Grain Boundary Chemistry and Morphology of Heavily Doped Cerium Dioxide

by

Douglas A. Blom

S.B., Materials Science and Engineering
Massachusetts Institute of Technology, 1993

Submitted to the Department of Materials Science and Engineering
in partial fulfillment of the requirements for the degree of

Doctor of Science in Ceramics

at the

MASSACHUSETTS INSTITUTE OF TECHNOLOGY

June 1998

© Massachusetts Institute of Technology 1998. All rights reserved.

Author ....
Department of Materials Science and Engineering
May 1, 1998

Certified by ....
Yet-Ming Chiang
Kyocera Professor of Ceramics
Thesis Supervisor

Accepted by ....
Linn W. Hobbs
John F. Elliot Professor of Materials
Chairman, Departmental Committee on Graduate Students

AUG 17 1998 ARCHIVES
LIBRARIES

Grain Boundary Chemistry and Morphology of Heavily Doped Cerium Dioxide

by

Douglas A. Blom

Submitted to the Department of Materials Science and Engineering
on May 1, 1998, in partial fulfillment of the
requirements for the degree of
Doctor of Science in Ceramics

Abstract

Ceria is a model system for oxygen ion conducting ceramics of the cubic fluorite structure, in which grain boundaries are known to limit the overall ionic conductivity of polycrystals. Measurements of grain boundary segregation of the aliovalent dopants Gd^{3+} and Ta^{5+} in heavily doped ceria have been made using a Vacuum Generators HB603 scanning transmission electron microscope (STEM). Space charge models both at the dilute limit, and with a limited site density at the interface, have been applied. In addition, a number of adsorption models have been considered.

The segregation isotherms of singly doped compositions allow one to determine the majority driving force for Gd^{3+} and Ta^{5+} ions in ceria. Gd^{3+} segregation is driven primarily by electrostatic interactions as described by a limited-site space charge model which explicitly considers the site density available at the interface. Ta^{5+} segregation in ceria is primarily associated with adsorption effects due to elastic strain relaxation.

From the singly doped compositions one cannot determine whether a space charge exists in Ta^{5+} doped ceria, nor the contribution of adsorption to Gd^{3+} segregation in ceria. In co-doped samples, it becomes possible to study co-segregation effects between Gd^{3+} and Ta^{5+}, as well as the minority segregation driving force(s). Specifically, by changing the lattice defect chemistry, the space charge potential ϕ_∞, changes, allowing for the separation of electrostatic and adsorption driving forces. Ta^{5+} segregation was significantly depressed in co-doped compositions, indicating a negative cosegregation effect of Gd^{3+} ions on Ta^{5+} ions in ceria. Gd^{3+} segregation was successfully modeled by a limited-site space charge model. Ta^{5+} additions did not affect the level of Gd^{3+} segregation in co-doped ceria.

Grain boundaries observed with HREM in Ta^{5+} containing ceria often contained an amorphous siliceous phase, while all boundaries observed in Gd^{3+} doped samples were free of secondary phase. The solubility of Si in ceria is strongly influenced by aliovalent dopants. Amorphous intergranular silicate films were observed in Ta^{5+} doped ceria with less Si impurity than Gd^{3+} doped samples which were film-free. The adsorption of Ta^{5+} to the grain boundary core promotes the formation of Si containing amorphous films. Gd^{3+} segregation in a space charge does not.

Confirmation of a space-charge in acceptor-doped ceria allows for the explanation of grain boundary blocking effects in materials without amorphous intergranular films. Acceptor-doped fluorite structure oxides will have grain boundaries with a net positive charge balanced by a negative space charge layer. Positively charged defects such as $V_O^{\cdot\cdot}$ will be depleted in the near grain boundary space charge and it is proposed that this depletion is responsible for the blocking nature of grain boundaries in fluorite structure oxides.

Thesis Supervisor: Yet-Ming Chiang
Title: Kyocera Professor of Ceramics

Contents

1 Introduction **13**

2 Theory **17**

2.1 Space Charge Models for Ceria 17

2.1.1 Dilute Model 20

2.1.2 Limited-Site Model 26

2.2 Defect Chemistry for Gd^{3+} and Ta^{5+} Doped Ceria 29

2.3 Solid State Adsorption 35

2.3.1 Langmuir Adsorption 35

2.3.2 Guttmann and McLean Model for Ternary Adsorption 37

3 Experimental Procedure **41**

3.1 Powder Preparation 43

3.2 Sample Fabrication 44

3.3 STEM Characterization 45

4 Results **51**

4.1 Gd^{3+} Segregation in Singly Doped Ceria 51

4.2 Ta^{5+} Segregation in Singly Doped Ceria 62

4.3 Grain Boundary Segregation in co-doped Ceria 68

4.3.1 Gd^{3+} Segregation in co-doped Ceria 68

4.3.2 Ta^{5+} Segregation in co-doped Ceria 76

4.4 Grain Boundary Morphology in Doped Ceria 79

4.4.1 Gd^{3+} Doped Ceria 83

4.4.2 Ta^{5+} Doped Ceria 89

4.4.3 co-doped Ceria 90

4.5 Implications for Transport Properties 108

5 Conclusions **113**

A Coverage Histograms **119**

Bibliography **135**

List of Figures

2-1 Schematic defect formation process in ionic solids. 19

2-2 Defect mole fractions in Gd^{3+}-doped ceria versus mole% Gd at 1500°C in air. 32

2-3 Defect mole fractions in Ta^{5+}-doped ceria as a function of mole% Ta at 1500°C in air. 33

2-4 Defect mole fractions vs. net % Gd in ceria co-doped with Gd^{3+} and Ta^{5+}. 34

3-1 Schematic of the STEM microanalysis technique 46

4-1 X-ray line-scan across a grain boundary in sample Gd7. Gd^{3+} segregation exists within ±5 nm of the boundary. 52

4-2 Grain boundary segregation at 16 different boundaries in Gd2. Error bars are derived from counting statistics error. 53

4-3 Grain boundary segregation at 23 different boundaries in Gd7. Error bars are derived from counting statistics error. 54

4-4 Gd^{3+} segregation isotherm at 1500°C in air 56

4-5 Additional fits of the limited-site space charge with varying assumptions of the number of interfacial sites (N_s). 58

4-6 Comparison of the limited-site space charge model and the Langmuir adsorption isotherms to the experimental data. 61

4-7 X-ray linescan across a grain boundary in sample Ta3. Ta^{5+} segregation exists within ±5 nm of the boundary. 64

4-8 Grain boundary segregation at 10 different boundaries in Ta1. Error bars are derived from counting statistics error. 65

4-9 Measured Ta^{5+} segregation isotherm and Langmuir adsorption fit. 66

4-10 X-ray linescan across a grain boundary in sample CGT4. Gd^{3+} and Ta^{5+} segregation exists within ±5 nm of the boundary. 69

4-11 Gd^{3+} and Ta^{5+} coverage in co-doped ceria. 70

4-12 Gd^{3+} coverage in co-doped ceria. Comparison between space charge models and experiment. 71

4-13 Gd^{3+} coverage in co-doped ceria. Comparison between Langmuir adsorption model originally fit to segregation data in Gd^{3+} doped ceria and experimental observations of Gd^{3+} segregation in co-doped ceria. 73

4-14 Gd^{3+} coverage in co-doped ceria. Comparison between Guttmann/McLean model and experiment. 75

4-15 Ta^{5+} coverage in co-doped ceria. Comparison between two parameter Langmuir model and experiment. 77

4-16 Ta^{5+} coverage in co-doped ceria. Comparison of experimental observations with the Guttmann/McLean model discussed in Section 2.3 and the best-fit Langmuir isotherm. 78

4-17 High resolution electron micrograph of a grain boundary in Gd7 illustrating the absence of an amorphous film. 81

4-18 High resolution electron micrograph of a grain boundary in Ta1 at which an amorphous film exists 85

4-19 High resolution electron micrograph of a grain boundary in Ta3 at which an amorphous film exists 87

4-20 X-ray linescan across the boundary seen in Figure 4-21. 91

4-21 High resolution electron micrograph of a grain boundary in CGT4 at which a 7.8 nm wide amorphous film exists 93

4-22 X-ray linescan across the boundary seen in Figure 4-25. 96

4-23 X-ray linescan across the boundary seen in Figure 4-26. 97

4-24 Ta^{5+} coverage versus grain boundary film thickness in CGT4 and Ta3. . . 98

4-25 High resolution electron micrograph of a grain boundary in CGT4 at which a 5.4 nm wide amorphous film exists 99

4-26 High resolution electron micrograph of a grain boundary in CGT4 at which a 2.2 nm wide amorphous film exists 101

4-27 Proposed low energy defect complex for Si in ceria suggested to increase the solubility of Si. 105

4-28 The Ta_2O_5-SiO_2 binary phase diagram 106

4-29 The Gd_2O_3-SiO_2 binary phase diagram 107

4-30 Defect profiles in 20 mole % Gd^{3+} doped ceria at 1773K and air atmosphere with a positive charge on the grain boundary and a negative space charge region. 112

5-1 Schematic diagram of Gd^{3+} in the space charge layer of ceria, Ta^{5+} adsorption at the glass/crystal interface and dissolution into the amorphous siliceous film. 117

List of Tables

2.1 Defect chemical reactions in ceria 30

2.2 Ionic radii and estimated enthalpy of segregation for various elastic constants of ceria 36

3.1 Predicted segregation of Gd^{3+} and Ta^{5+} in co-doped ceria 42

3.2 Compositions 44

4.1 Model input parameters 72

5.1 Projected segregation driving forces for aliovalent dopants in ceria 116

Acknowledgments

Many people have helped me throughout my graduate career at MIT. I would first like to thank my advisor, Yet-Ming Chiang for all his helpful insights, patience and support. I am not the easiest graduate student to advise, but you pulled it off. Dr. Tony Garratt-Reed was invaluable for his assistance in learning to operate the STEM and understand the subtleties of X-ray microanalysis. Dr. Haifeng Wang spent many hours with me on the 002B in order to produce the HREM images contained herein. Fred Wilson, John DiFrancesco, and Toni Centorino provided a stable support for me as I dealt with experimental difficulties and MIT bureaucracy.

I also had a large number of friends and co-slackers which helped me maintain a grip on my sanity throughout graduate school. The entire Coffee Crew (aka Slack Train) provided many fun hours of chemical stimulation and distracting conversation. Members included Hal, Arun, Eric, Erika, Tracey, Erin, Shih-tung, and Srikar. Dr. David C. Bell has contributed greatly to my caffeine addiction, because after all "It's always coffeetime in America." The contributions of Khaldi the goat boy were instrumental to the completion of this thesis. Thanks to Matz, Arun, and Eric for introducing me to the strange cast of characters who inhabit the MIT weight room. Erika, Nat & Tracey are some of my closest friends who have shared their lives with me. Dinners and outings with you will always be a treasured memory of my time at MIT.

My family has always been so supportive of me. Whatever I have done, you have always been there for me. Thank you. Tammy has been with me as I traveled the hard road to graduation. She always believed in me, even when I didn't believe in myself. Her love and support are irreplaceable.

Chapter 1

Introduction

Cubic fluorite structure oxides are prototypical oxygen ion conductors with applications as oxygen sensors, oxygen separation membranes and as the solid electrolyte in solid oxide fuel cells (SOFC's) [1–3]. The most widely used and studied fluorite structure oxide is cubic stabilized zirconia (CSZ). 8–15 mole percent of lower valence cations such as Ca^{2+} or Y^{3+} added to pure ZrO_2 stabilizes the cubic phase to room temperature and leads to high oxygen ion conductivity due to oxygen vacancy compensation of the dopant.

Grain boundary segregation of dopants influences a number of the structural and functional properties of fluorite structure oxides. Grain growth studies in ceria have shown that segregation of aliovalent dopants leads to a reduced grain boundary mobility [4–6]. Impedance measurements have identified a high resistivity layer existing at the grain boundaries in CSZ [7–9]. This "grain boundary effect" is a limiting factor in the practical application of CSZ as an oxygen conductor and may be related to the spatial distribution of defects near the grain boundary as well as the existence of thin glassy films surrounding the grains. As in zirconia, the grain boundaries in ceria-based electrolytes are known to be electrically blocking [10–18]. It has been suggested that the blocking behavior is due to impurity segregation [9, 11–13, 15].

A number of semiquantitative studies of both surface and grain boundary segregation of dopants in cubic fluorite oxides have been conducted using a variety of techniques [5, 19–26]. The majority of the data so far reported have been obtained using surface science techniques applied to polycrystalline fracture surfaces. The observed segregation of aliovalent solutes such as Y^{3+}, Ce^{3+}, Mg^{2+}, Sc^{3+}, Sb^{3+}, and In^{3+} has been attributed to space charge effects [5, 21, 23], adsorption [22, 26] and cosegregation with a Si-rich impurity phase [24–26]. Segregation to surfaces and grain boundaries in polycrystalline samples [5, 19–22] as well as at single crystal surfaces [23] has been observed. Recent low energy ion scattering (LEIS) results on Gd^{3+} doped ceria have established that Gd^{3+} segregation in heavily doped ceria occurs in approximately the first 5 monolayers [19]. Hwang and Chen observed that grain boundary segregation in Ce-stabilized tetragonal zirconia differed depending on the relative charge of the dopants, providing evidence of segregation driven by electrostatics [5].

The most quantitative study to date of grain boundary segregation in fluorite structure oxides is the work of Aoki *et al.* [9]. They correlated Ca and Si grain boundary segregation with grain boundary impedance in high purity Ca-stabilized zirconia. Measurements of Ca and Si grain boundary coverage were made using scanning transmission electron microscopy (STEM). It was found that the boundary impedance varied with the combined coverage of Ca and Si at the boundaries. No amorphous silicate films were formed due to the extremely low level of silicon impurities in the bulk ($\leq$ 80 ppm). Decreasing the grain size lowered the total grain boundary coverage of Ca and Si and led to lower grain boundary impedance. Cosegregation of Ca and Si was observed. Ca segregation scaled with Si segregation so that the composition of the grain boundary was $\approx Si_2Ca_3O_7$.

Zirconia is a difficult material in which to study equilibrium segregation over a wide dopant concentration range, due to the existence of multiple phases, especially at low doping levels. In multi-phase materials the excess segregating to an interface will in principal be different for each phase. Ceria, on the other hand, maintains the cubic fluorite phase over a wide range of doping. A number of solutes such as the rare earths and yttrium [27–29] are highly soluble. Cation diffusion is very slow below 1000°C [28], allowing the high temperature cation distribution to be observed in quenched samples. The defect chemical model of ceria has been well established in the literature [10,30–34]. Furthermore, results obtained in ceria can have impact on its technological uses as a low temperature solid oxide fuel cell electrolyte and as a redox catalyst [3,35–37].

In this work, I examined the segregation behavior of the aliovalent solutes Gd^{3+} and Ta^{5+} in ceria, as a model for heavily doped fluorite structure oxides. Gd^{3+} doped ceria has been extensively studied as an electrolyte in low temperature SOFC's [2,38–41], and the bulk defect chemistry is particularly well understood [10,30–34,42–45]. Because Gd^{3+} is highly soluble in ceria and the size misfit of Gd'_{Ce} is small, non-electrostatic contributions to segregation are minimized. Ta^{5+} was chosen as a representative donor due to the availability of literature data on the defect chemistry [46,47].

The samples fabricated for this study represent a wide lattice defect chemistry regime. Using STEM, the excess of aliovalent solute at grain boundaries was quantified. Previous work in TiO_2 developed the experimental technique and the analysis used to correlate lattice defect chemistry and grain boundary segregation [48–50]. HREM was used to study the grain boundary morphology and its interaction with the grain boundary chemistry as determined by STEM. We seek to understand the driving forces that cause segregation in highly concentrated ionic solutions, with the ultimate goal of controlling the transport properties of the grain boundaries.

The segregation isotherms in singly doped ceria allow one to determine the majority driving force for grain boundary segregation. However, minority segregation forces and co-segregation effects cannot be studied with singly doped compositions. Co-doping allows the study of co-segregation effects between Gd^{3+} and Ta^{5+}, as well as the minority segregation driving force(s). Specifically, by changing the lattice defect chemistry, the space charge potential ϕ_{∞}, changes, allowing for the separation of electrostatic and adsorption driving forces.

Chapter 2

Theory

2.1 Space Charge Models for Ceria

Frenkel [51] first formulated the idea of a near-interface space charge region for ionic solids, in which point defects are generally charged. In the bulk, electroneutrality holds and limits the formation of intrinsic point defects to neutral combinations, *eg.* $V_O^{\cdot\cdot}$ and O_i'' . (Kröger-Vink notation is used throughout [52].) Since lattice discontinuities act as sinks for point defects, the equilibration of point defects of different formation energies with a lattice discontinuity creates a charge imbalance. Kliewer and Kohler showed that this surface charge is a feature of thermodynamic equilibrium for ionic solids [53]. The free energy of formation of a point defect is here defined as the energy required to take an ion from a lattice site and place it at the interface. Figure 2-1 is a schematic diagram of the defect formation process and the formation energy definition. $g_{V_O^{\cdot\cdot}}$ is the energy necessary to transport an O^{2-} ion from the bulk to an interface, leaving behind an $V_O^{\cdot\cdot}$. $g_{O_i''}$ is the free energy of formation of an O_i'', which is equal to the energy necessary to transfer an O^{2-} ion from the interface to a bulk interstitial site. These energies are unique to each interface site.

The surface charge creates an electrostatic potential difference between the interface and the bulk of the crystal. Charged aliovalent solutes will respond to the electric field and segregate or deplete in the near-interface region in order to shield the interfacial charge. The sign and magnitude of the interfacial charge is therefore a function of the lattice defect chemistry, and the formation energies of the individual intrinsic ionic and electronic defects. Manipulating the lattice defect chemistry allows for the possibility of controlling the spatial distribution at interfaces of *all* charged defects, which in turn may allow one to engineer the defect-dependent interfacial properties. Specifically, there exists for a particular defect chemistry a state known as the isoelectric point. At the isoelectric point, the interfaces are not charged and therefore the defects exhibit no spatial variation across a grain boundary. In TiO_2, the existence of regimes of positive and negative space charge potential, and of an isoelectric point, have been experimentally demonstrated as a function of doping, temperature and oxygen activity [48–50].

Interfaces in ceria are believed to be more oxygen deficient than the bulk of the material. Experimental evidence of this has been seen in nanocrystalline ceria [54] and at surfaces in ceria [55]. The enhanced nonstoichiometry of nanocrystalline material suggests that the grain boundaries are more easily reduced than the bulk. Calculations on surface oxygen vacancy formation have shown that the (111), (110) and (310) surfaces are also more oxygen deficient than the bulk [56, 57]. Since oxygen vacancies in ceria are charged, the interfaces in undoped ceria can then be expected to be net positively charged with an accompanying negative space charge layer. Acceptor doping is expected to further increase the magnitude of this interface charge. For the experimental conditions investigated in this work, negatively charged dopants are expected to segregate to the interfaces and positively charged dopants are expected to be depleted.

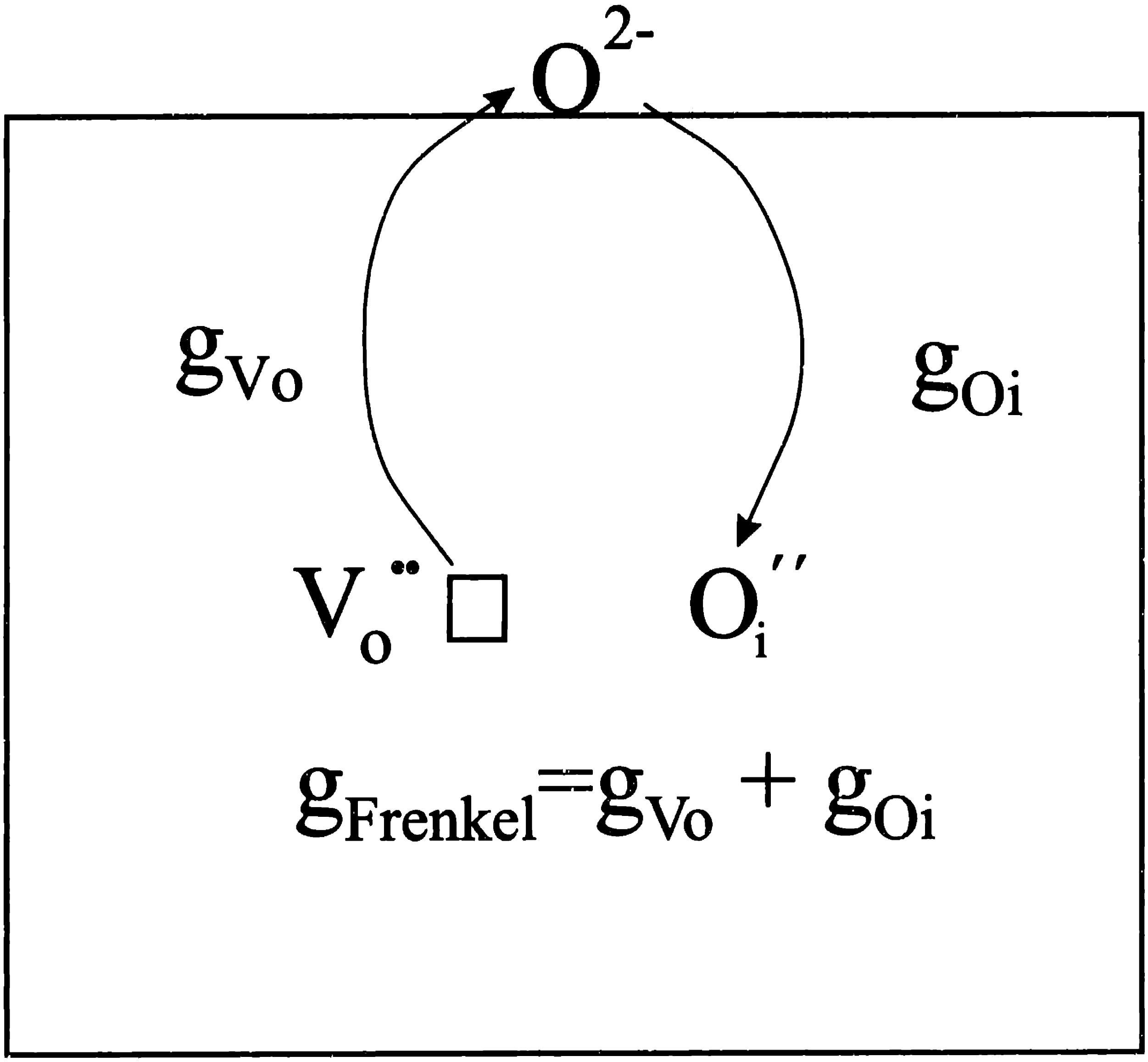
O^{2-}
g_{Vo}
g_{Oi}
$V_o^{\bullet\bullet}$
O_i''
$g_{Frenkel}=g_{Vo}+g_{Oi}$

Figure 2-1: Schematic defect formation process in ionic solids.

Because the majority ionic defects in undoped as well as doped ceria are $V_O^{\cdot\cdot}$, the free energy of formation of an oxygen vacancy, $g_{V_O^{\cdot\cdot}}$, is a key thermodynamic quantity when discussing the defect chemistry and space charge of ceria. Space charge models solve Poisson's equation for the distribution of defects throughout the crystal given the assumption of electroneutrality in the bulk. The formation energy of the dominant ionic defect is the vital link between the defect chemistry of the bulk material and the space charge [49]. Although $g_{V_O^{\cdot\cdot}}$ is not known *a priori*, a bulk defect chemical model of ceria is well established, and therefore measurements of grain boundary segregation can be used to obtain the value of $g_{V_O^{\cdot\cdot}}$.

2.1.1 Dilute Model

Kliewer and Koehler [53, 58–60] derived a framework for discussing space charge segregation for *dilute* doped systems. The free energy per unit area of a crystal is given by:

$$F = \int_0^\infty \Big[\sum_i n_i g_i + \frac{1}{2}\rho(x)\phi(x)\Big] dx - TS_c \tag{2.1}$$

where n_i is the number density of defect i, g_i is the free energy of formation of defect i, $\rho(x)$ is the local charge density, $\phi(x)$ is the local electrostatic potential, T is the absolute temperature, and S_c is the configurational entropy of the defects. Poisson's equation links the charge distribution in the solid, $\rho(x)$ to the electrostatic field, $\phi(x)$:

$$\nabla^2\phi(x) = \frac{-4\pi}{\epsilon}\rho(x) \tag{2.2}$$

where ϵ is the static dielectric constant of the material. Thermodynamic equilibrium is achieved when the free energy is minimized. The relevant constraints are:

$$\phi = \begin{cases} 0 & \text{at} \quad x = 0 \\ \phi_\infty & \text{at} \quad x = \infty \end{cases} \tag{2.3a}$$

$$\frac{d\phi}{dx} = 0 \quad \text{at} \quad x = \infty \tag{2.3b}$$

$$\int_0^\infty (n_{solute} + n_{SV})dx = C_{solute}V \tag{2.3c}$$

C_{solute} is the bulk solute concentration and V is the total crystal volume. Using the calculus of variations, it is possible to show that the minimization condition is [53, 58]:

$$\begin{aligned} 0 = \delta F = \int_0^\infty \Bigg\{ & \delta n_{V_o}\left[g_{V_o} + z_{V_o}e\phi(x) + kT\ln\left(\frac{n_{V_o}}{2N}\right)\right] + \\ & \delta n_{O_i}\left[g_{O_i} + z_{O_i}e\phi(x) + kT\ln\left(\frac{n_{O_i}}{2N}\right)\right] + \\ & \delta n_{SV}\left[g_{V_o} + B_{SV} + z_{SV}e\phi(x) + kT\ln\left(\frac{n_{SV}}{8N}\right)\right] + \\ & \delta n_{solute_i}\left[z_{solute_i}e\phi(x) - \alpha_L + kT\ln\left(\frac{n_{solute_i}}{N}\right)\right]\Bigg\}dx \end{aligned} \tag{2.4}$$

where z_i is the effective charge on defect i, N is the number density of sites per molecule, B_{SV} is the binding energy of the solute-vacancy defect associate, and α_L is a Lagrangian multiplier necessary to maintain solute conservation. For F to be at a minimum, the coefficients of every δn_i term must be 0. For doped ceria, the equations become:

$$[V_O^{\cdot\cdot}] = \frac{n_{V_O^{\cdot\cdot}}}{2N} = \exp\left(\frac{-\left(g_{V_O^{\cdot\cdot}} + 2e\phi(x)\right)}{kT}\right) \tag{2.5a}$$

$$[O_i''] = \frac{n_{O_i''}}{2N} = \exp\left(\frac{-\left(g_{O_i''} - 2e\phi(x)\right)}{kT}\right) \tag{2.5b}$$

$$n = [e'] = \frac{n_{e'}}{N} = \exp\left(\frac{-\left(g_{e'} - e\phi(x)\right)}{kT}\right) \tag{2.5c}$$

$$p = [h^\cdot] = \frac{n_{h^\cdot}}{N} = \exp\left(\frac{-\left(g_{h^\cdot} + e\phi(x)\right)}{kT}\right) \tag{2.5d}$$

$$[A'_{Ce}] = \frac{n_A}{N} = C_{solute}(1 - p_{SV})\exp\left(\frac{z_A e\left(\phi(x) - \phi_\infty\right)}{kT}\right) \tag{2.5e}$$

$$[D_{Ce}^\cdot] = \frac{n_D}{N} = C_{solute}\exp\left(\frac{z_D e\left(\phi(x) - \phi_\infty\right)}{kT}\right) \tag{2.5f}$$

$$[(A'_{Ce}V_O^{\cdot\cdot})^\cdot] = \frac{n_{SV}}{N} = 8C_{solute}p_{SV}\exp\left(\frac{z_{SV} e\left(\phi(x) - \phi_\infty\right)}{kT}\right) \tag{2.5g}$$

where p_{SV} is the probability of the formation of a solute-vacancy defect associate.

An implicit assumption in Equation 2.5 is that the amount of segregant is much smaller than the available solute. This assumption holds for sub-monolayer segregation in doped samples with micron size grains. Kliewer and Koehler [53] showed that the spatial distribution of defects in the space charge region follows an inverse hyperbolic tangent function, which for $e\phi_\infty \ll kT$ is essentially an exponential.

If a defect chemical model is available, so that the bulk concentrations are known, aliovalent solute accumulation can be used to determine the space charge potential. The results can give information on the individual defect formation energies. Equations 2.5

give the spatial variation of both intrinsic and extrinsic defects in doped ceria. Given the boundary conditions from Equation 2.3, the defect concentrations (in number/m^3) at $x = 0$ and $x = \infty$ can be written as:

$$\begin{aligned}
n_{V_O^{\cdot\cdot},0} &= 2N \exp \frac{-g_{V_O^{\cdot\cdot}}}{kT} & n_{V_O^{\cdot\cdot},\infty} &= 2N \exp \frac{-\left(g_{V_O^{\cdot\cdot}} + 2e\phi_\infty\right)}{kT} && \text{(2.6a)}\\
n_{O_i'',0} &= 2N \exp \frac{-g_{O_i''}}{kT} & n_{O_i'',\infty} &= 2N \exp \frac{-\left(g_{O_i''} - 2e\phi_\infty\right)}{kT} && \text{(2.6b)}\\
n_{e',0} &= N \exp \frac{-g_{e'}}{kT} & n_{e',\infty} &= N \exp \frac{-\left(g_{e'} - e\phi_\infty\right)}{kT} && \text{(2.6c)}\\
n_{h^\cdot,0} &= N \exp \frac{-g_{h^\cdot}}{kT} & n_{h^\cdot,\infty} &= N \exp \frac{-\left(g_{h^\cdot} + e\phi_\infty\right)}{kT} && \text{(2.6d)}\\
n_{A,0} &= NC_{solute}(1 - p_{SV}) \exp \frac{-e\phi_\infty}{kT} & n_{A,\infty} &= NC_{solute}(1 - p_{SV'}) && \text{(2.6e)}\\
n_{D,0} &= NC_{solute} \exp \frac{e\phi_\infty}{kT} & n_{D,\infty} &= NC_{solute} && \text{(2.6f)}\\
n_{SV,0} &= NC_{solute} p_{SV} \exp \frac{z_{SV} e\phi_\infty}{kT} & n_{SV,\infty} &= NC_{solute} p_{SV} && \text{(2.6g)}
\end{aligned}$$

The defect equations can therefore be written as:

$$n_i(x) = n_{i,\infty} \exp \left[\frac{-z_i e[\phi(x) - \phi_\infty]}{kT} \right] \tag{2.7}$$

The space charge density is thus:

$$\rho(x) = \sum_i z_i e n_i(x) = \sum_i z_i e n_{i,\infty} \exp \left(\frac{-z_i e\left(\phi(x) - \phi_\infty\right)}{kT} \right) \tag{2.8}$$

Substituting Equation 2.8 into Poisson's equation (Equation 2.2) yields:

$$\frac{\partial^2 \phi}{\partial x^2} = -\frac{4\pi}{\epsilon} \sum_i z_i e n_{i,\infty} \exp \left[\frac{-z_i e[\phi(x) - \phi_\infty]}{kT} \right] \tag{2.9}$$

Integrating Equation 2.9 by multiplying both sides by $2\frac{d\phi}{dx}$ and using the chain rule in the following manner

$$\frac{d}{dx}\left(\frac{d\phi}{dx}\right)^2 = 2\left(\frac{d\phi}{dx}\right)\frac{d^2\phi}{dx^2} \tag{2.10}$$

yields upon evaluation of the constant of integration at $x = \infty$:

$$\frac{d\phi}{dx} = \left\{\frac{8\pi kT}{\epsilon}\sum_i n_{i,\infty}\left[\exp\left(\frac{-z_i e[\phi - \phi_\infty]}{kT}\right) - 1\right]\right\}^{1/2} \tag{2.11}$$

From Gauss's law

$$\sigma = -\int_0^\infty \rho(x)dx = -\frac{\epsilon}{4\pi}\left(\frac{d\phi}{dx}\right)_{x=0} \tag{2.12}$$

the equation linking the surface charge density to the space charge potential is [48,49,61]:

$$\sigma = -\left\{\frac{\epsilon kT}{2\pi}\sum_i n_{i,\infty}\left[\exp\left(\frac{z_i e\phi_\infty}{kT}\right) - 1\right]\right\}^{1/2} \tag{2.13}$$

For the current sign convention, in which $\phi(x = 0) = 0$, the sign of the defects which are enriched in the space charge region is the same as that of the space charge potential. Therefore, for a particular sign of the potential, either positive or negative defects, but not both, will contribute significantly to the space charge density. For instance, if Gd'_{Ce} segregates in a space charge layer in ceria, then $\phi_\infty < 0$, and the following relation exists between the measured Gd excess, Γ_{Gd}, and the interfacial charge density, σ:

$$\sigma = \frac{e\Gamma_{Gd}}{\left(1 + \frac{n_{e',\infty}}{n_{Gd'_{Ce},\infty}}\right)^{1/2}} \tag{2.14}$$

For Gd doping levels >1%, $n_{e',\infty} \ll n_{Gd'_{Ce}}$, and the measured solute coverage, Γ_{Gd}, is equal to σ/e. Substituting the charge of the measured excess, $e\Gamma_{Gd}$, into Equation 2.13 gives the space charge potential, ϕ_∞, with no adjustable parameters except the bulk defect concentrations. As discussed later, the bulk defect concentrations can be determined from a defect chemical model. Once ϕ_∞ has been calculated, it is a simple matter to numerically integrate the defect concentration expressions (Equation 2.7) to get the integrated excess of each defect in the space charge region. The integration can be carried out from the interface to 2 Debye lengths into the bulk, where the Debye length, κ^{-1}, is defined as:

$$\kappa^{-1} = \sqrt{\frac{\epsilon kT}{8\pi e^2 N}} \tag{2.15}$$

where ϵ is the static dielectric constant and N is the concentration per cubic meter of the most prevalent mobile defect.

The value of $g_{V_O^{\cdot\cdot}}$ may be obtained from the condition of electroneutrality in the bulk:

$$[Gd'_{Ce}] + n + 2[O_i''] = 2[V_O^{\cdot\cdot}] + [(Gd'_{Ce} - V_O^{\cdot\cdot})^{\cdot}] + [Ta_{Ce}^{\cdot}] \tag{2.16a}$$

$$\begin{aligned} [Gd'_{Ce}] + \left(\frac{K_{redox}}{2}\right)^{1/2} P_{O_2}^{-1/4} \exp\left(\frac{g_{V_O^{\cdot\cdot}} + 2e\phi_\infty}{2kT}\right) + 4K_{Frenkel}\exp\left(\frac{g_{V_O^{\cdot\cdot}} + 2e\phi_\infty}{kT}\right) \\ = 4\exp\left(\frac{-\left(g_{V_O^{\cdot\cdot}} + 2e\phi_\infty\right)}{kT}\right) + [(Gd'_{Ce} - V_O^{\cdot\cdot})^{\cdot}] + [Ta_{Ce}^{\cdot}] \end{aligned} \tag{2.16b}$$

It is now possible to numerically solve for $g_{V_O^{\cdot\cdot}}$, the free energy of formation of an oxygen vacancy. Implicit in using the values of Gd'_{Ce} and $(Gd'_{Ce} - V_O^{\cdot\cdot})^{\cdot}$ from the bulk in the electroneutrality equation is the assumption that the association reaction remains constant throughout the space charge region.

2.1.2 Limited-Site Model

Blakely and coworkers [62–64] extended Kliewer and Koehler's model to account for a limited number of sites at the lattice discontinuity. We will refer to this model as the limited-site model. By explicitly including a term to account for the configurational entropy at the interfacial layer, the assumption of a dilute solution of defects throughout the crystal was relaxed. They still assume a dilute solution in the bulk. The free energy equation that results is:

$$F = \int_0^\infty \left[\sum_i n_i g_i + \frac{1}{2}\rho(x)\phi(x) \right] dx - TS_c - TS_{c_{surface}} \tag{2.17}$$

The surface configurational entropy can be written as [62]:

$$S_{c_{surface}} = -k \ln \left[\frac{N_s!}{(N_s - n_s)!n_s!} \right] \tag{2.18}$$

where N_s is the number of surface sites available, n_s is the number of occupied surface sites. When $n_s \ll N_s$, the surface entropy is negligible and the equation reduces to Equation 2.1 derived by Kliewer and Koehler [53]. Because n_s is limited to be $\leq N_s$, the interfacial charge density, σ, is now limited to be $\leq z_{n_s} e N_s$. Using Sterling's approximation, and varying the surface entropy with respect to the number of occupied surface sites yields:

$$\delta S_{c_{surface}} = \delta n_s k \ln \left(\frac{N_s - n_s}{n_s} \right) \tag{2.19}$$

The interfacial charge density, σ, the number density of occupied interfacial sites, n_s, and the integrated space charge density, ρ, are related via overall electrical neutrality of the crystal:

$$\sigma = z_{n_s} e n_s = -\int_0^\infty \rho(x) dx \tag{2.20}$$

Varying Equation 2.20 and substituting for δn_s in Equation 2.19 yields:

$$\delta S_{c_{surface}} = -\frac{1}{e z_{n_s}} \int_0^\infty \delta\rho(x) k \ln\left(\frac{N_s - n_s}{n_s}\right) dx \tag{2.21}$$

The overall minimization condition is then:

$$\begin{aligned} 0 = \delta F = \int_0^\infty \Bigg\{ & \delta n_{V_O}\left(g_{V_O} + z_{V_O} e\phi(x) + kT \ln\left[\frac{n_{V_O}}{2N}\left(\frac{N_s - n_s}{n_s}\right)^{\frac{z_{V_O}}{z_{n_s}}}\right]\right) + \\ & \delta n_{O_i}\left(g_{O_i} + z_{O_i} e\phi(x) + kT \ln\left[\frac{n_{O_i}}{2N}\left(\frac{N_s - n_s}{n_s}\right)^{\frac{z_{O_i}}{z_{n_s}}}\right]\right) + \\ & \delta n_{SV}\left(g_{SV} + z_{SV} e\phi(x) + kT \ln\left[\frac{n_{SV}}{8N}\left(\frac{N_s - n_s}{n_s}\right)^{\frac{z_{SV}}{z_{n_s}}}\right]\right) + \\ & \delta n_{sol}\left(z_{sol} e\phi(x) - \alpha_L + kT \ln\left[\frac{n_{sol}}{N}\left(\frac{N_s - n_s}{n_s}\right)^{\frac{z_{SV}}{z_{n_s}}}\right]\right) \Bigg\} dx \end{aligned} \tag{2.22}$$

The equations for the spatial distribution of defects for aliovalent doped ceria are:

$$[V_O^{\bullet\bullet}] = \frac{n_{V_O^{\bullet\bullet}}}{2N} = \left(\frac{n_s}{N_s - n_s}\right) \exp\left(\frac{-\left(g_{V_O^{\bullet\bullet}} + 2e\phi(x)\right)}{kT}\right) \tag{2.23a}$$

$$[O_i''] = \frac{n_{O_i''}}{2N} = \left(\frac{N_s - n_s}{n_s}\right) \exp\left(\frac{-\left(g_{O_i''} - 2e\phi(x)\right)}{kT}\right) \tag{2.23b}$$

$$n = [e'] = \frac{n_{e'}}{N} = \left(\frac{n_s}{N_s - n_s}\right)^{1/2} \exp\left(\frac{-\left(g_{e'} - e\phi(x)\right)}{kT}\right) \tag{2.23c}$$

$$p = [h^\bullet] = \frac{n_{h^\bullet}}{N} = \left(\frac{N_s - n_s}{n_s}\right)^{1/2} \exp\left(\frac{-\left(g_{h^\bullet} + e\phi(x)\right)}{kT}\right) \tag{2.23d}$$

$$[A'_{Ce}] = \frac{n_A}{N} = C_{solute}(1 - p_{SV}) \exp\left(\frac{e\left(\phi(x) - \phi_\infty\right)}{kT}\right) \tag{2.23e}$$

$$[D^\bullet_{Ce}] = \frac{n_D}{N} = C_{solute} \exp\left(\frac{-z_D e\left(\phi(x) - \phi_\infty\right)}{kT}\right) \tag{2.23f}$$

$$[Assoc] = \frac{n_{SV}}{N} = 8C_{solute}p_{SV} \exp\left(\frac{-z_{SV} e\left(\phi(x) - \phi_\infty\right)}{kT}\right) \tag{2.23g}$$

The interfacial site density is related to the charge density, σ, by Equation 2.20. A charge of +2 is assumed per defect in the surface charge. This corresponds to $V_O^{\bullet\bullet}$, which are known to be doubly ionized in ceria at these temperatures. Substituting the new defect concentration terms into the bulk electroneutrality condition, Equation 2.16a yields:

$$\begin{aligned}
[Gd'_{Ce}] &+ \left(\frac{K_{redox}}{2}\right)^{1/2} P_{O_2}^{-1/4} \left(\frac{2eN_s - \sigma}{\sigma}\right)^{1/2} \exp\left(\frac{g_{V_O^{\cdot\cdot}} + 2e\phi_\infty}{2kT}\right) \\
&+ 4K_{Frenkel} \left(\frac{2eN_s - \sigma}{\sigma}\right) \exp\left(\frac{g_{V_O^{\cdot\cdot}} + 2e\phi_\infty}{kT}\right) \\
&= 4\left(\frac{\sigma}{2eN_s - \sigma}\right) \exp\left(\frac{-\left(g_{V_O^{\cdot\cdot}} + 2e\phi_\infty\right)}{kT}\right) + [(Gd'_{Ce} - V_O^{\cdot\cdot})] + [Ta_{Ce}^{\cdot}]
\end{aligned} \tag{2.24}$$

The free energy of formation of an oxygen vacancy can be calculated from experimentally observed segregation in the following manner. The space charge potential, ϕ_∞, is solved by substituting the experimentally measured $e\Gamma_{Gd}$ for σ in Equation 2.13. Equations 2.13 and 2.24 can then be simultaneously solved for the single unknown, $g_{V_O^{\cdot\cdot}}$. Note, however, that this value depends explicitly on the interfacial charge density, σ, and the number of interfacial sites, N_s. Numerical integration from the grain boundary to 2 Debye lengths into the bulk can be carried out to model the integrated excess of any particular defect.

2.2 Defect Chemistry for Gd^{3+} and Ta^{5+} Doped Ceria

Solving the defect chemistry is a necessary first step to obtain a quantitative space charge segregation model for ceria. The defect chemistry of both nonstoichiometric intrinsic ceria and acceptor doped ceria has been well established [10,30–34,44,45,65–67]. Acceptor dopant compensation is known to be ionic in nature. For Ta^{5+} doping, electronic compensation has been observed [46,47]. The consensus of the literature is that the dominant intrinsic defect reaction is the fully ionized anion Frenkel reaction:

$$O_O^x + V_i^x \longleftrightarrow V_O^{\cdot\cdot} + O_i'' \tag{2.25}$$

Table 2.1: Defect chemical reactions in ceria

Reaction	Mass Action Law	Experimental Value
$O_O^x + V_i^x \longleftrightarrow V_O^{\bullet\bullet} + O_i''$	$K_{Frenkel} = \frac{[V_O^{\bullet\bullet}][O_i'']}{[O_C^x][V_i^x]}$	$K_{Frenkel} = 4.88 \times 10^4 \exp\left[\frac{-4.45e}{kT}\right]$
$nil \longleftrightarrow e' + h^{\bullet}$	$K_e = [e'][h^{\bullet}]$	$K_e = \exp\left[\frac{-2.5e}{kT}\right]$
$O_O^x \longleftrightarrow V_O^{\bullet\bullet} + 2e' + \frac{1}{2}O_2$	$K_{redox} = \frac{[V_O^{\bullet\bullet}][e']^2 P_{O_2}^{\frac{1}{2}}}{[O_O^x]}$	$K_{redox} = 3.84 \times 10^6 \exp\left[\frac{-4.67e}{kT}\right]$
$Gd'_{Ce} + V_O^{\bullet\bullet} \longleftrightarrow (Gd'_{Ce} - V_O^{\bullet\bullet})^{\bullet}$	$K_{assoc} = \frac{[(Gd'_{Ce} - V_O^{\bullet\bullet})^{\bullet}]}{[V_O^{\bullet\bullet}][Gd'_{Ce}]}$	$K_{assoc} = 8 \exp\left[\frac{0.12e}{kT}\right]$

Thermogravimetric [34], coulometric titration [10, 32, 65], oxygen diffusion [66], and conductivity studies [10, 30, 31, 67] all provide support for this interpretation. In addition, it has been shown that electron migration occurs by a small polaron process in ceria [44, 45]. Equilibrium constants for the anion Frenkel [31], redox [30], Gd'_{Ce}— $V_O^{\bullet\bullet}$ association [42, 43], and e'— $h^{\bullet}$ pair production [68] defect reactions have been calculated from experimental results. Table 2.1 lists the reactions, the mass action laws and the experimentally observed values when the defect concentrations are in units of mole fraction. The implicit assumption in writing the mass action laws is that the defects are dilute enough that the concentrations may be substituted for the activities. Recent work in developing a non-dilute defect chemistry formalism has shown the importance of two effects at high defect concentrations: coulombic defect-defect energy interactions and site exclusion effects [69, 70]. Both effects serve to make the formation of additional defects more difficult at high concentrations. The details of how to correctly account for the long-range coulombic interactions between defects is still a subject of controversy. The calculations presented here are overestimates of the defect concentrations, but without a well-accepted non-dilute defect chemistry formalism are a good first approximation.

The point defect concentrations at 1500°C in air as a function of Gd^{3+} doping were calculated using previously published values for the various defect reactions in ceria (Table 2.1) and the condition of electroneutrality. The association of oxygen vacancies,

$V_O^{\bullet\bullet}$, with Gd^{3+} substitutional defects, Gd'_{Ce}, was included in the calculation, although only "dimers" of one oxygen vacancy and one Gd^{3+} ion were considered. Larger defect clusters were not included since theoretical calculations show they are energetically unstable with respect to the dimers [43,71]. From Figure 2-2, the majority defects in Gd^{3+} doped ceria are e', $V_O^{\bullet\bullet}$, Gd'_{Ce}, and $(Gd'_{Ce} - V_O^{\bullet\bullet})^{\bullet}$ dimers. For samples containing $\geq 1\%$ Gd, the electron concentration is much smaller than the concentration of Gd'_{Ce} so the electronic space charge can be ignored. At lower temperatures, the bulk defect chemistry will be even more dominated by the extrinsic concentration of solute atoms and their compensating oxygen vacancies.

Figure 2-3 shows the calculated defect concentrations as a function of Ta content at 1500°C in air. The majority defects in Ta^{5+} doped ceria are e', $Ta_{Ce}^{\bullet}$, and $V_O^{\bullet\bullet}$. Under the experimental conditions for which the defect chemistry was solved, the most important defect reaction is the reduction of the ceria lattice to produce electrons and oxygen vacancies. Although Ta^{5+} doping has the effect of decreasing the concentration of oxygen vacancies, the samples are still overall oxygen deficient under the conditions considered. $Ta_{Ce}^{\bullet}$ in these compositions serves as a charged solute tracer by which the near boundary defect concentrations may be inferred.

The bulk defect chemistry of ceria co-doped with both Gd^{3+} and Ta^{5+} was also solved. Figure 2-4 shows the calculated defect concentrations of e', $h^{\bullet}$, $V_O^{\bullet\bullet}$, O''_i, and the net dopant concentration as a function of net Gd doping from -4% to $+4\%$. We have defined the net dopant concentration as % Gd $-$ %Ta. The predominant defects at 1500°C in air are, e', $V_O^{\bullet\bullet}$ and the dopants. The most important defect reaction is the reduction of the ceria lattice to produce electrons and oxygen vacancies. Association of Gd'_{Ce} and $Ta_{Ce}^{\bullet}$ was also considered. Calculating the coulombic interaction of the two charged defects assuming they lie at nearest neighbor cation sites gives a value of 0.151eV for the

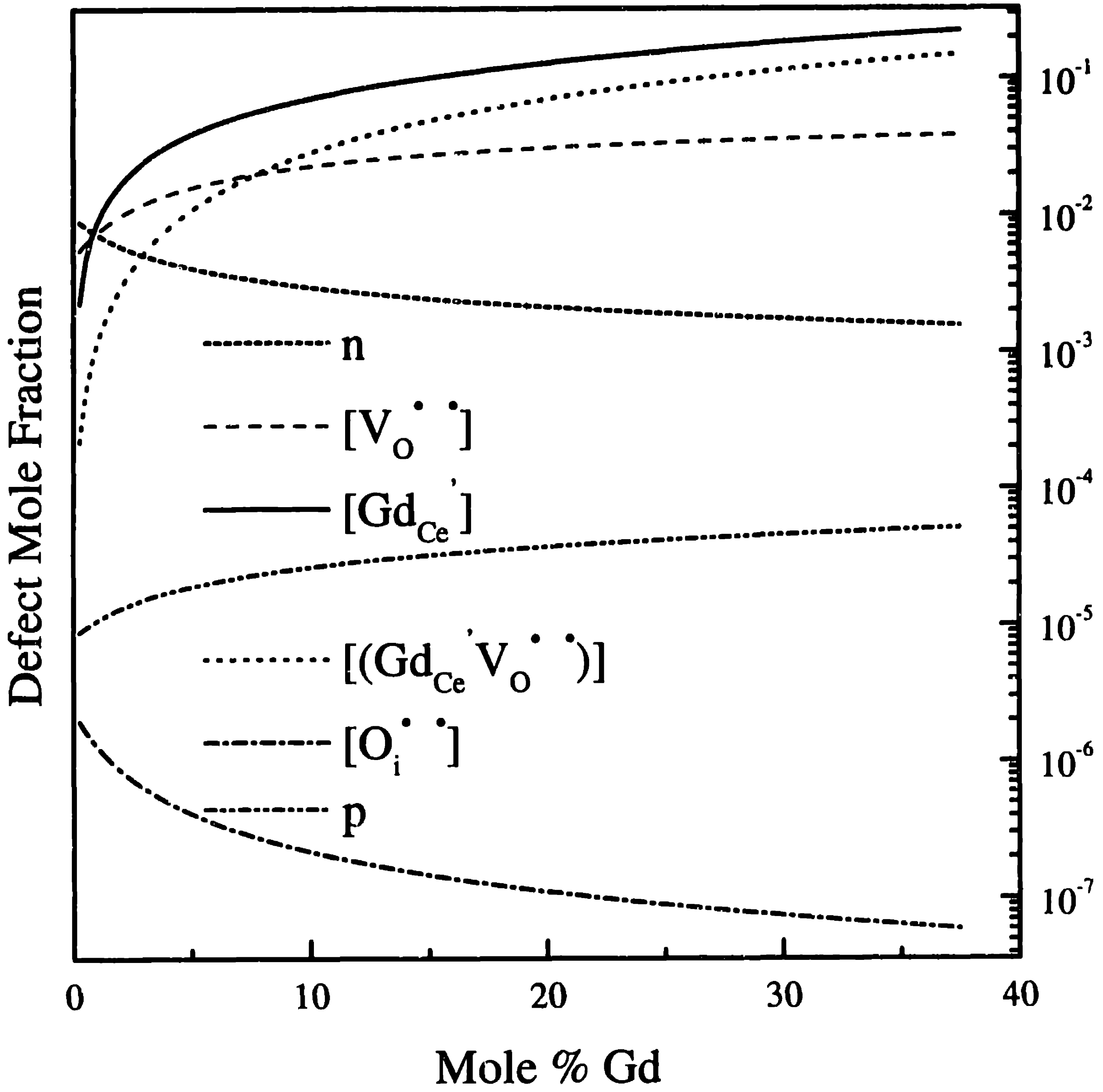

Figure 2-2: Defect mole fractions in Gd^{3+}-doped ceria versus mole% Gd at 1500°C in air.

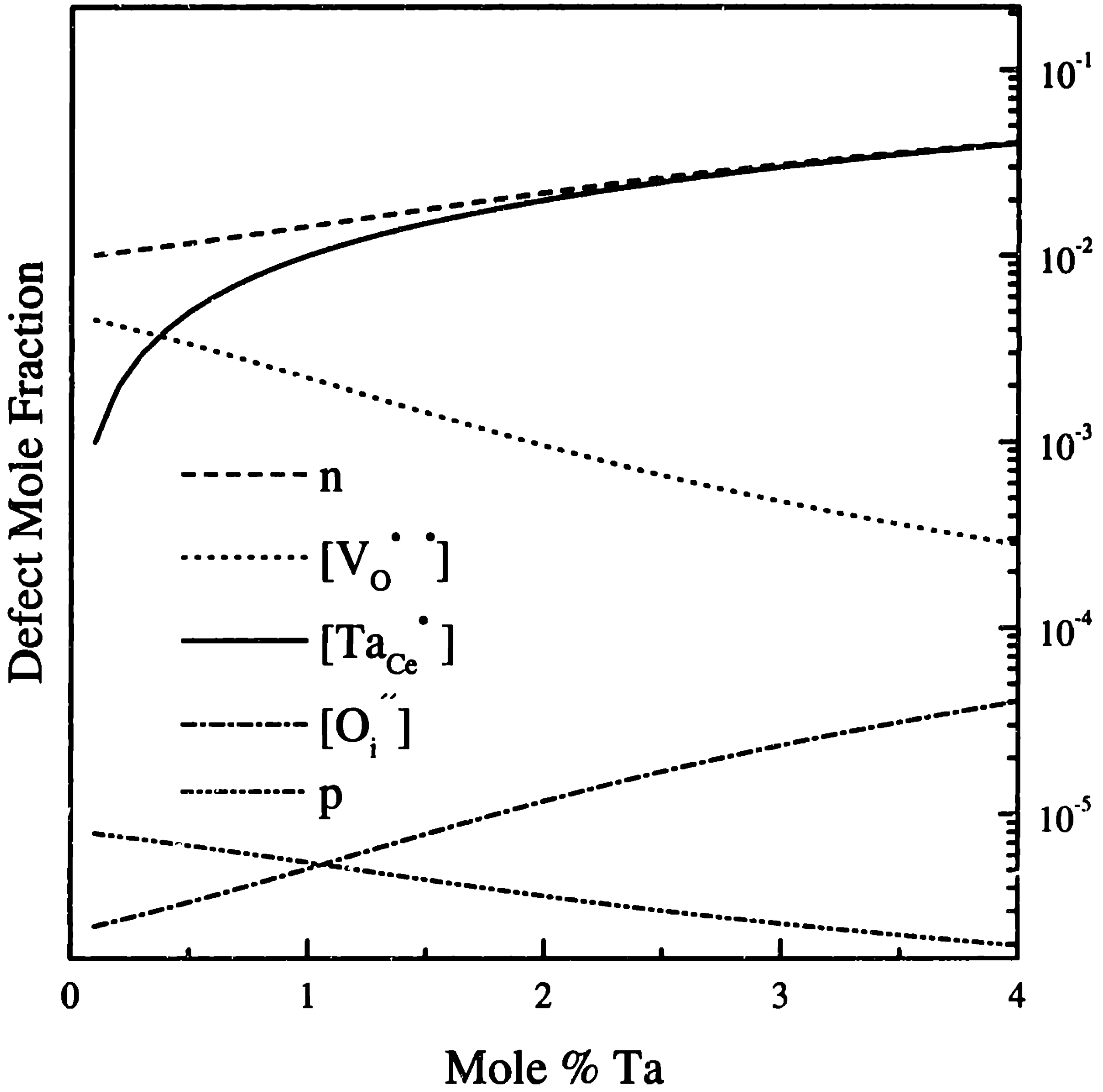

Figure 2-3: Defect mole fractions in Ta^{5+}-doped ceria as a function of mole% Ta at 1500°C in air.

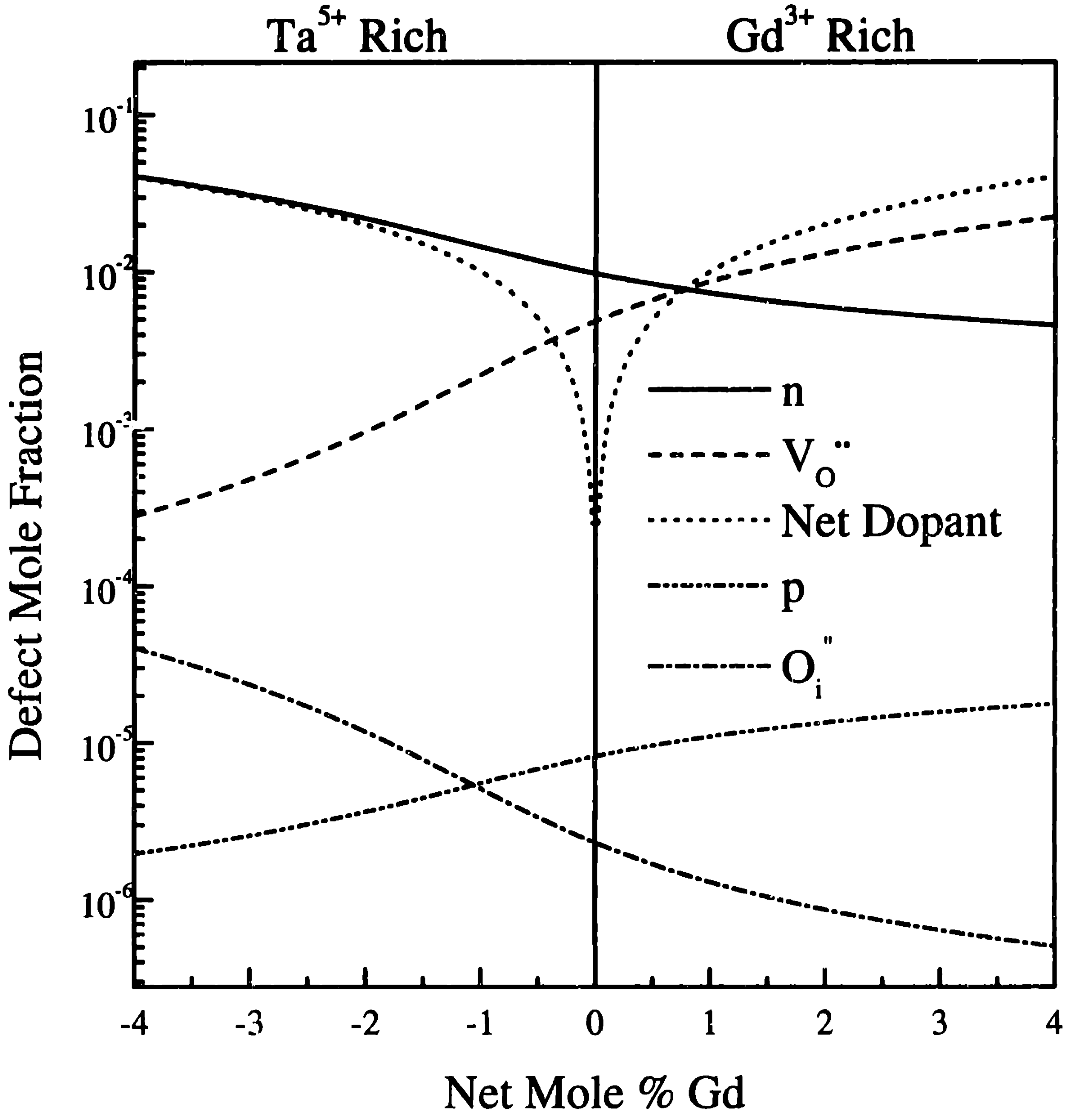

Figure 2-4: Defect mole fractions vs. net % Gd in ceria co-doped with Gd^{3+} and Ta^{5+}.

association energy. At 1500°C the association is negligible for the compositions studied.

2.3 Solid State Adsorption

2.3.1 Langmuir Adsorption

Alternative models of interfacial segregation are solid state analogues of gas phase adsorption. The simplest of these is a Langmuir adsorption isotherm. The free energy of the system can be written as:

$$G = n_{gb}E_{gb} + n_{bulk}E_{bulk} - TS_c \tag{2.26}$$

where n_{gb} is the number of independent sites at the interface, E_{gb} is the energy of the solute sitting at a interfacial site, n_{bulk} is the number of bulk sites, E_{bulk} is the energy of the solute sitting at a bulk site, and S_c is the configurational entropy associated with the partitioning of the solute between bulk and interfacial sites. Note the similarity with Equations 2.1 and 2.17. Minimizing the free energy with respect to the site occupations leads to:

$$\frac{X_{gb}}{X_{gb}^{sat} - X_{gb}} = \frac{X_{bulk}}{1 - X_{bulk}} \exp\left(\frac{-\Delta G}{kT}\right) \tag{2.27}$$

where X_{gb}^{sat} is the composition of the interface at saturation, X_{gb} is the mole fraction of solute at the interface, X_{bulk} is the bulk solute molar fraction, and ΔG is the free energy of segregation per solute atom. For most systems, this energy is < 0 and segregation of solute is predicted. Typically, X_{gb}^{sat} is assumed to be equal to 1, which implies that the solute can fully substitute for the matrix at the interface. Equation 2.27 assumes

Table 2.2: Ionic radii and estimated enthalpy of segregation for various elastic constants of ceria

Ion	Radius (pm) [76]	ΔH_ϵ (eV)		
		K= 210 GPa [77]	K= 357 GPa [78]	K= 5.977 GPa [79]
Ce^{4+}	111			
Gd^{3+}	119.3	−0.065	−0.110	−0.002
Ta^{5+}	88	−0.445	−0.757	−0.013

that the solute ions do not interact with each other, and that every interfacial site has the same energy. Solute segregation is assumed to occur at the first atomic plane at the interface. More nuanced models which allow for multi-layer adsorption, interaction among segregating species, and non-ideal behavior exist as analogues from the field of gas phase adsorption. [72, 73].

McLean [74] equated the enthalpy of segregation, ΔH_ϵ, to the relaxation of the elastic misfit energy of a solute. An over- or under-sized solute atom in the bulk has an elastic energy component due to bond distortion which can be estimated by [75]:

$$\Delta H_\epsilon = \frac{-24\pi K G R_{matrix} R_{solute} (R_{solute} - R_{matrix})^2}{4 G R_{matrix} + 3 K R_{solute}} \tag{2.28}$$

where R_{solute} and R_{matrix} are the appropriate ionic radii of the solute and matrix, K is the bulk modulus of the solute, and G is the shear modulus of the matrix. Table 2.2 lists the ionic radii for Ce^{4+}, Gd^{3+} and Ta^{5+} in eight-fold coordination [76], along with the estimate of the enthalpy of segregation due to elastic misfit. Atkinson has published a value of 210 GPa for the Young's modulus of ceria doped with 20 mole % Gd [77]. Additionally, two separate theoretical calculations of the bulk modulus of pure ceria have been performed [78, 79]. Hill and Catlow calculated a value of 357 GPa, while

Andrés and Beltrán results gave 5.977 GPa. For an isotropic solid, the bulk modulus, shear modulus, Young's modulus and Poisson's ratio are simply related [80]. No elastic constants have been published for gadolinia or tantala. Therefore, the elastic constants of ceria have been used to estimate the strain enthalpy for Gd^{3+} and Ta^{5+} in ceria. Poisson's ratio for ceria was assumed to be 1/3. ΔH_ϵ for Gd^{3+} is ≤ -0.11 eV while ΔH_ϵ for Ta^{5+} is ≤ -0.76 eV. The larger size misfit of the Ta^{5+} ion is responsible for the much larger strain enthalpy.

2.3.2 Guttmann and McLean Model for Ternary Adsorption

Guttmann and McLean have developed a series of models for segregation of solutes in multi-component systems [81]. The most applicable to the simultaneous segregation of Gd^{3+} and Ta^{5+} in ceria is a regular solution model with site competition between the two solutes. The two solutes are labeled M and I and it is assumed that solute I segregates more strongly to the interface than solute M.

Since both Gd'_{Ce} and $Ta^{\cdot}_{Ce}$ are substitutional defects on the Ce^{4+} site, we expect these two solutes to compete for the same interfacial sites. The relevant equations to describe this behavior are [81]:

$$\frac{X_i^{gb}}{X_{Ce}^{gb}} = \frac{X_i^{bulk}}{X_{Ce}^{bulk}} \exp\left(\frac{-\Delta G_i}{kT}\right) \tag{2.29}$$

where X_i^{gb} is the mole fraction of solute i at the interface, which we limit to be $\leq X_i^{sat}$ the saturation level of solute i at the interface, X_i^{bulk} is the bulk solute molar fraction, and ΔG_i is the free energy of segregation per atom for solute i. ΔG_i in a ternary system with site competition may be written as:

$$\Delta G_I = \Delta G_I^\circ - \alpha(X_M^{gb} - X_M^{bulk}) \tag{2.30a}$$

$$\Delta G_M = \Delta G_M^\circ - \alpha(X_I^{gb} - X_I^{bulk}) \tag{2.30b}$$

where ΔG_i° is the standard free energy of segregation for solute i in a binary solid solution of i and the majority element (Ce^{4+} in this case) and α is the energy of interaction between solute I and solute M. Guttmann and McLean defined a negative interaction coefficient as a repulsive force. Equation 2.30 assumes that segregation does not change the driving force for additional segregation, that solute I ions do not interact with other solute I ions and solute M ions do not interact with other solute M ions. From the results of segregation of Gd^{3+} and Ta^{5+} in ceria, best-fits of ΔG_{Gd}° ΔG_{Ta}°, X_{Gd}^{sat} and X_{Ta}^{sat} can be determined. α is estimated by the coulombic interaction energy when Gd'_{Ce} and $Ta^{\cdot}_{Ce}$ are nearest cation site neighbors, which is equal to $0.151eV$. Typically, a calculation of this type which does not allow for ion relaxation provides an overestimate of the interaction between the two ions.

As we will show, the segregation isotherms corresponding to Equations 2.27 and 2.29 are very similar to those due to the space charge models. Comparing the adsorption and space charge segregation models, it is clear that both predict segregation of acceptors such as Gd'_{Ce} in ceria. Qualitative observations of grain boundary segregation are not sufficient to unequivocally identify the mechanistic cause. In order to test the applicability of space charge models to a particular ceramic system through measurement of aliovalent solute grain boundary segregation, defect chemical calculations must be coupled with the analysis outlined previously in Section 2.1.1. Only by comparing the segregation tendencies of oppositely charged defects is it possible to determine whether that a space charge model is an accurate representation of the segregation mechanism.

Chapter 3

Experimental Procedure

The experiments were designed to probe the driving force(s) for aliovalent solute segregation in heavily doped ceria. A series of Gd^{3+} doped samples containing between 1 and 26 mole % Gd, Ta^{5+} doped samples containing between 0.28 and 1.79 % Ta, and co-doped samples containing between 0.8 % and 4.2 % Gd and between 0.9 % and 1.9 % Ta, were measured in order to compare experimental grain boundary segregation isotherms with the two space charge models, as well as a number of adsorption models. The solutes vary in both their effective charge and their size misfit with the host cerium ion.

From the single dopant data, the dominant driving force for Gd^{3+} and Ta^{5+} segregation in ceria may be determined. Adsorption models predict that both Gd^{3+} and Ta^{5+} should segregate to the grain boundaries in ceria. From an elastic misfit viewpoint, Ta^{5+} should segregate more strongly. If space charge effects dominate the behavior of both Gd^{3+} and Ta^{5+} in ceria, it is expected that Gd^{3+} will segregate, while Ta^{5+}, with opposite effective charge, will deplete from the near interface region. Segregation of both solutes would indicate that an electrostatic driving force does not dominate the grain boundary segregation of one or both of the solutes in ceria.

Table 3.1: Predicted segregation of Gd^{3+} and Ta^{5+} in co-doped ceria

Solute	Ta^{5+}-rich		Gd^{3+}-rich	
	Space charge	Adsorption	Space charge	Adsorption
Ta^{5+}	Slightly more Ta^{5+} depletion	More segregation than in binary solid solution	Slightly less Ta^{5+} depletion	More segregation than in binary solid solution
Gd^{3+}	Slightly less Gd^{3+} segregation	Less Gd^{3+} segregation	Same as Gd^{3+} doped	Less Gd^{3+} segregation

Table 3.1 shows the predictions of the space charge models and Guttmann and McLean's ternary adsorption model applied to co-doped ceria for both Gd^{3+} rich and Ta^{5+} rich compositions. Reference is to a singly doped sample with an equal amount of either Gd^{3+} or Ta^{5+}. The space charge models predict that the amount of Gd^{3+} segregation in samples co-doped with both Gd^{3+} and Ta^{5+} will not change significantly. Samples with an excess of Ta^{5+} in the bulk will have slightly less Gd^{3+} segregation. The ternary adsorption model on the other hand, predicts significantly less Gd^{3+} segregation in co-doped compositions. Competition by Ta^{5+} for interfacial sites reduces the expected segregation of Gd^{3+}.

Guttmann and McLean's ternary adsorption model predicts more Ta^{5+} segregation in ternary solutions than in binary solutions of Ta^{5+} in ceria. The positive interaction between $Ta_{Ce}^{\cdot}$ and Gd'_{Ce} effectively increases the adsorption energy of Ta^{5+} as can be seen by inspection of Equation 2.30a. Even assuming a zero interaction energy between Ta^{5+} and Gd^{3+}, the site competition effect favors additional Ta^{5+} at the expense of Gd^{3+}. The space charge models are complicated by the interplay between the overall charge on the interface and the Debye length. For Gd^{3+} rich compositions, the large increase in the number of charged defects and subsequent decrease in the Debye length leads to a prediction of slightly less Ta^{5+} depletion than in a binary solution. For Ta^{5+}-rich compositions, the increased charge on the interface creates a larger depletion driving force which is not overcome by the decreased Debye length, and the space charge models predict slightly more depletion of Ta^{5+}.

3.1 Powder Preparation

Homogeneous ceria powders doped with various amounts of Gd and Ta were prepared by the thermal decomposition of mixed organometallic precursors. To minimize Si contamination, all powder processing steps were carried out in polypropylene containers. Table 3.2 details the compositions studied in this work, along with the Si impurity level. The chemical compositions were measured using Inductively Coupled Plasma (ICP) emission spectroscopy (UOP Inc. Tarrytown, NY and Luvak Inc. Boylston, MA).

Gadolinium acetate, cerium acetate, and tantalum tetraethoxide-2,4-pentanedionate (Johnson Matthey/Alfa Aesar,Ward Hill, MA) precursors were mixed overnight in 300 ml of deionized water with a resistivity of $\geq$ 17.9 Mohm-cm. The resulting solutions were atomized directly into liquid nitrogen and then placed in a freeze drier (Virtis Consol 25, Gardiner, NY). A mechanical rotary pump was used to evacuate the chamber to 10^2 Pa. Over a period of several days, the temperature of the powder was increased from ≈ -45°C to room temperature. As the temperature of the powder was raised, the excess water was sublimated, yielding 4–5 grams of finely dispersed, molecularly mixed organometallic powders.

0.2 to 0.3 grams of the mixed powder was then calcined in a small box furnace in air to convert the material to a doped oxide sample. Calcination was conducted by ramping the furnace at 20°C/min to 700°C and then immediately furnace cooling back to room temperature. The various precursors all decomposed below 500°C. Platinum foil lined

Table 3.2: Compositions

Sample Identification	Gd Mole Fraction	Ta Mole Fraction	Si Impurity Mole Fraction
Gd1	0.0128		0.0001
Gd2	0.0176		0.0032
Gd3	0.0187		0.0019
Gd4	0.0485		0.0086
Gd5	0.0757		0.0080
Gd6	0.2372		0.0014
Gd7	0.2571		0.0080
Ta1		0.0028	0.0002
Ta2		0.0053	0.0535
Ta3		0.0179	0.0038
CGT1	0.0154	0.009	6.74×10^{-5}
CGT2	0.0421	0.0152	0.001
CGT3	0.0148	0.0189	$\leq 1.23 \times 10^{-4}$
CGT4	0.0081	0.0182	0.001

high purity alumina boats with covers were used to limit contamination.

3.2 Sample Fabrication

The oxide powders were deagglomerated by shaking a teflon ball in a polypropylene vial containing the powder. 6 mm diameter pellets were produced by uniaxially pressing the deagglomerated powder at 110 MPa in a stainless steel die. The surfaces of the cold-pressed pellets were removed to eliminate contamination from the steel die and rams. The green density was between 30 and 40% of the theoretical density for ceria.

The green pellets were placed on a platinum mesh and lowered into a vertical-tube furnace. A pre-sintering heat treatment at 500°C for 8–12 hours was performed in order to ensure complete degassing of the ceramic compacts. The ceramic sample was then quickly lowered into the hot zone of the furnace which had stabilized at 1500°C. After 6 hours, the sample was air-quenched from 1500°C to room temperature. The final density of each sample was measured using the Archimedes's technique with deionized water. All samples prepared had a final density $\geq 90\%$ of the theoretical value.

Specimens suitable for examination by transmission electron microscopy were then prepared from the fired pellets. Slices were cut from the pellets with a low speed diamond saw (Buehler Isomet, Evanston, IL) and polished to ≈ 25 μm thickness. For specimens containing Ta, a Mo washer was epoxied to the ceramic. For all other specimens, a Cu washer was epoxied to the specimens. The Cu K_α X-ray lines overlap with the Ta L_α lines making X-ray compositional analysis extremely difficult. By eliminating the overlap, the accuracy of the subsequent data analysis was greatly enhanced. Final two-sided argon ion thinning (Gatan Duomill 600, Warrendale, PA) of the ceramic was done on liquid nitrogen cooled samples at 6kV and 0.5mA gun current.

3.3 STEM Characterization

The grain boundary excess of dopant, Γ_{dopant}, was quantified with a Vacuum Generators HB603 Scanning Transmission Electron Microscope (STEM) fitted with a windowless PentaFET X-ray detector (Oxford Link, Concord, MA) using the area-scan technique developed by Ikeda *et al.* [48, 49, 61, 82]. Between 10 and 33 separate grain boundaries were measured for each composition. For every composition, the spectra were collected with an equal number of counts on the Ce L_{α_1} line at 4.840 keV. X-ray spectra were collected from defined volumes of the specimen (32 nm square raster area), both at the grain boundary and in the bulk of the grains. Figure 3-1 illustrates the placement of the raster areas.

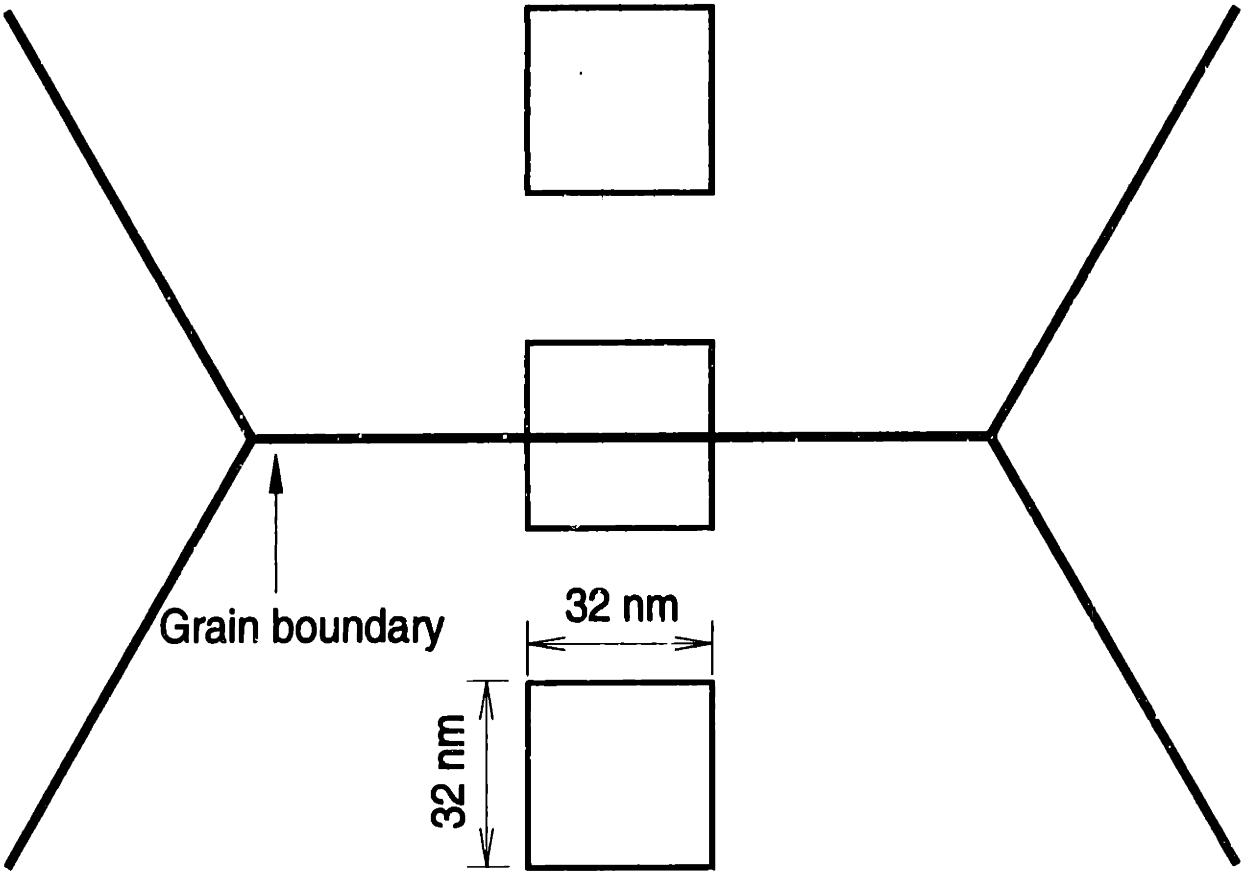
Grain boundary
32 nm
32 nm

Figure 3-1: Schematic of the STEM microanalysis technique, showing the location of the rastered areas used to quantify the excess solute coverage at a grain boundary.

The grain boundary excess is calculated as follows:

$$\Gamma_{dopant} = \frac{1}{2}\left[\frac{\frac{I_{dopant}}{I_{Ce}}^{gb} - \frac{I_{dopant}}{I_{Ce}}^{grain}}{\frac{I_{dopant}}{I_{Ce}}^{grain}}\right] C^{bulk}_{dopant} N w \qquad (3.1)$$

where I_x is the integrated X-ray line intensity for element x, C^{bulk}_{dopant} is the bulk chemical composition of the specimen as measured by ICP emission spectroscopy, N is the cation site density of ceria (2.5×10^{28} atoms/m^3), and w is the width of the rastered area. The factor of one half is necessary to account for the segregation associated with the two grains. For Equation 3.1 to apply, the grain boundary must not be tilted with respect to the electron beam direction. Grain boundaries throughout a sample were chosen for analysis based on the degree to which the grain boundary plane was parallel to the electron beam.

The L series of X-ray lines were used to quantify the Ce, Gd, and Ta content of the samples. The integrated line intensities for each element were calculated using the RTS2 analysis program supplied by Link. The RTS2 program set the gain factor of the detector so that the Ce L_{α_1} line was centered at 4.840 keV, stripped the background from the spectrum and then fit the spectrum to a series of standard spectra for each element analyzed. The standard spectra were experimentally collected from pure oxides using the same microscope and X-ray detector. $\frac{I_{dopant}}{I_{Ce}}^{grain}$ in Equation 3.1 was the average of the two grain measurements in order to correct for any small inhomogeneities in the bulk composition. Each reported grain boundary excess is therefore the difference in composition between the bulk of the grain and the near grain boundary region.

The X-ray mass absorption coefficients were calculated from published data [83] and found to vary between 1.002 and 0.998 for 100 nm thick Gd-doped samples (1–100% Gd). Compositional differences between the bulk and grain boundary could account for no more than a 0.5% correction to the integrated line intensities for Gd^{3+} doped samples. The mass absorption coefficients for 100 nm thick Ta^{5+} doped samples varied from 0.999 to 0.994 for doping levels from 0–100% Ta. At most, a 0.6% correction would be required. Corrections for co-doped samples were also calculated. It was assumed that the concentration of either solute would not increase above 100% at the interface. The corrections necessary account for no more than 0.6%. The effect of thickness variation was also considered. For the compositions studied, varying the thickness between 50 nm and 150 nm creates a 0.3% change in the Gd mass absorption correction and a 0.06% change in the Ta correction. Therefore, no mass adsorption correction was necessary for the compositions considered here for reasonable thickness variation.

The error due to X-ray counting statistics was quantified experimentally for every sample and measurement condition. The area scan of a grain was measured 10 times consecutively. No systematic variation was observed in the I_{Gd}/I_{Ce} or I_{Ta}/I_{Ce} ratio during these measurements, indicating that beam induced composition changes were minimal at this exposure. The error in the measured X-ray intensity ratios was therefore assumed to be due strictly to counting statistics. Student's t-test was applied to the data in order to define a 95% confidence limit:

$$Error_{relative} = t^* \frac{\frac{S}{\sqrt{10}}}{\mu} \tag{3.2}$$

$Error_{relative}$ is the error of the measurement relative to the mean of the ratio of integrated X-ray intensities, I_{dopant}/I_{Ce}. t^* is the 95% critical limit from Student's t-test with nine degrees of freedom. S is the standard deviation of the ratio I_{dopant}/I_{Ce} for the ten measurements. μ is the mean of the integrated intensity ratios. The relative error can be converted to an error in terms of atoms/m^2 or equivalent monolayers by multiplying by the chemical composition of the grain *i.e.*, using ICP analyzed concentrations and the volume of analysis. In order to determine the volume analyzed, the scan area and thickness must be known. The scan area was directly measured, while the thickness was estimated to be 100 nm in all cases.

When the measured composition of the two grains is significantly different, the ability to measure a grain boundary excess per unit area is compromised. If the ratio of I_{dopant}/I_{Ce} from the two different grain measurements was <0.90 or >1.10, the data from that measurement was excluded from further analysis. Less than 15% of the total number of measurements were affected by this criterion. The variation may represent a real composition fluctuation, a large thickness variation, or the counting statistics of the measurement. The more lightly doped samples exhibited more such cases, suggesting the variation was due to the counting statistics. Grain boundaries for which the measured excess was less than the counting statistics error associated with the measurement were not included in the calculation of the average grain boundary segregation for that composition. Only a few "special" boundaries exhibited grain boundary excess below the confidence limits of the experiment.

Chapter 4

Results

4.1 Gd^{3+} Segregation in Singly Doped Ceria

In order to test whether the area scan method captures all the dopant segregation, a series of point probe measurements were made as a function of distance from a grain boundary in sample Gd7. The results are shown in Figure 4-1. The composition at each point was calculated from the integrated line intensities using the Cliff-Lorimer equation [84]:

$$\frac{C_A}{C_B} = k_{AB}\frac{I_A}{I_B} \tag{4.1}$$

where C_A and C_B are the weight fractions of A and B, k_{AB} is referred to as the k-factor and I_A and I_B are the integrated X-ray intensities of elements A and B. The k-factor was experimentally determined from the average X-ray intensity ratios for the area scans of the grains. The error bars are 95% confidence limits following the derivation of Furdanowicz [85]. The Gd^{3+} concentration peaks at the grain boundary with an apparent composition of 38.3 mole % Gd. Excess Gd^{3+} exists within ±5 nm of the grain boundary. The area scan includes the grain boundary ±16 nm, and therefore all of the Gd^{3+} grain

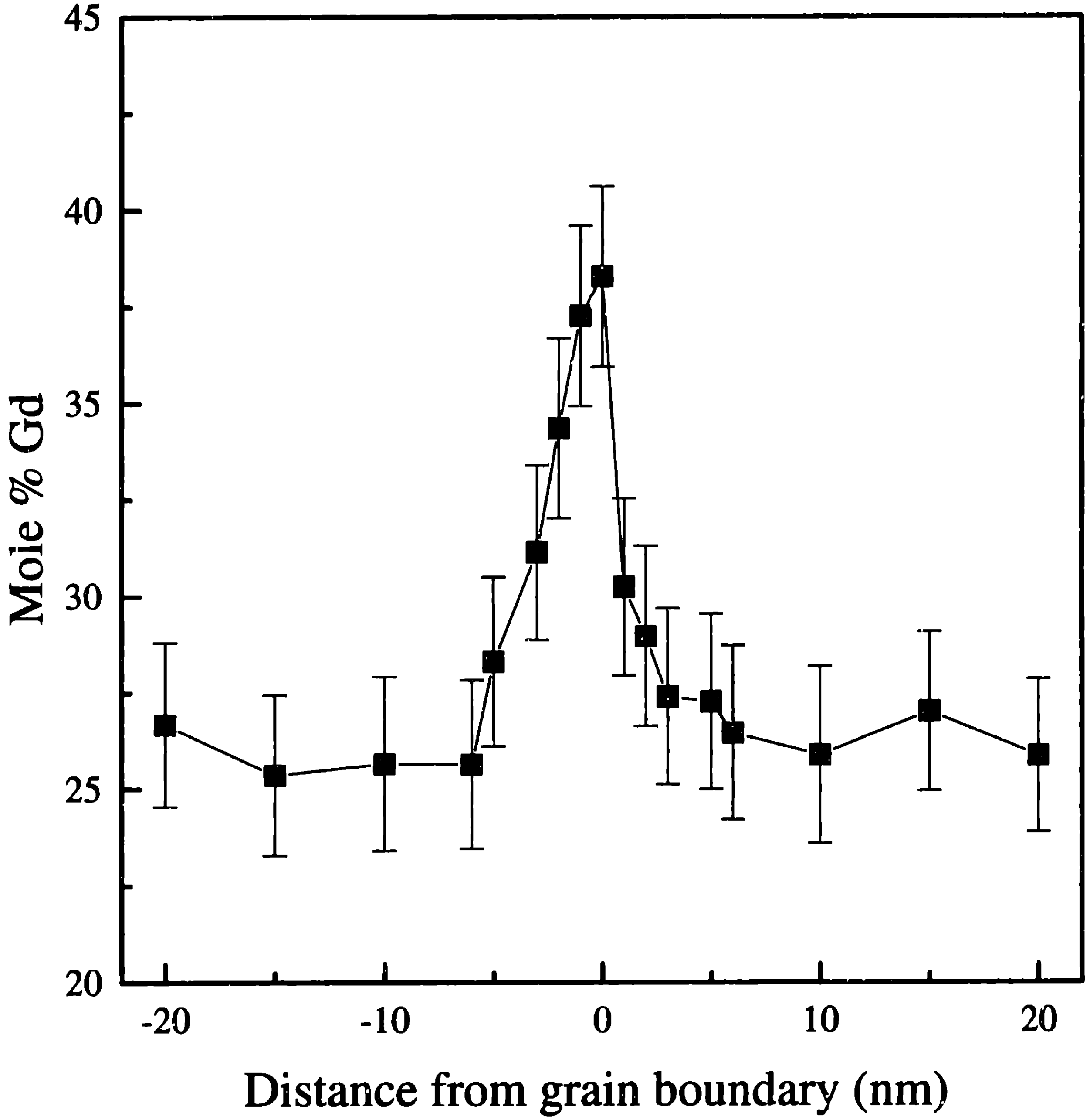

Figure 4-1: X-ray line-scan across a grain boundary in sample Gd7. Gd^{3+} segregation exists within ±5 nm of the boundary.

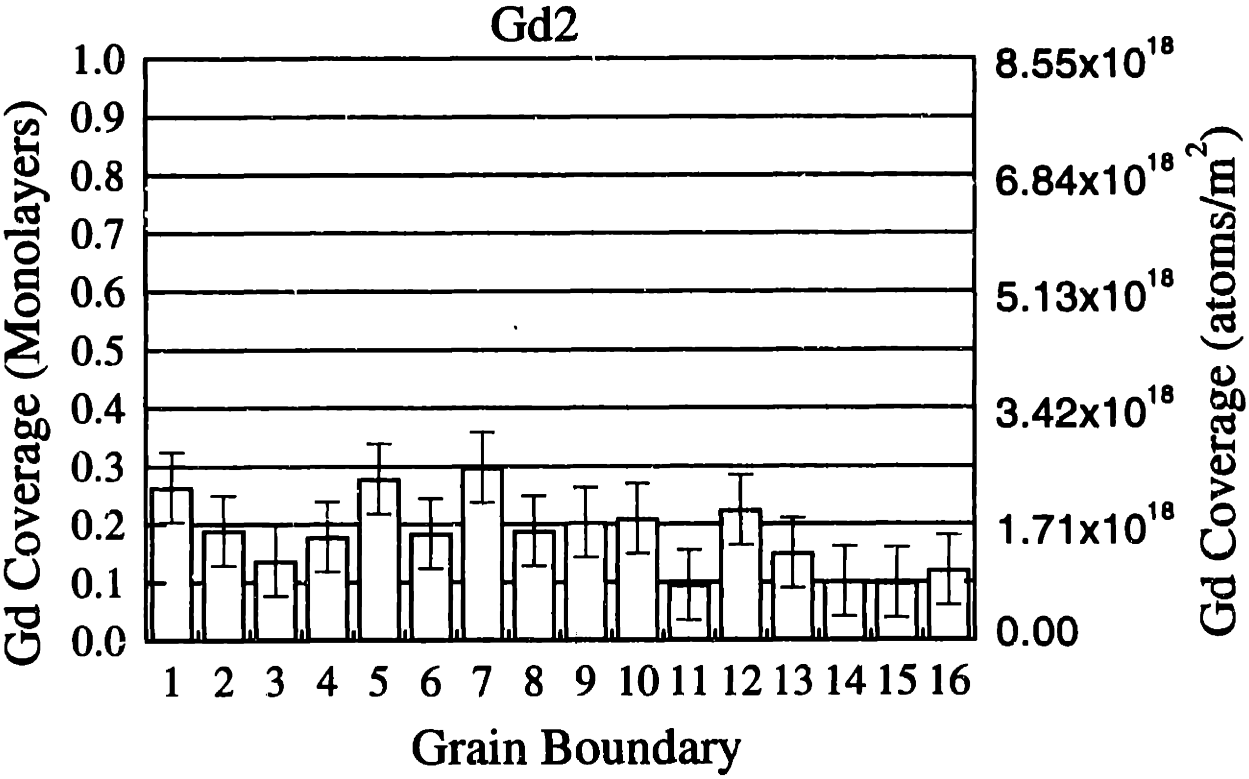

Figure 4-2: Grain boundary segregation at 16 different boundaries in Gd2. Error bars are derived from counting statistics error.

boundary segregation.

STEM measurements of Gd^{3+} grain boundary segregation were performed on 199 different grain boundaries in 7 different Gd compositions. Figures 4-2 and 4-3 show the excess of Gd^{3+} measured at 16 separate boundaries in sample Gd2 and 23 boundaries in Gd7. Equation 3.1 was used to obtain the integrated excess of Gd at each particular boundary from the X-ray data. The excess in terms of atoms per square meter was converted into equivalent monolayers by dividing by the average cation site density in ceria ($N^{2/3} = 8.55 \times 10^{18}$ atoms/m^2). The error bars come from the error analysis described in Section 3.3. As can be seen from Figures 4-2 and 4-3, the precision of the measurement of Γ_{Gd} is quite high. By rastering over a well-defined volume, the statistical precision

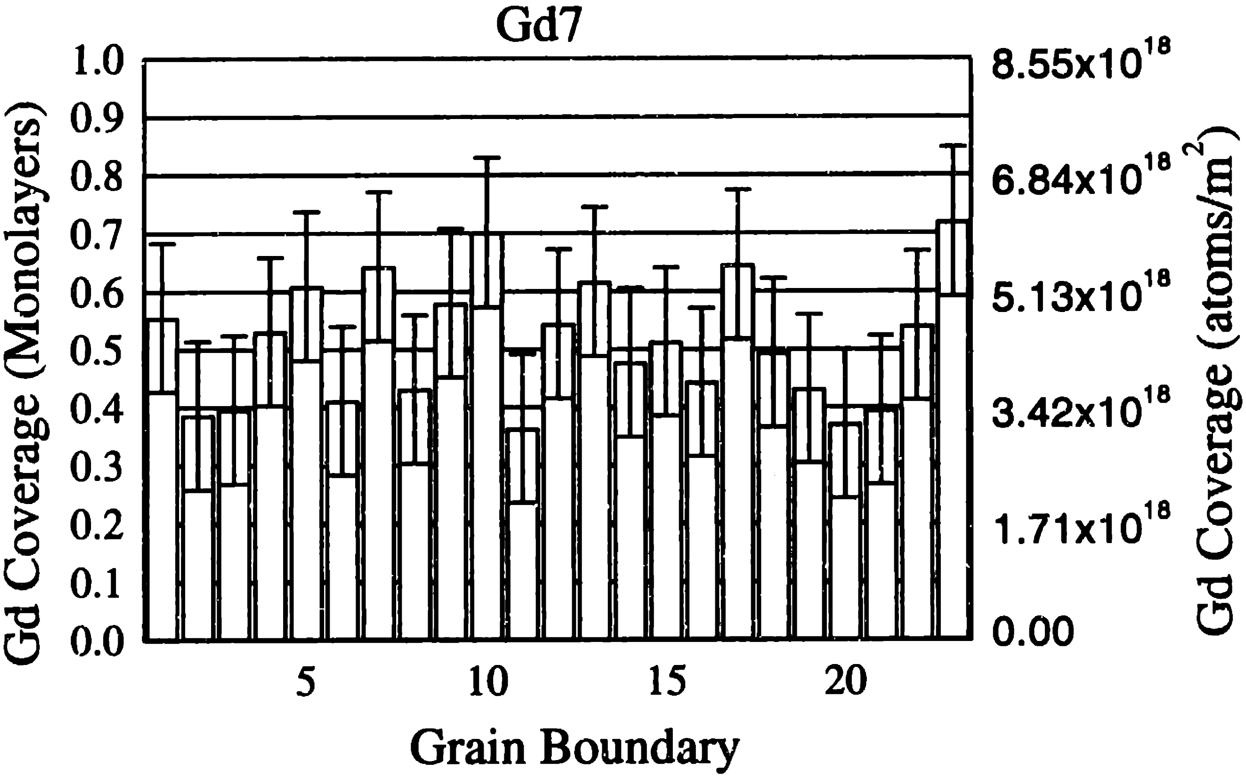

Figure 4-3: Grain boundary segregation at 23 different boundaries in Gd7. Error bars are derived from counting statistics error.

of the composition measurement is enhanced at the expense of spatial information. The average Gd^{3+} excess in sample Gd2 is 0.18 monolayers (1.6×10^{18} atoms/m^2), and in Gd7, 0.51 monolayers (4.5×10^{18} atoms/m^2). The excess of Gd^{3+} for a single composition, temperature and oxygen partial pressure varied somewhat from grain boundary to grain boundary. This is reasonable since the details of grain boundary structure will affect the energetics of grain boundary sites [73]. The average segregation in each sample was used to construct the segregation isotherm for Gd^{3+} in ceria. These data were then compared to the two space charge models as well as the Langmuir adsorption isotherm. The energetics derived from the models represent not a particular grain boundary structure, but values typical of high-angle general grain boundaries in ceria.

Figure 4-4 shows the measured segregation isotherm of Gd^{3+} doped ceria at 1500°C in air over the concentration range 1–26% Gd. The ordinate records excess gadolinium in terms of monolayers of coverage. Each data point is the average of between 5 and 23 measurements. Submonolayer segregation was seen at every measured boundary. The average Gd^{3+} grain boundary segregation ranged from 0.1 to 0.5 monolayers for samples containing between 1% and 26% Gd. Two curves are shown in Figure 4-4. They are fits to the experimental data using the space charge models applied to ceria from Section 2. The dilute space charge model was fit to the data with one adjustable parameter, $g_{V_O^{\cdot\cdot}}$. The model assumes that $g_{V_O^{\cdot\cdot}}$ has a single value for all interfacial sites and is not a function of composition. The limited site model also assumes that $g_{V_O^{\cdot\cdot}}$ has a single, composition independent value. For the limited-site model, which explicitly considers the configurational entropy of the interface, an additional parameter, N_s, the total number of available interfacial sites, is necessary. The fit shown in Figure 4-4 is for $N_s = (1/2)(2N)^{2/3}$. This corresponds to 1/2 of the oxygen sites in a monolayer being vacant. Considering both grains, this condition allows for the complete absence

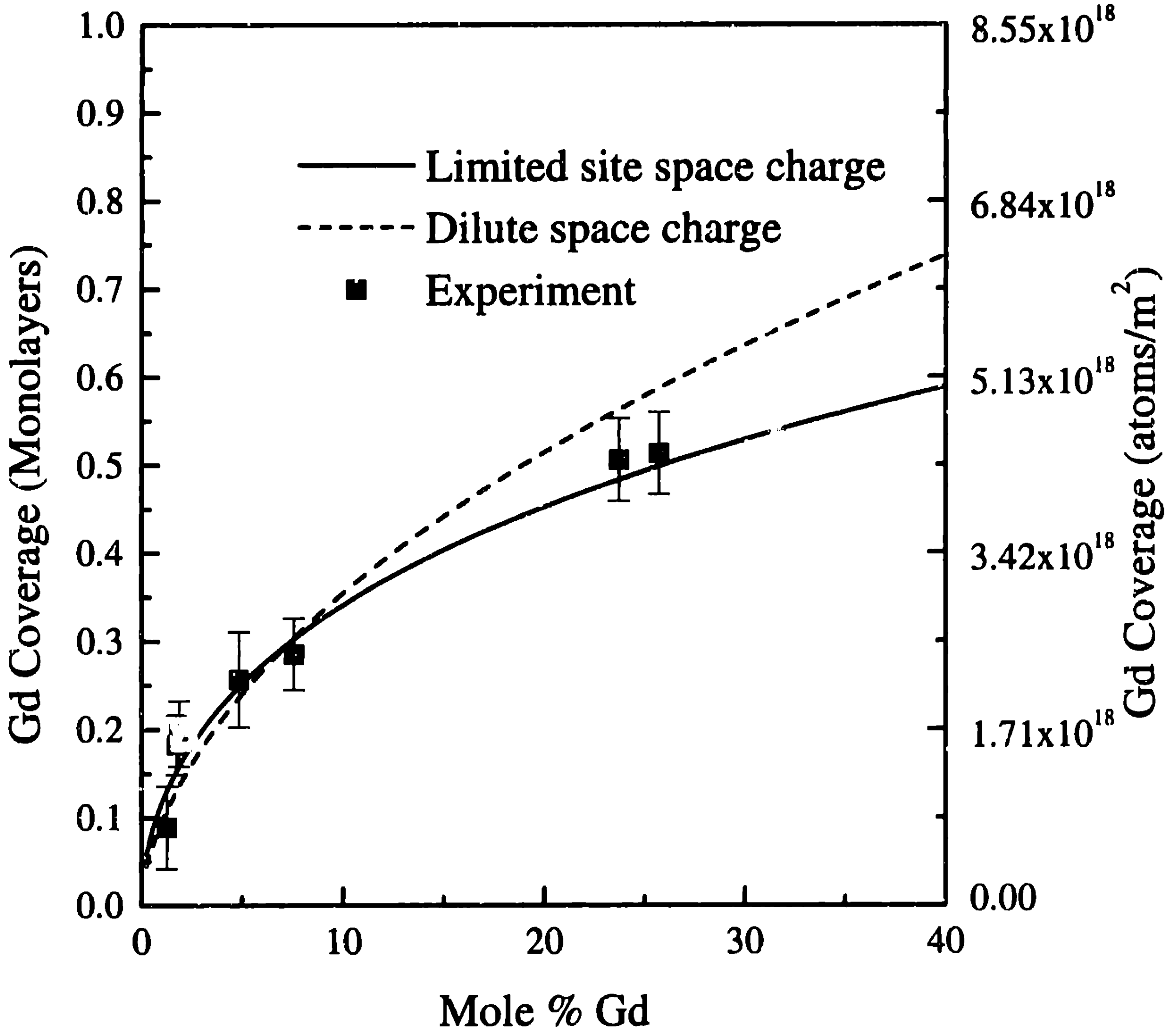

Figure 4-4: Gd^{3+} segregation isotherm at 1500°C in air. The experimental points are averages from the individual measurements and the error bars are 95% confidence limits from Student's t-test. The two curves are fitted using a dilute space charge model and a limited-site model.

of all oxygen ions in a single atomic layer. At low concentrations, both models fit the experimental data equally well, within the error of the measurements. As discussed in Section 2, the limited-site model reduces to the dilute solution model when the surface charge density, σ, is small. At higher concentrations, however, the dilute solution model predicts segregation that exceeds the measured value. This model cannot be adjusted to simultaneously fit both the low and high concentration data. At high doping levels, the assumption that the interface can act as an infinite source or sink for defects becomes unrealistic and is observed in the dilute space charge model as a divergence between the model and experimental data.

On the other hand, the limited-site model can be fit well over the entire concentration regime. This is the first experimental evidence that a limited-site space charge model will accurately reproduce an experimental isotherm where the standard dilute solution space charge model will not. A series of fits of the limited site model to the data are shown in Figure 4-5. The value of N_s was varied from 1/8 to 1/2 of the oxygen site density (1.69×10^{18} to 6.79×10^{18} atoms/m^2). Except for $N_s = 1/8$ of the oxygen sites, the assumption of N_s does not significantly alter the segregation isotherm. The value of $g_{V_{\ddot{O}}}$ required to produce these curves varies from 2.17 eV for $N_s = 1/4$ of the oxygen sites to 2.00 eV for $N_s = 1/2$ of the oxygen sites. Therefore, it appears that the saturation number of sites at typical grain boundaries in Gd^{3+} doped ceria ,N_s, is between 1/4 and 1/2 of the oxygen site density and the free energy of formation of an oxygen vacancy, $g_{V_{\ddot{O}}}$, is ≈ 2 eV.

This derived value for the free energy of formation of an oxygen vacancy is reasonable given the previously measured thermodynamic properties of ceria. The total Frenkel energy for ceria has been reported as 4.45 eV [68]. As seen in Figure 2-1 the Frenkel energy is equal to $g_{V_{\ddot{O}}} + g_{O_i''}$ and therefore, $g_{O_i''}$ is ≈ 2.45eV. This is reasonable because

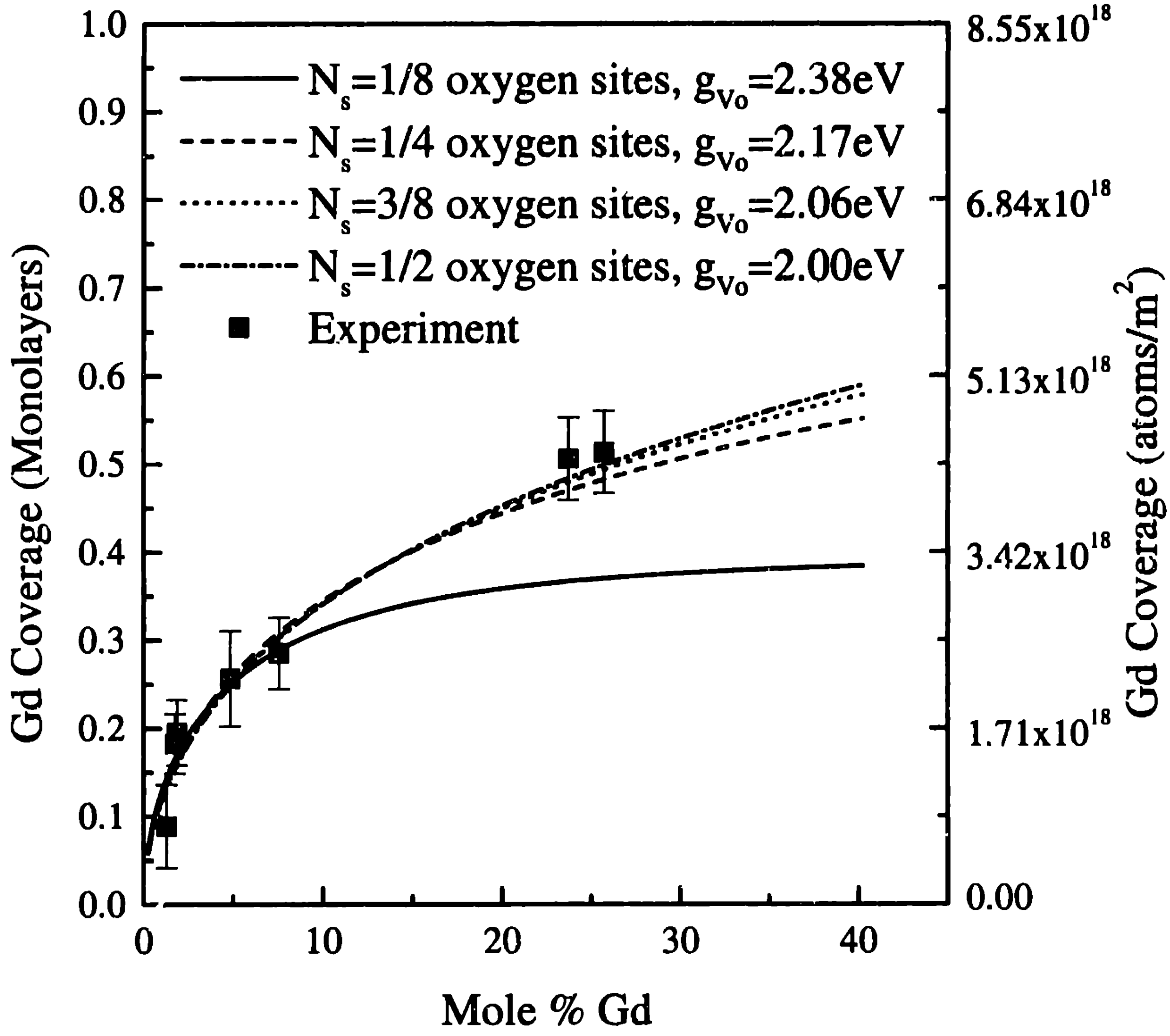

Figure 4-5: Additional fits of the limited-site space charge with varying assumptions of the number of interfacial sites (N_s).

ceria is easily reduced, which implies that the formation of oxygen vacancies is more energetically favored than the formation of oxygen interstitials. Experimental work on undoped nanocrystalline ceria has shown that the heat of reduction of nanocrystalline material is ≈ 2.4eV less than the bulk heat of reduction [86]. Because the interface to volume ratio in nanocrystalline materials is so large, the heat of reduction measured for a nanocrystalline oxide is essentially the heat of reduction of the interface of the crystal. The difference between the nanocrystalline heat of reduction and the heat of reduction for coarse grained materials is therefore the energy required to move an oxygen ion from the bulk to the surface, which is what I have defined as $g_{V_O^{\cdot\cdot}}$. Additionally, Sayle *et al.* have used computer simulation techniques to calculate the energy required to remove an oxygen ion from the bulk of ceria as well as three different surfaces [56]. The difference between removing an O^{2-} ion from the surface and from the bulk is equivalent to $g_{V_O^{\cdot\cdot}}$ as I have defined it. The calculations show that for a (111) surface $g_{V_O^{\cdot\cdot}}$ is 0.39eV, for a (110) surface $g_{V_O^{\cdot\cdot}}$ is 1.5eV, and for a (310) surface $g_{V_O^{\cdot\cdot}}$ is 2.47eV. The experimentally derived value of $g_{V_O^{\cdot\cdot}}$ is reasonable when compared to the theoretical calculations for the (110) and (310) surfaces. The agreement with the calculation for a (111) surface is not particularly good, but given that the value derived in this work was for a general high-angle grain boundary, while the (111) surface is a particular low energy surface in ceria, the discrepancy is not surprising.

The assumption of dilute solution in the bulk of the material is formally violated in the compositions studied in this work. However, the limited-site space charge model can be fit very effectively to the experimental isotherm. If significant defect interactions in the bulk existed which are not accounted for in the space charge model, it is expected that the fit to the data would inaccurately reproduce the segregation isotherm. In addition, the measured segregation is sub-monolayer in nature even at 26 mole % of Gd and therefore the assumptions of the limited-site space charge model seem justified. Specifically, the number of interfacial sites appears to be limited to ≤ 1 monolayer of oxygen, with $g_{V_{\ddot{O}}}$ being composition independent once the configurational entropy of the interface states has been considered.

The Gd^{3+} segregation data can also be fit to a Langmuir adsorption isotherm as seen in Figure 4-6. The Langmuir isotherm bends over at high concentration because the ordinate is the excess of Gd^{3+}, not the interfacial concentration X^{gb}. Equation 2.27 was fit to the experimental data via non-linear least squares fitting. The best fit for a two-parameter model is obtained for a saturation coverage of $X^{sat}_{interface} = 0.99$, and $\Delta G = -0.34$ eV. For comparison, the limited-site space charge model fit and the two parameter Langmuir adsorption model fit are shown in Figure 4-6. From Table 2.2, the estimate of the enthalpy of segregation for a simple ion size misfit theory for Gd^{3+} in ceria is ≤ -0.110 eV. Even though the elastic constants are not known for gadolinia, the error introduced by approximating the elastic properties of gadolinia with those of ceria cannot account for the large discrepancy in the enthalpy of segregation from the best-fit to the experimental data. Elastic misfit does not satisfactorily account for the quantity of Gd grain boundary segregation measured. On the other hand, the best-fit of the Langmuir adsorption isotherm predicts, in a similar manner to space charge theories, a limited number of sites at the interface (≤ 1 monolayer) and a free energy of segregation of a few tenths of an eV. The Langmuir adsorption isotherm does not formally specify the source of the energy difference between interfacial and bulk sites. Other possible non-electrostatic contributions to segregation include the change in interfacial energy upon solute segregation and chemical interactions between the matrix and solute ions.

Figure 4-6 also shows that simple observations of segregation isotherms can not be used to differentiate among the possible driving forces. Both a detailed limited-site

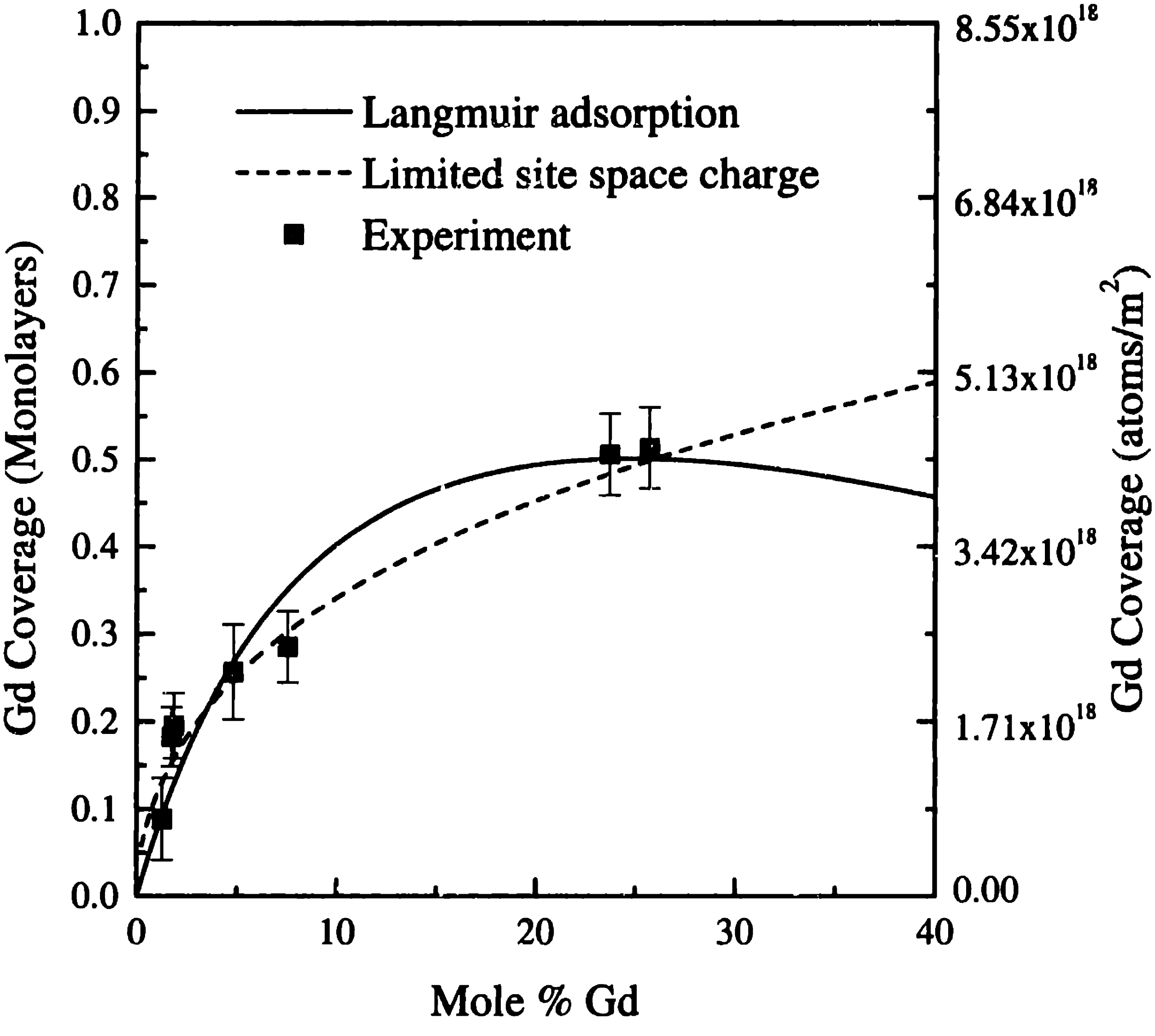

Figure 4-6: Comparison of the limited-site space charge model and the Langmuir adsorption isotherms to the experimental data.

space charge model incorporating extensive defect chemical calculations and an empirical Langmuir adsorption isotherm provide a satisfactory fit to the observed Gd^{3+} grain boundary segregation over a wide concentration range. Both models use a similar statistical mechanical formalism in the description of the free energy of the overall system. Not surprisingly, the resulting segregation isotherms differ only slightly. To date, this fact has not been widely appreciated.

After a careful analysis of the data, we conclude that segregation of Gd^{3+} in ceria is driven predominantly by electrostatic interactions. The experimentally derived isotherm is best fit with a limited-site space charge model over the concentration regime studied. While a Langmuir adsorption isotherm with two adjustable parameters fits the data nearly as well, the best-fit value of ΔG is significantly too high to represent the elastic strain introduced into the lattice by Gd'_{Ce}. Further tests are necessary to conclusively rule out any additional minor driving forces for Gd^{3+} segregation in ceria.

4.2 Ta^{5+} Segregation in Singly Doped Ceria

In order to further test the mode of segregation, samples for which the space charge and Langmuir adsorption models predict opposite segregation results were made. From Equation 2.7, the spatial variation of defect concentration depends on both the sign of the space charge potential and the effective charge of the defect. In the present sign convention, defects which have the same sign as the potential will segregate in the near grain boundary space charge region, while defects with the opposite sign should be depleted. The space charge potential is determined by the bulk defect chemistry. Using the best fit value of $g_{V_O^{\cdot\cdot}}$ from the Gd^{3+} segregation data, ϕ_∞ vs. Ta composition was calculated for 1500°C and air atmosphere using Equations 2.13 and 2.24. The predicted space charge potentials were all <0. Therefore Ta^{5+} is predicted to be depleted near the interfaces. The previously reported observations of no Ta^{5+} segregation in Ce-stabilized Ta doped zirconia by Hwang and Chen [5] are in agreement with this prediction.

Three samples containing between 0.28% and 1.79% Ta were prepared. Segregation measurements were performed at 106 grain boundaries. According to the space charge models all three Ta^{5+} doped samples should have exhibited $\leq$ 0.01 monolayer of Ta^{5+} depletion near the grain boundaries. On the other hand, significant Langmuir adsorption of Ta^{5+} is expected due to the large ion size misfit of $Ta_{Ce}^{\cdot}$ (see Table 2.2).

In fact, all grain boundaries measured in these materials exhibited a net excess of Ta^{5+} near the grain boundaries. Figure 4-7 shows the results of a linescan across a boundary in Ta3. The segregation apparently exists within 5 nm of the boundary validating the area-scan method for Ta^{5+} segregation in ceria. Figure 4-8 shows the measured Ta^{5+} excess at 10 boundaries in sample Ta1. The error bars are from the error analysis of Section 3.3 and represent a 95% confidence limit. The measurements of Γ_{Ta} were very precise due to the large number of counts collected for each spectrum. Figure 4-9 shows the measured Ta^{5+} segregation isotherm. This observation was unexpected and in direct opposition to the prediction of the space charge model and previous observations in Ce-stabilized Ta-doped zirconia [5]. An electrostatic driving force is unambiguously *not* the predominant one for Ta^{5+} in ceria. These results do not mean that a space charge is absent in Ta^{5+} doped ceria, but it is certainly not the predominant effect. The best fits of both a one-parameter and a two-parameter Langmuir adsorption isotherm are shown in Figure 4-9. The one-parameter model does not fit the data as well as the two-parameter fit. Using the one-parameter Langmuir model, the best-fit value is $\Delta G = -0.58$ eV. For the two-parameter Langmuir model, the best-fit is $X_{interface}^{sat} = 0.6$ and $\Delta G = -0.72$ eV. The calculated value of strain misfit energy for Ta^{5+} in ceria using the theoretical

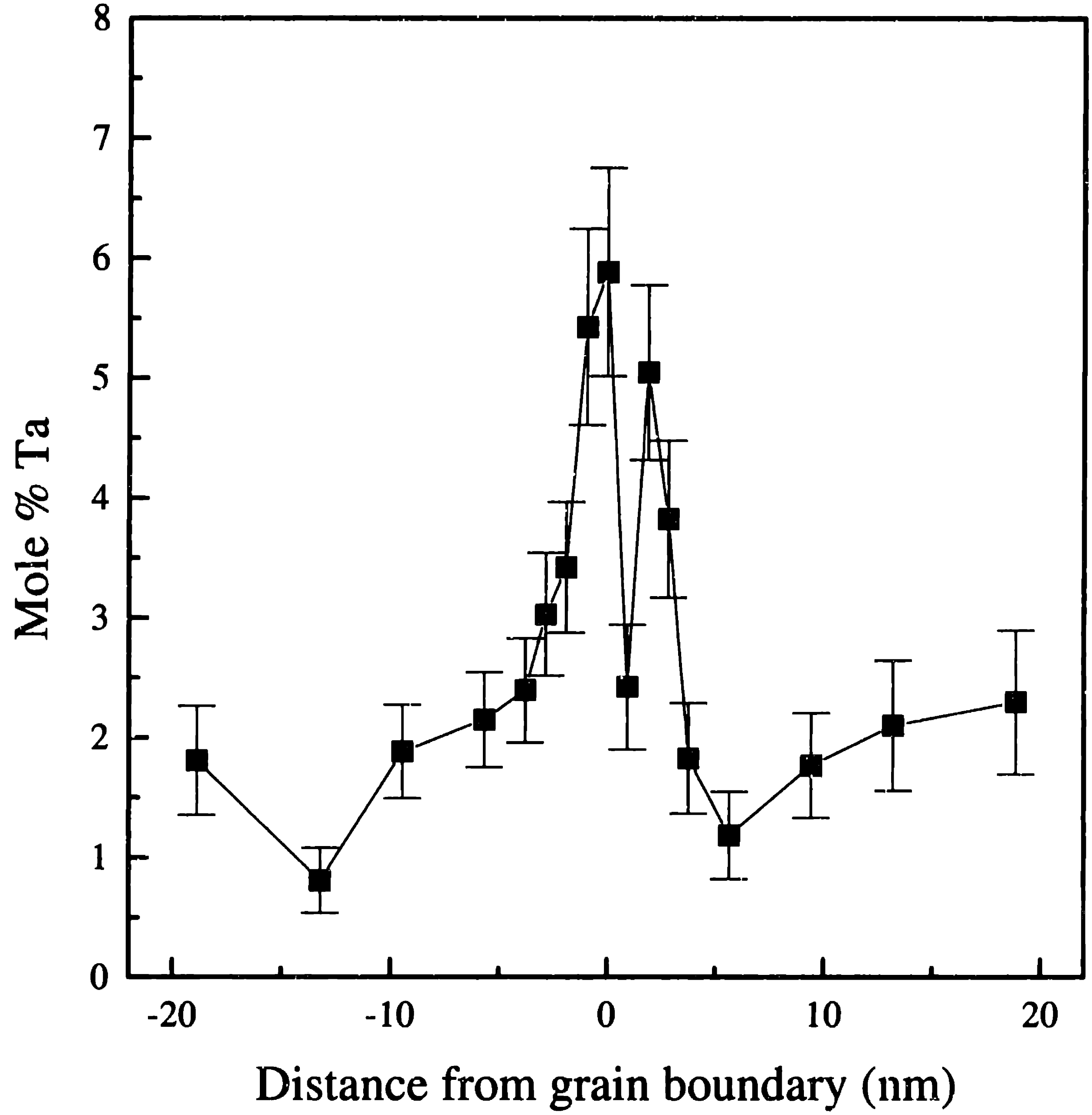

Figure 4-7: X-ray linescan across a grain boundary in sample Ta3. Ta^{5+} segregation exists within ±5 nm of the boundary.

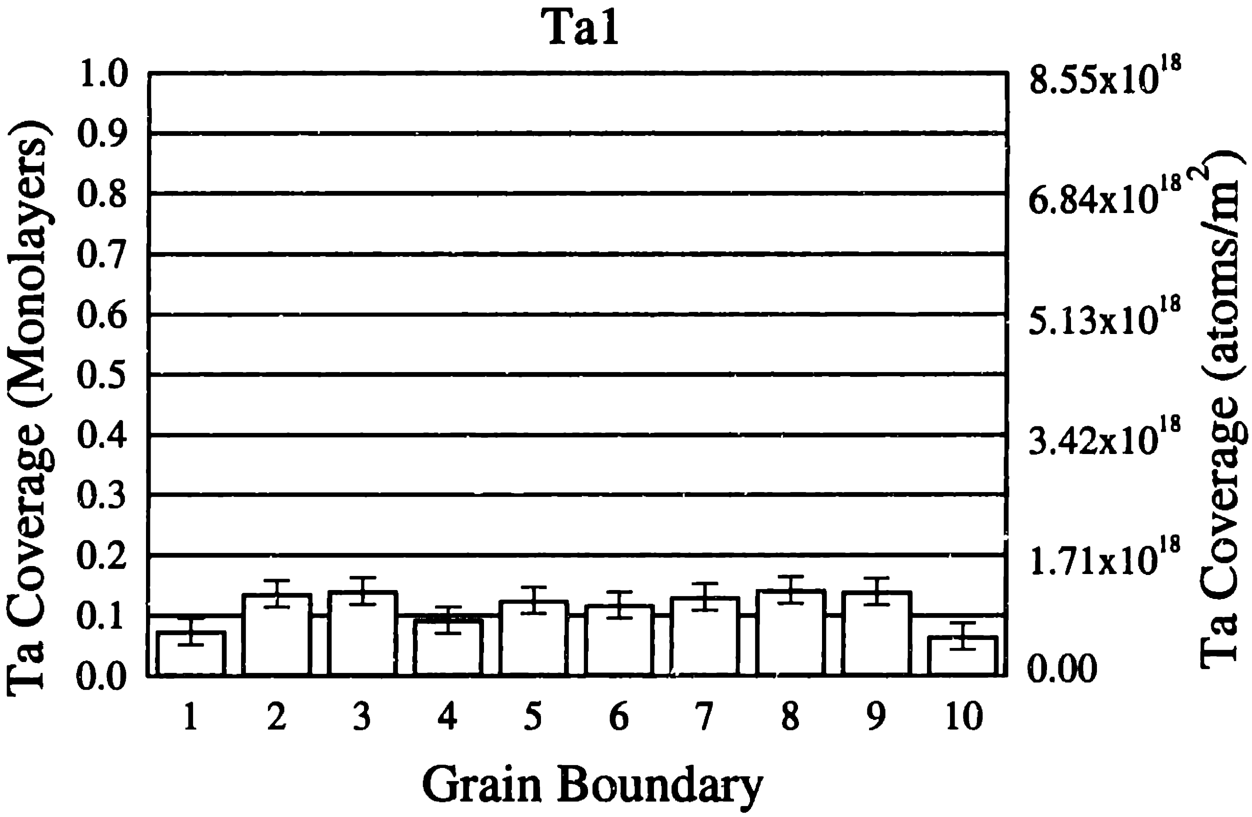

Figure 4-8: Grain boundary segregation at 10 different boundaries in Ta1. Error bars are derived from counting statistics error.

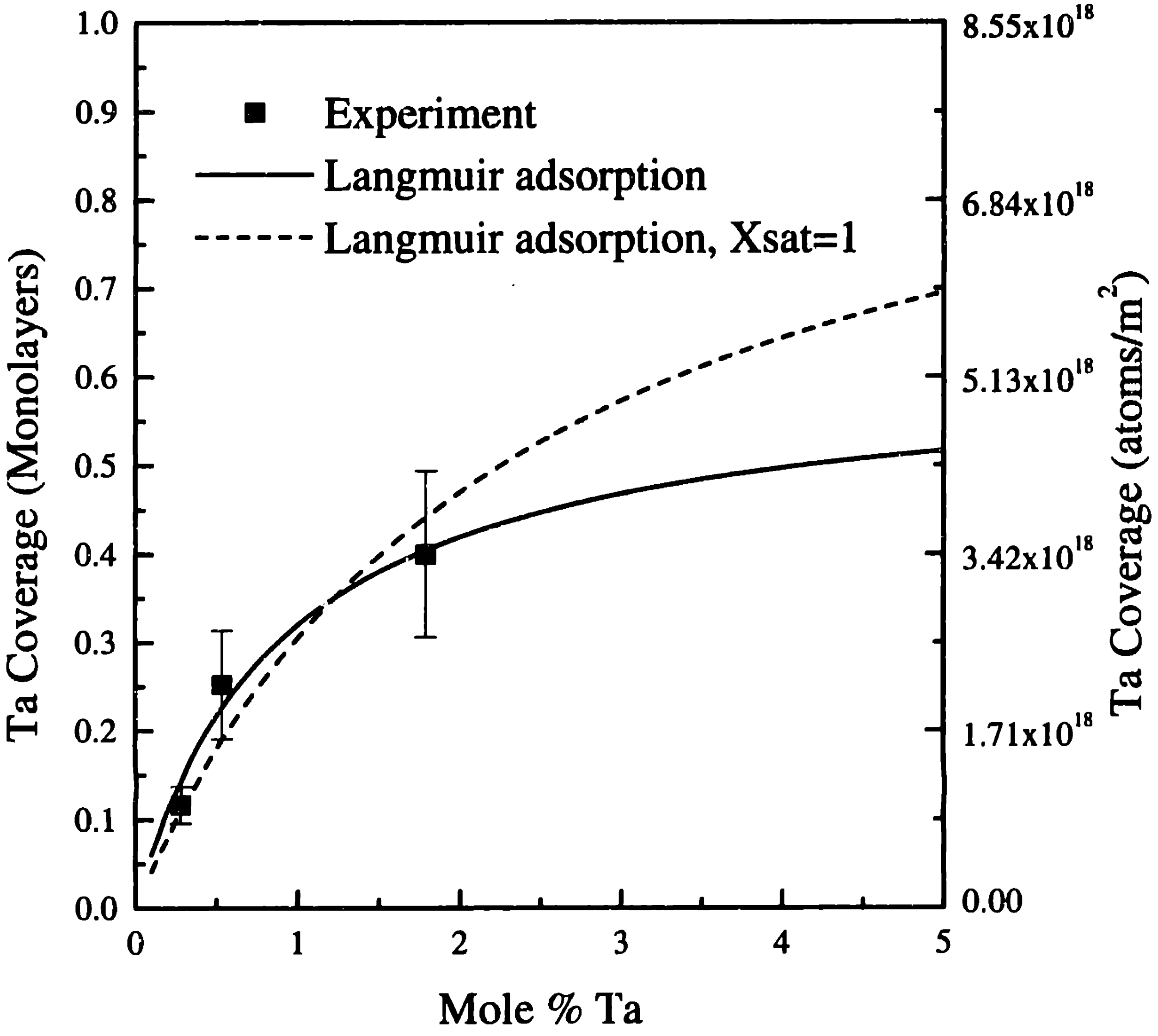

Figure 4-9: Measured Ta^{5+} segregation isotherm and Langmuir adsorption fit.

elastic constant derived by Hill and Catlow [78] was -0.757 eV. This assumes complete relaxation of the elastic strain upon segregation. It can be concluded that elastic ion size misfit effects can satisfactorily explain Ta^{5+} segregation in ceria.

Previously, Hwang and Chen [5] reported that the segregation of various dopants in Ce-stabilized tetragonal zirconia depended on the relative charge of the dopant ion. Negatively charged acceptor dopants such as Mg''_{Zr}, Sc'_{Zr}, In'_{Zr}, and Y'_{Zr} were observed to segregate as measured by XPS and AES on intergranular fracture surfaces of polycrystalline materials. No segregation of positively charged donors $Nb^{\bullet}_{Zr}$ and $Ta^{\bullet}_{Zr}$ was measured. Hwang and Chen used a space charge model to explain the charge dependence of the segregation. While Hwang and Chen's [5] results for Ce-stabilized tetragonal zirconia are certainly suggestive of an electrostatic component to segregation of pentavalent dopants in zirconia, there are a number of difficulties in extending their observations to ceria. The role of Si in their samples is not well characterized. The XPS results showed no Si at the boundaries, yet their own STEM observations of Ca^{2+} doped Ce-stabilized zirconia showed the existence of a 1 nm thick silicate film at the boundaries. Either the Si content of the interfaces was below the detection limit of XPS or the fracturing of the samples destroyed the silicate films and possibly the uppermost atomic layers of the samples. The slow cooling of their samples allowed for non-equilibrium segregation and dopant redistribution. The ill defined temperature and therefore oxidation state of the multivalent $Ce^{3+/4+}$ stabilizer makes any defect chemical modeling extremely difficult. In addition, the defect chemistry of Ce-stabilized zirconia is not well characterized in general.

4.3 Grain Boundary Segregation in co-doped Ceria

STEM measurements of Gd^{3+} and Ta^{5+} grain boundary segregation were performed on 96 different grain boundaries in 4 different co-doped compositions. Figure 4-10 shows a line scan across a boundary in CGT4. Segregation of both Gd^{3+} and Ta^{5+} is observed within ±5nm of the boundary. Figure 4-11 shows the excess of Gd^{3+} and Ta^{5+} measured at 19 separate boundaries in sample CGT1. Equation 3.1 was used to obtain the integrated excess of Gd^{3+} and Ta^{5+} at each particular boundary from the X-ray data. The excess in terms of atoms per square meter was converted into equivalent monolayers by dividing by the average cation site density in ceria ($N^{2/3} = 8.55 \times 10^{18}$ atoms/m^2). The error bars come from the error analysis described in Section 3.3. As can be seen from Figure 4-11, the precision of the measurement of Γ_{Gd} and Γ_{Ta} is quite high. By rastering over a well-defined volume, the statistical precision of the composition measurement is enhanced at the expense of spatial information. The average Gd^{3+} excess in sample CGT1 is 0.12 monolayers (1.03×10^{18} atoms/m^2). The average Ta^{5+} excess is 0.15 monolayers (1.28×10^{18} atoms/m^2). The excesses of Gd^{3+} and Ta^{5+} for a single composition, temperature and oxygen partial varied somewhat from grain boundary to grain boundary. This is reasonable since the details of grain boundary structure will affect the energetics of grain boundary sites [73].

4.3.1 Gd^{3+} Segregation in co-doped Ceria

Figure 4-12 shows the average Gd^{3+} excess found in each of the four compositions studied here. Sub-monolayer segregation is observed for all samples. We have plotted Gd^{3+} coverage (Γ_{Gd}) versus net mole percent Gd. Net mole percent Gd is defined as %Gd - %Ta. The error bars represent the 95% confidence limits for the measurements of excess

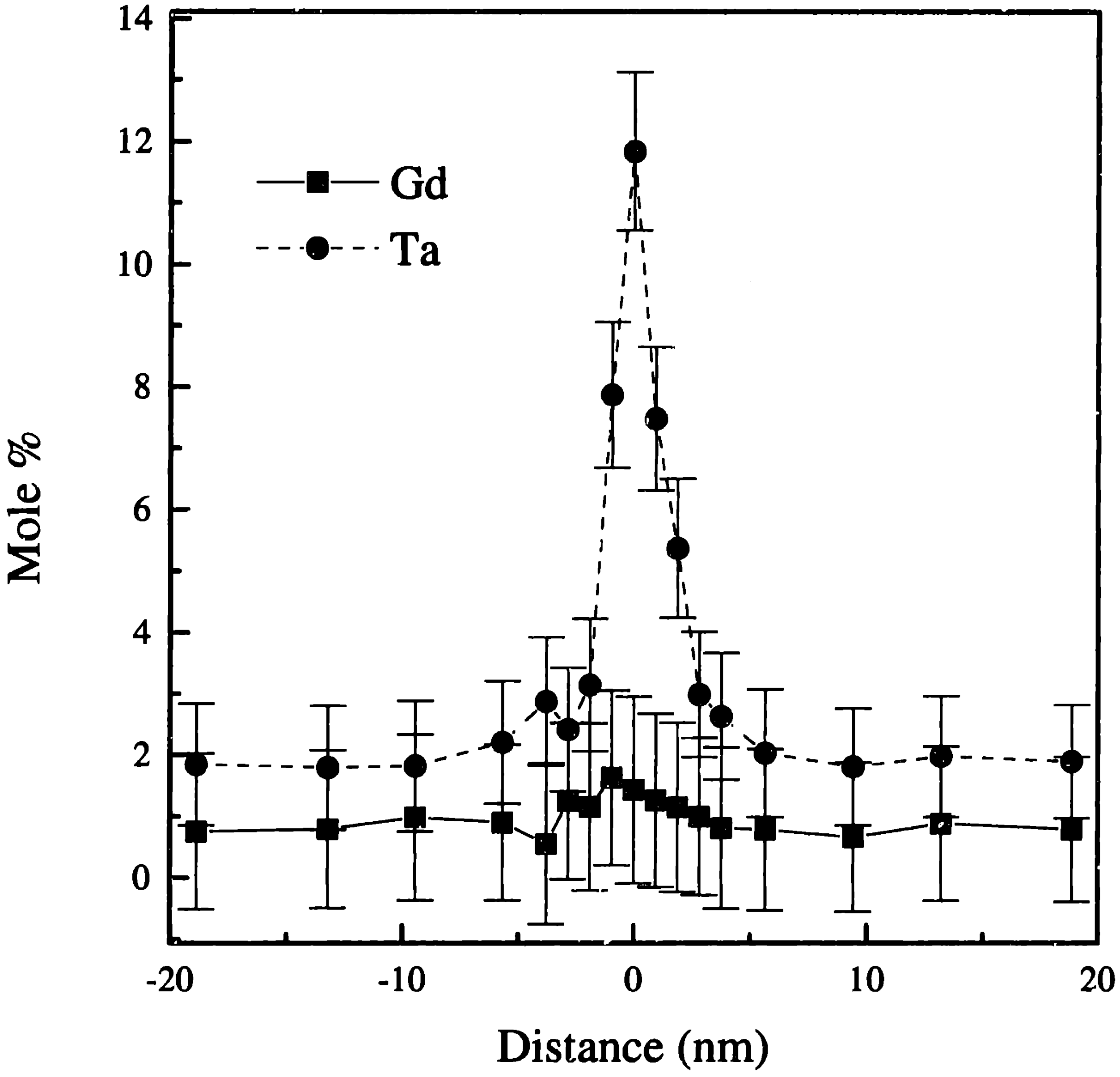

Figure 4-10: X-ray linescan across a grain boundary in sample CGT4. Gd^{3+} and Ta^{5+} segregation exists within ±5 nm of the boundary.

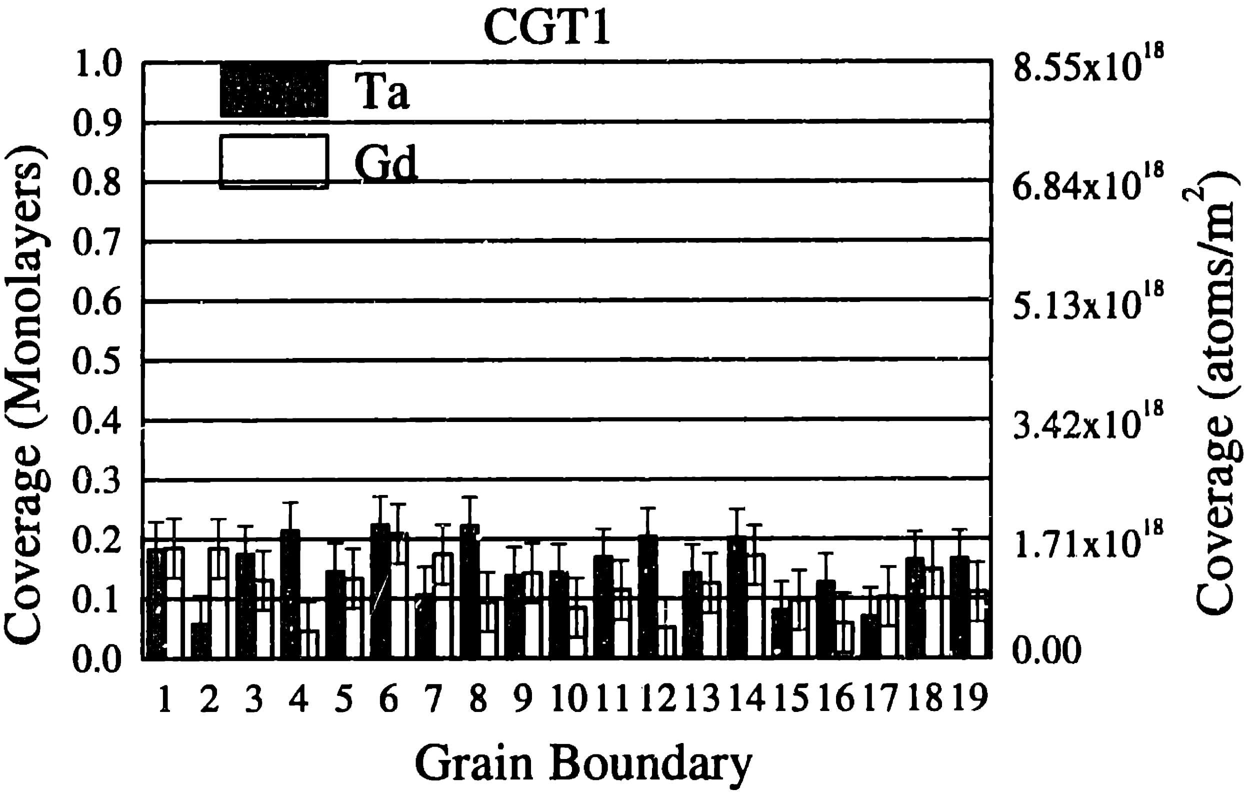

Figure 4-11: Gd^{3+} and Ta^{5+} coverage in co-doped ceria.

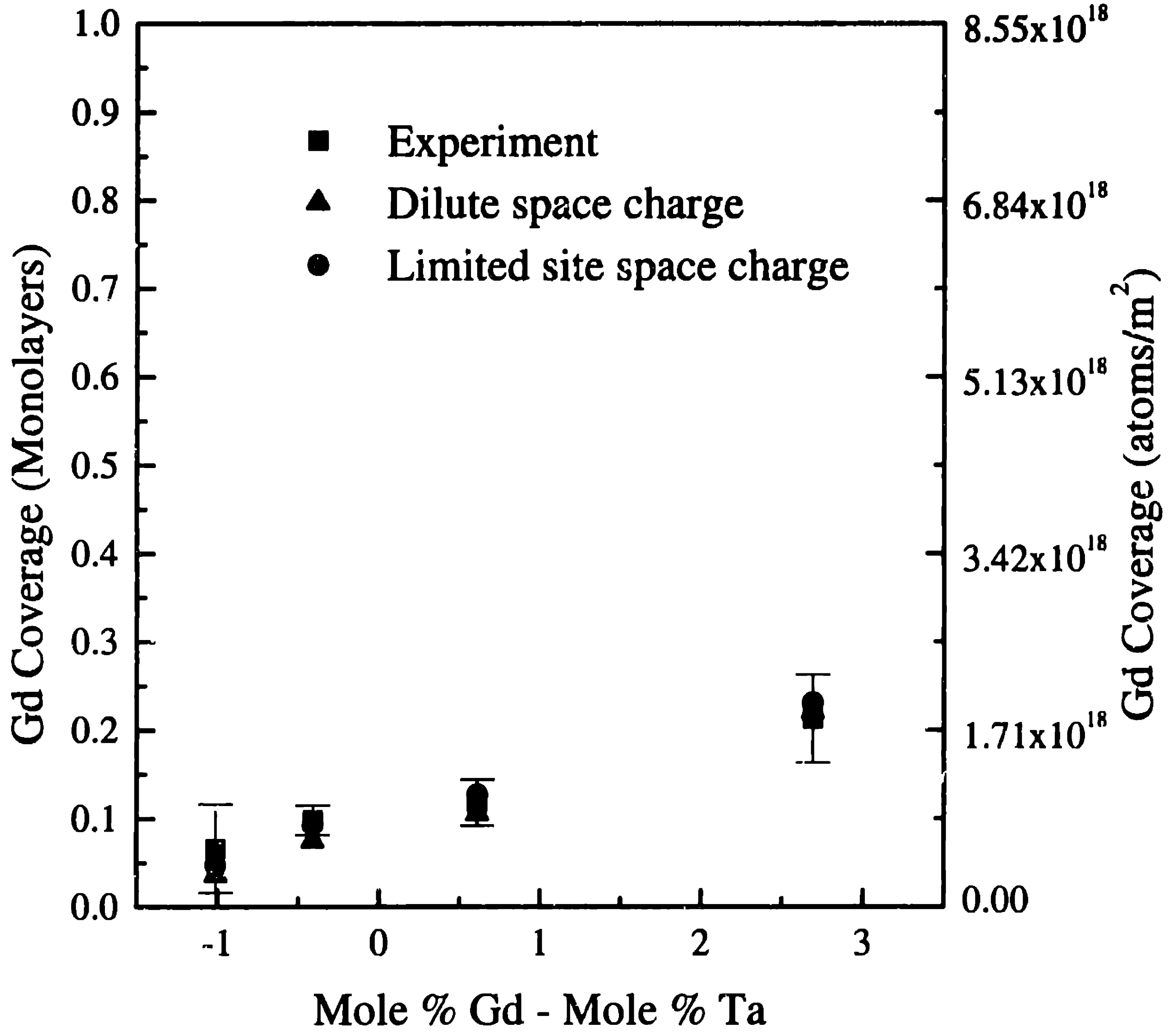

Figure 4-12: Gd^{3+} coverage in co-doped ceria. Comparison between space charge models and experiment.

Table 4.1: Model input parameters

Parameter	Description	Model	Value
$g_{V_{\ddot{O}}}$	Free energy of formation of an oxygen vacancy	Space charge	2eV
N_s	Areal density of available interfacial sites	Limited-site space charge	6.78×10^{18} atoms/m^2
ΔG^{o}_{Gd}	Free energy of adsorption for Gd^{3+}	Adsorption	-0.34 eV
X^{sat}_{Gd}	Saturation amount of Gd^{3+}	Adsorption	0.99
ΔG^{o}_{Ta}	Free energy of adsorption for Ta^{5+}	Adsorption	-0.72eV
X^{sat}_{Ta}	Saturation amount of Ta^{5+}	Adsorption	0.6

Gd^{3+} and correspond to the variability from boundary to boundary. For comparison, the predictions of the two space charge models are also plotted in Figure 4-12 using the best-fit results from Gd^{3+} doped ceria. Table 4.1 details the various parameters derived previously and applied to these data. The space charge models accurately reproduce the experimental data within the error of the measurements. Explicit co-segregation effects between Gd^{3+} and Ta^{5+} are not part of the space charge models and are concluded to be unnecessary to explain the level of Gd^{3+} segregation in these co-doped ceria samples within the framework of a space charge model.

Figure 4-13 plots the same experimental data against the total Gd^{3+} content. The results of a Langmuir model originally fit to the segregation of Gd^{3+} in ceria are also plotted. The free energy of segregation for the model is -0.34eV (See Table 4.1) and again reproduces the experimental isotherm well. No co-segregation effects are included in the simple Langmuir model. The Gd^{3+} and Ta^{5+} ions are assumed to be non-interacting. This model fits the experimental data reasonably well.

Applying the model of Guttmann and McLean discussed in Section 2.3 to co-doped

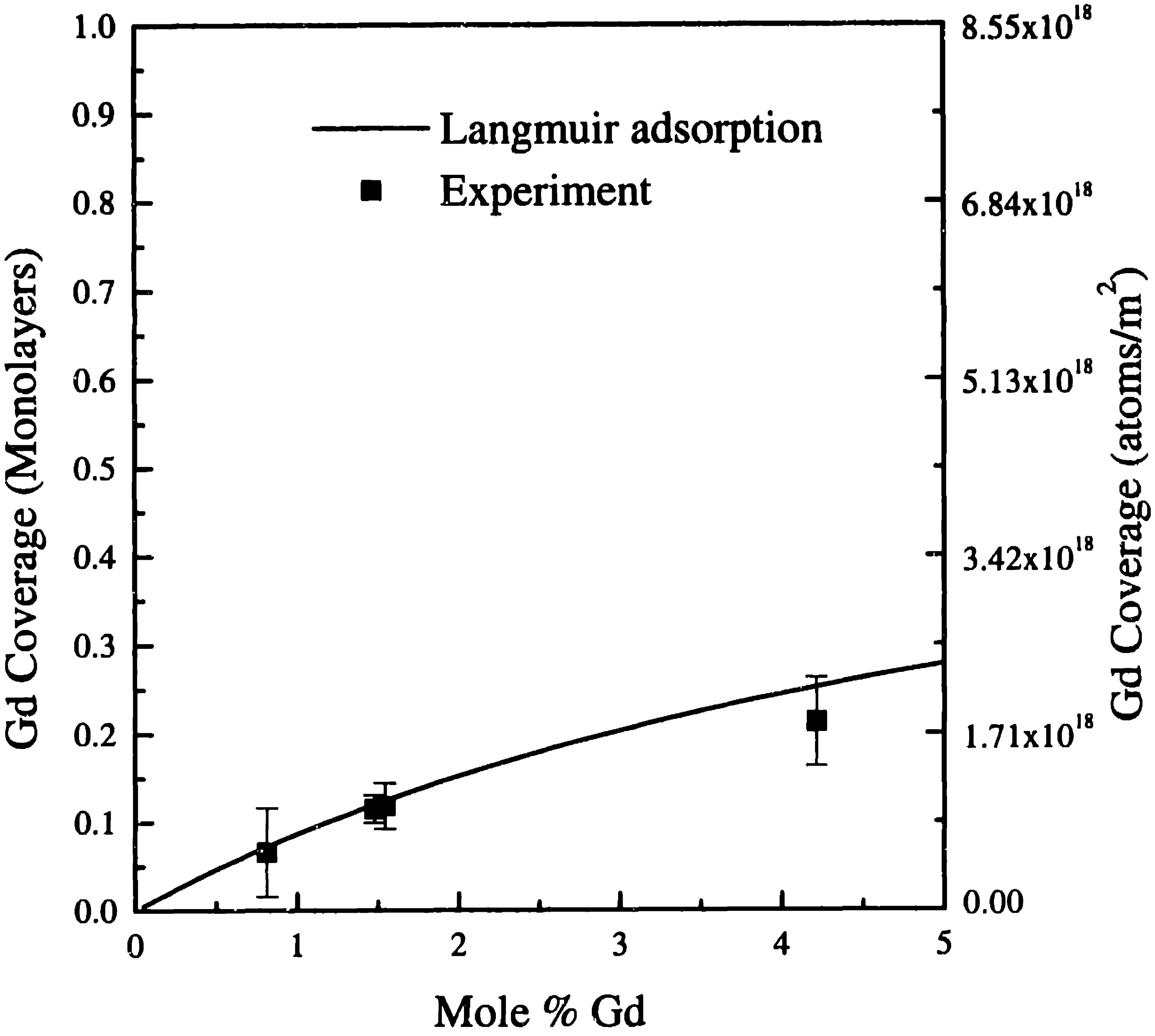

Figure 4-13: Gd^{3+} coverage in co-doped ceria. Comparison between Langmuir adsorption model originally fit to segregation data in Gd^{3+} doped ceria and experimental observations of Gd^{3+} segregation in co-doped ceria.

ceria, we can address the effects of interactions between Gd^{3+} and Ta^{5+} ions. Figure 4-14 plots the Gd^{3+} coverage versus mole percent Gd along with the results of the Guttmann/McLean model. The parameters required for the Guttmann/McLean model are: the solute saturation limit at the interface X_i^{sat}, the free energy of segregation of the solutes in a binary solid solution ΔG_i^o, and the interaction energy α between the different solutes. For the results plotted in Figure 4-14, we used the best-fit values from our previous studies of Gd^{3+} and Ta^{5+} doped ceria listed in Table 4.1, along with the coulombic attraction between Gd'_{Ce} and $T'a_{\dot{C}e}$ defects sitting on nearest neighbor cation sites. This ternary adsorption model is a poor fit to the experimental data, confirming that Gd^{3+} segregation in ceria is electrostatic in nature. The adsorption model consistently predicts less Gd^{3+} segregation than is observed. Even when the interaction parameter α is set to zero, which implies no preferential co-segregation effect between Gd^{3+} and Ta^{5+}, site competition is predicted to limit the segregation of Gd^{3+} to values well below those experimentally observed. This is because the strong adsorption of Ta^{5+} should preferentially fill the available interfacial sites with Ta^{5+} at the expense of Gd^{3+}.

Gd^{3+} segregation in ceria co-doped with Gd^{3+} and Ta^{5+} can be effectively modeled only by the space charge models. The ternary adsorption model developed by Guttmann and McLean predicts that in a ternary solid solution, the solute with the larger segregation energy (*e.g.* Ta^{5+} in ceria) will preferentially adsorb at the limited number of interfacial sites. Accordingly, the more weakly adsorbing solute (Gd^{3+} in this case) is predicted to segregate to a lesser extent than it would in a binary solid solution. For ceria co-doped with Gd^{3+} and Ta^{5+}, neither of these predictions is observed. Gd^{3+} segregation in ceria is therefore a strictly electrostatic phenomenon which can be described over a wide defect chemistry range by a limited-site space charge model.

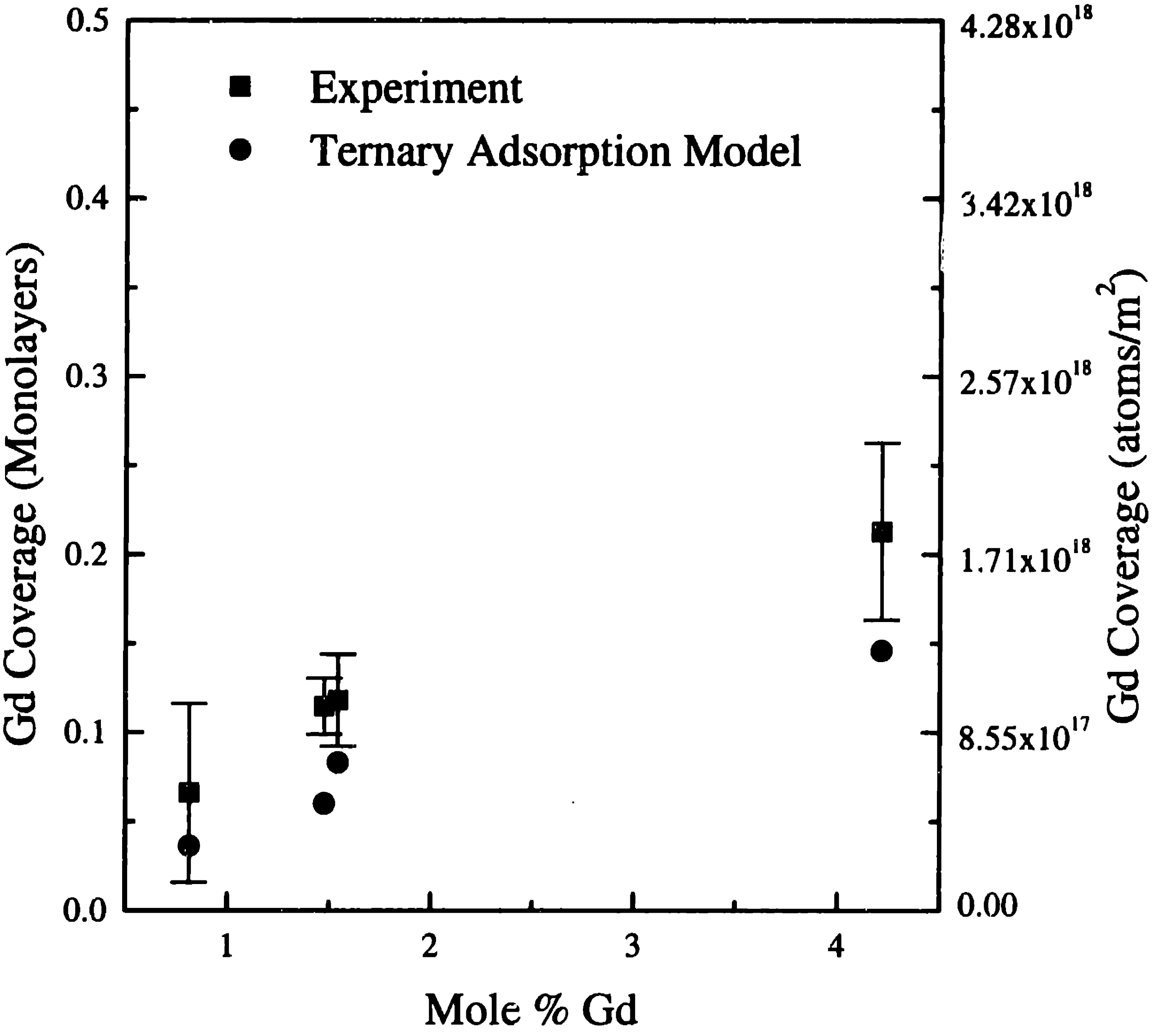

Figure 4-14: Gd^{3+} coverage in co-doped ceria. Comparison between Guttmann/McLean model and experiment.

4.3.2 Ta^{5+} Segregation in co-doped Ceria

Figure 4-15 shows the segregation results for Ta^{5+} in the co-doped compositions studied here. The error bars are 95% confidence limits and represent the boundary to boundary variation. Sub-monolayer segregation is observed. From our previous studies of Ta^{5+} segregation in ceria, we have concluded that Ta^{5+} segregation is primarily an adsorption phenomenon. These co-doped compositions allow us to study the co-segregation effects between $Ta_{Ce}^{\cdot}$ and Gd_{Ce}' as well as whether a minority space charge segregation effect acts on Ta^{5+} in ceria. The Langmuir adsorption isotherm which was a best-fit to the Ta^{5+} segregation data in ceria is shown for reference. If Ta^{5+} segregation in ceria is strictly an adsorption phenomenon with no co-segregation or minority driving forces, the Ta^{5+} segregation in the co-doped compositions should fall on the Ta^{5+} segregation isotherm for ceria doped only with Ta^{5+}. Ta^{5+} segregation in co-doped ceria is significantly less, for a given quantity of Ta^{5+} in the bulk, than observed in binary solutions of Ta^{5+} in ceria. The existence of minority driving forces and/or co-segregation effects for Ta^{5+} segregation in ceria is confirmed.

Figure 4-16 shows the result of the Guttmann/McLean model for Ta^{5+} segregation in co-doped ceria. This ternary adsorption model does not accurately predict the observed Ta^{5+} segregation in co-doped ceria. Specifically, the adsorption model predicts a larger Ta^{5+} segregation than observed for three of the four compositions. In fact, the ternary adsorption model predicts that Ta^{5+} should segregate more strongly in co-doped samples than in singly doped specimens. The opposite is observed; the addition of Gd^{3+} into ceria depresses the quantity of Ta^{5+} segregation. Even in samples with more Ta^{5+} than Gd^{3+} in the bulk, the Ta^{5+} segregation is depressed. The Guttmann/McLean model already accounts for site competition, therefore these results show that there is a negative energetic interaction between $Ta_{Ce}^{\cdot}$ and Gd_{Ce}'.

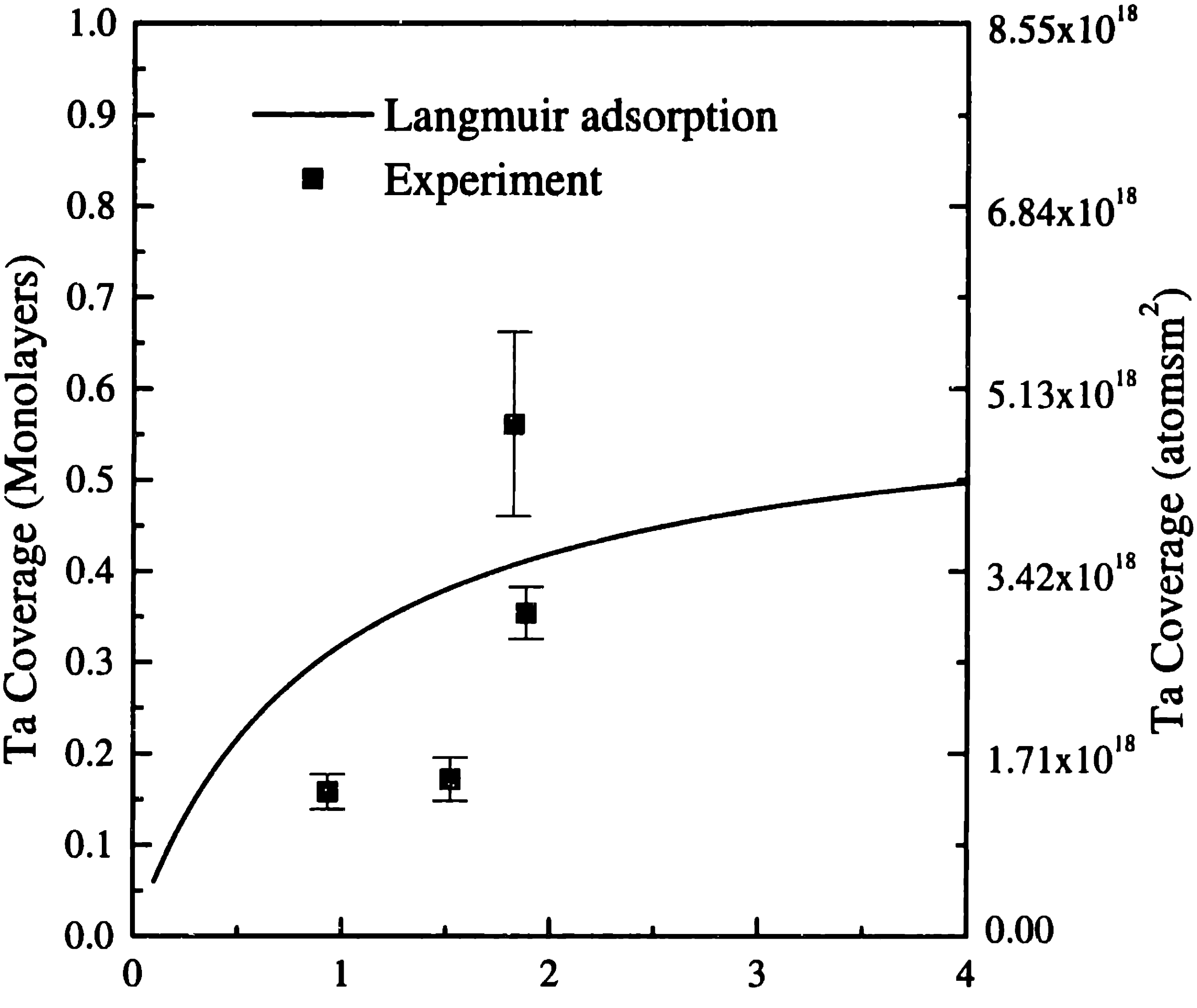

Figure 4-15: Ta^{5+} coverage in co-doped ceria. Comparison between two parameter Langmuir model and experiment.

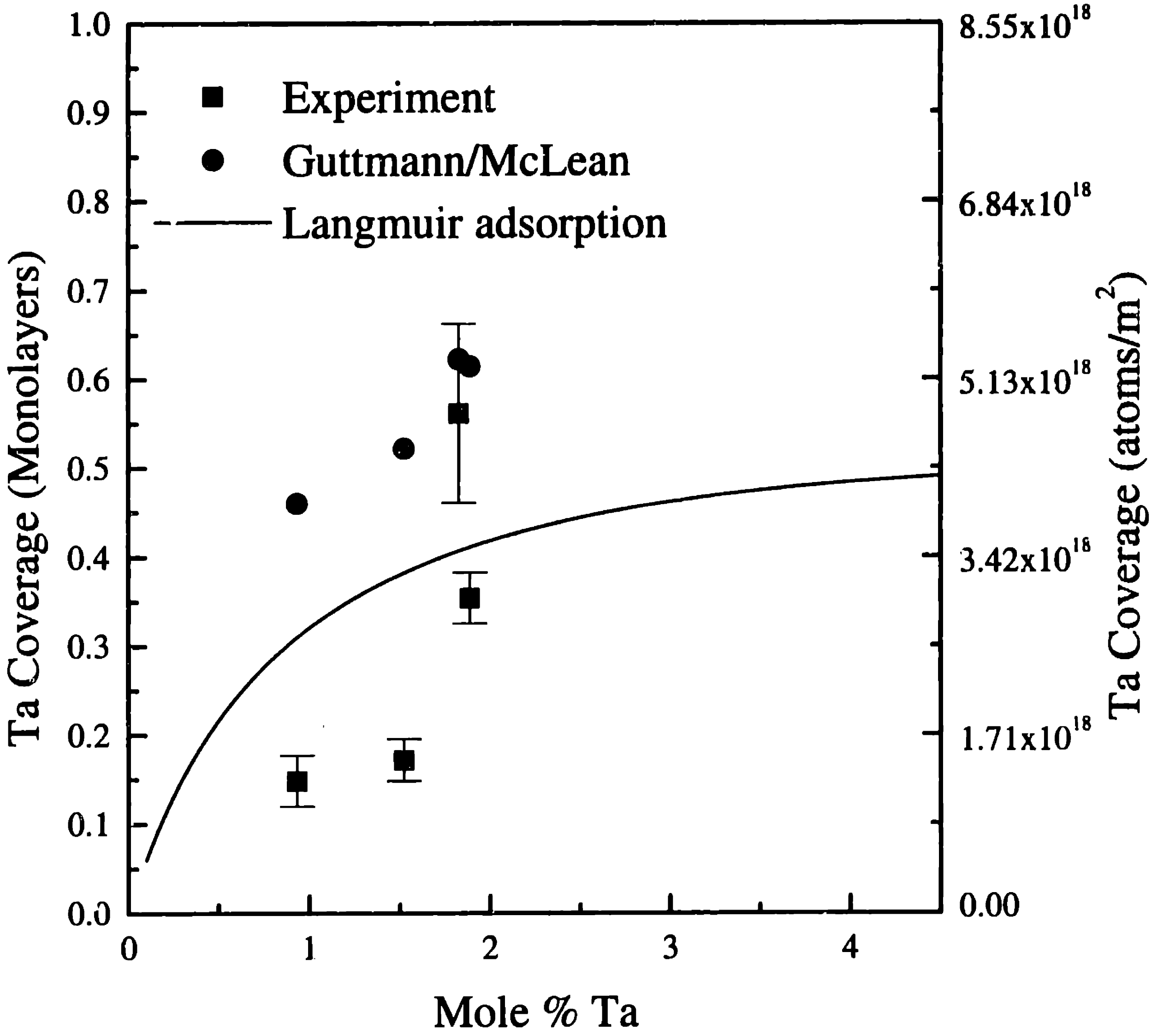

Figure 4-16: Ta^{5+} coverage in co-doped ceria. Comparison of experimental observations with the Guttmann/McLean model discussed in Section 2.3 and the best-fit Langmuir isotherm.

One possible explanation of less Ta^{5+} segregation in co-doped samples than in singly doped samples is the influence of the space charge. From the Gd^{3+} segregation data, the existence of a near interfacial space charge in ceria has been confirmed. Even though Ta^{5+} segregation is predominantly adsorption, the existence of a minority effect has not been ruled out. The space charge models predict that Ta^{5+} depletion in will increase in Ta^{5+} rich compositions and decrease in Gd^{3+} rich compositions. The excess depletion predicted is on the order of 1/1000 of a monolayer, an amount much too small to be experimentally confirmed. The observed depression of Ta^{5+} segregation in co-doped samples is on the order of 1/10 of a monolayer, which is much too large to be due to a simple excess depletion of Ta^{5+} in the space charge. It is therefore concluded that there exists a strong negative co-segregation effect of Gd^{3+} on Ta^{5+} is observed in co-doped ceria.

4.4 Grain Boundary Morphology in Doped Ceria

Further support of the above interpretation of the segregation results is seen in the HREM observations of grain boundary morphology in ceria. HREM observations of grain boundary morphology coupled with STEM provides a very detailed picture of the chemistry-structure relation for a particular grain boundary. The grain boundary morphology of Ta^{5+} doped ceria was markedly different than the morphology of grain boundaries in Gd^{3+} doped ceria. Ta^{5+} doped ceria contained amorphous siliceous films while Gd^{3+} doped ceria did not. This is consistent with Ta^{5+} adsorption at the interfacial core modifying the grain boundary sufficiently that an amorphous silicate glass has a lower energy than the grain boundary. Gd^{3+} segegration in a near interface space charge layer does not appear to greatly modify the grain boundary energy and therefore a glassy film is of higher energy than the crystal/crystal interface.

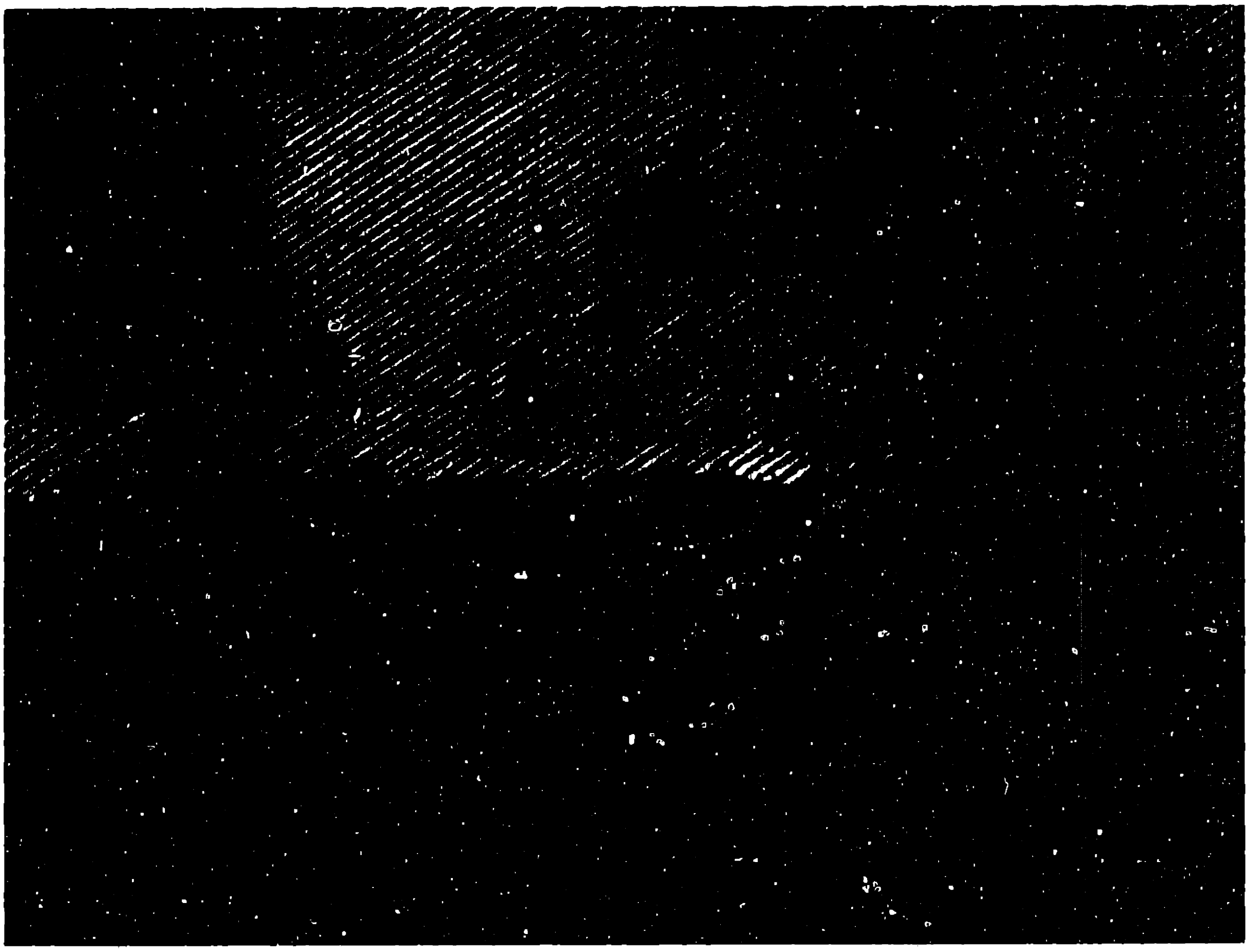

Figure 4-17: High resolution electron micrograph of a grain boundary in Gd7 illustrating the absence of an amorphous film.

4.4.1 Gd^{3+} Doped Ceria

Observations of grain boundary morphology in Gd^{3+} doped ceria were performed using a High Resolution Electron Microscope (HREM) (Akashi TopCon 002B, Paramus, NJ). A total of 20 boundaries in Gd5 and Gd7 were imaged. Figure 4-17 is such a grain boundary. No second phases or amorphous films were seen in these Gd^{3+} doped samples. Si contamination in these samples was 0.8 mole percent from the ICP analyses (see Table 3.2). The absence of second phases or films suggests that the Si was dissolved into the bulk of the ceria. The Si coverage was not quantifiable because the Si content in the bulk of the grains was below the detection limit of the X-ray analyzer. Cosegregation effects between Gd^{3+} and Si are possible, although the Si content of the various Gd samples were not all uniform. It is to be expected that if cosegregation plays an important role, the Gd^{3+} segregation should depend on the Si content of the material. Because the Gd^{3+} isotherm can be so accurately fit by the limited-site space charge and Langmuir adsorption models, which ignore any possible cosegregation, cosegregation effects with Si are concluded to be minor for Gd^{3+} in ceria.

The requirement of the two grains each having a zone axis parallel to the electron beam for lattice fringes to be observable in both grains may cause HREM images to be atypical in terms of chemistry. STEM analysis of the imaged boundaries yielded segregation measurements consistent with those previously measured on non-imaged boundaries for both compositions. The imaged boundaries are therefore representative of a typical high-angle general grain boundary in Gd^{3+} doped ceria.

Figure 4-18: High resolution electron micrograph of a grain boundary in Ta1 at which an amorphous film exists

Figure 4-19: High resolution electron micrograph of a grain boundary in Ta3 at which an amorphous film exists

4.4.2 Ta^{5+} Doped Ceria

HREM observations in two of the Ta^{5+} doped ceria samples significantly showed the existence of amorphous films at some grain boundaries and at grain triple junctions. HREM and STEM measurements of Ta1 were made, and showed Ta^{5+} segregation similar to the average for the sample and glassy films between 0.5 and 1.33 nm thick. Figure 4-18, from Ta1, shows a film $\approx$ 0.5 nm thick. Figure 4-19, from Ta3, shows a film $\approx$ 2.5 nm thick. STEM measurements of this boundary show 0.42 monolayers of Ta^{5+} segregation, which is the average value in this sample. Additional amorphous films were imaged in Ta3 and ranged in thickness between 1.3 and 2.5 nm. The Ta^{5+} excess associated with these films was typical for the sample and did not scale with the film thickness. Additionally, two grain boundaries were imaged in Ta3 with no discernible amorphous film. The Ta^{5+} coverage at these boundaries was $\approx$ 0.5 monolayers. Therefore, Ta^{5+} adsorption is occurring in Ta^{5+} doped ceria in the absence of an amorphous grain boundary film. The composition of these very thin films is difficult to measure quantitatively due to electron beam broadening effects.

The characteristic X-ray lines of Ta^{5+} and Si overlap such that no EDX measurement of Si is possible in Ta containing material. However, Scanning Auger Electron Spectrometry (SAES) (Physical Electronics Model 660, Eden Prairie, MN) measurements on an intergranular fracture surface of Ta3 showed the presence of Si at the surface, which disappeared after sputtering with Ar ions for 30 seconds. The amorphous films observed by HREM are therefore concluded to be a silicate glass with an unknown quantity of dissolved Ce^{4+}, and Ta^{5+}. The typical grain boundary morphology of Ta^{5+} doped ceria includes a siliceous amorphous film between the ceria grains.

4.4.3 co-doped Ceria

Sample CGT4 was observed with HREM. 10 separate boundaries in this Ta^{5+} rich sample were imaged and all were found to contain widely varying amounts of amorphous glass. This wide variation in film thickness, along with the observed 0 dihedral angle leads to the conclusion that these amorphous film are not equilibrium thickness films. The glass thickness is instead constrained by the available Si content and sphering pressure of the sample as discussed in Chiang *et al.* [87].

X-ray linescans were performed on three interfaces in order to investigate the location of the Ta^{5+} and Gd^{3+}. Figure 4-21 shows a "grain boundary" with a thick amorphous film 7.8nm wide. Figure 4-20 shows the X-ray linescan results from this boundary. The focussed electron probe was stepped across the two grains and the amorphous film at 1 nm intervals starting at the left hand crystal/glass interface. The resulting data is a convolution of the electron probe shape and the concentration profiles. As previously mentioned, the Si K_α X-ray line and the Ta M lines overlap at 1.74 keV. The curve denoted as Si assigns all the counts at 1.74 keV to Si. The high apparent concentration of Si in the grains is an artifact of this assignment. The error bars are $\pm 2\sigma$ values for the apparent concentrations. The Ta^{5+} profile clearly shows that the Ta^{5+} ions are segregated into the glassy layer. Electron beam broadening cannot account for the constant Ta^{5+} composition across the width of this film. The counting statistics for Gd^{3+} using the point probe are too poor to allow for confident analysis of the distribution of Gd^{3+} across the film.

The area-scan method was also used to measure the Ta^{5+} and Gd^{3+} excess at this boundary and yielded 1.76 monolayers of Ta^{5+} and 0.06 monolayers of Gd^{3+}. The average coverages for this sample are 0.56 monolayers of Ta^{5+} and 0.07 monolayers of Gd^{3+}. The Ta^{5+} content of the amorphous phase accounts for approximately 1/2 of the measured

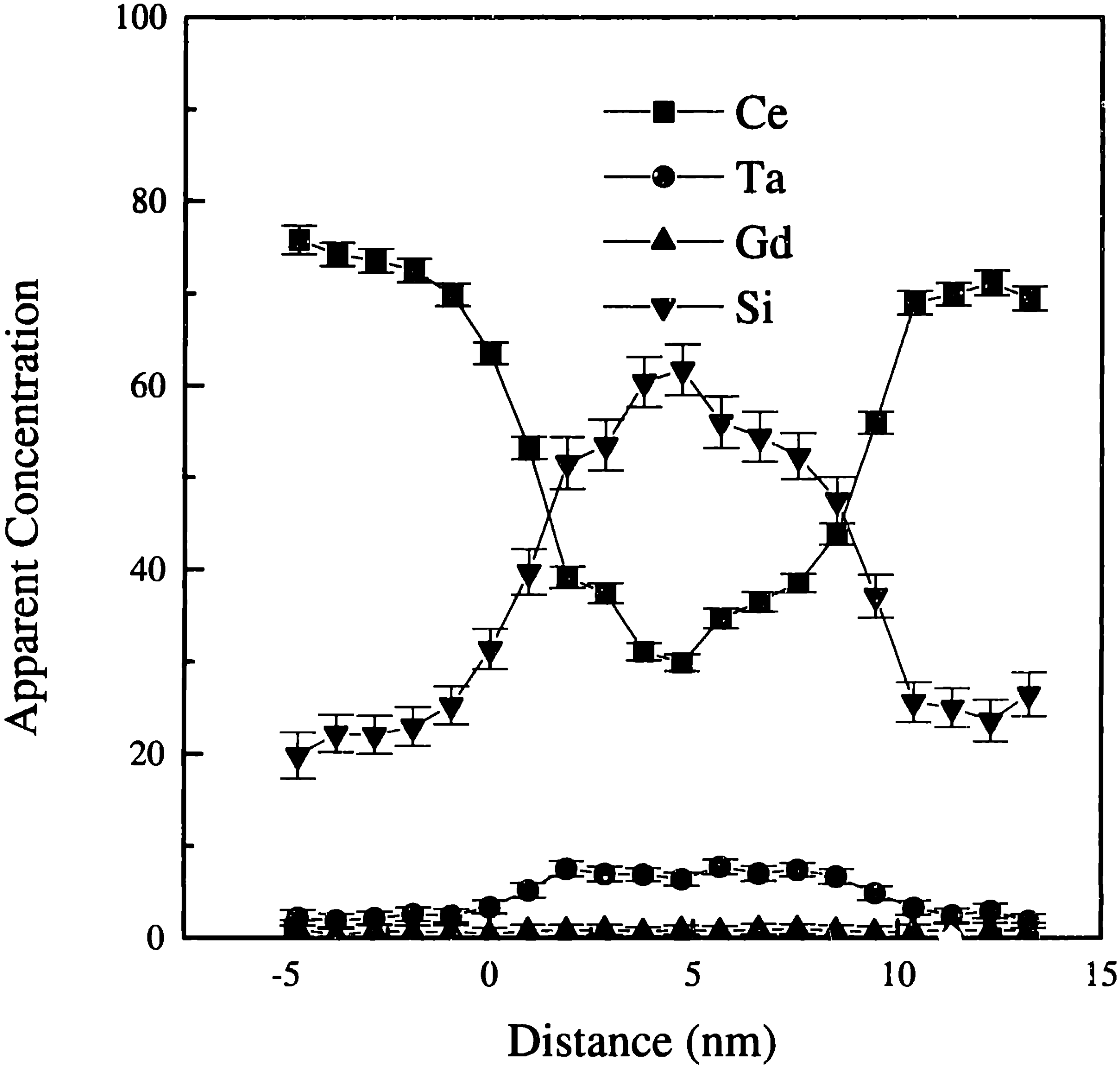

Figure 4-20: X-ray linescan across the boundary seen in Figure 4-21.

Figure 4-21: High resolution electron micrograph of a grain boundary in CGT4 at which a 7.8 nm wide amorphous film exists

segregation at this interface. Ta^{5+} both adsorbs at the glass/crystal interface and dissolves into the siliceous amorphous film. The exceptionally large excess of Ta^{5+} at this interface is explained by the thick amorphous Ta-Si glass combined with Ta^{5+} adsorption to the first atomic plane of the grains.

Figure 4-25 is a HREM micrograph from another boundary in CGT4. The glassy layer is 5.4 nm wide in this case. The X-ray linescan across this film is seen in Figure 4-22. Again, the Ta^{5+} is distributed uniformly across the film thickness. The area-scan measurement yielded 1.3 monolayers of Ta^{5+} and 0.1 monolayers of Gd^{3+}. The Ta^{5+} content of the glass accounts for 0.63 monolayers of the total excess per grain. The remaining Ta^{5+} is concluded to be adsorbed at the glass/crystal interface.

Finally, Figure 4-26 shows a thin amorphous film between two grains of CGT4. The film is 2.2 nm wide. The X-ray linescan is seen in Figure 4-23. It is less clear for this thinner film what the actual concentration profiles are. The convolution of the electron probe shape with the concentration profile becomes significant at this length scale. The Ta^{5+} coverage was measured as 0.73 monolayers, while the Gd^{3+} coverage was 0.04 monolayers.

Further evidence that the Ta^{5+} is segregating in the film is seen in Figure 4-24. Plotting the Ta^{5+} coverage measured by the area-scan technique versus the amorphous film thickness as observed by HREM, it is clear that for sample CGT4 a linear correlation exists. The line shown is a least-squares fit to the CGT4 data. This linear correlation suggests that the film compositions are constant in CGT4. The thicker films have a larger Ta^{5+} excess due to the larger volume of glass. The data from sample Ta3 are also plotted. At two "dry" grain boundaries significant Ta^{5+} segregation was measured. The Ta^{5+} segregation in sample Ta3 appears to be primarily adsorption at the glass/crystal interface with a small contribution to the overall excess due to the glassy phase.

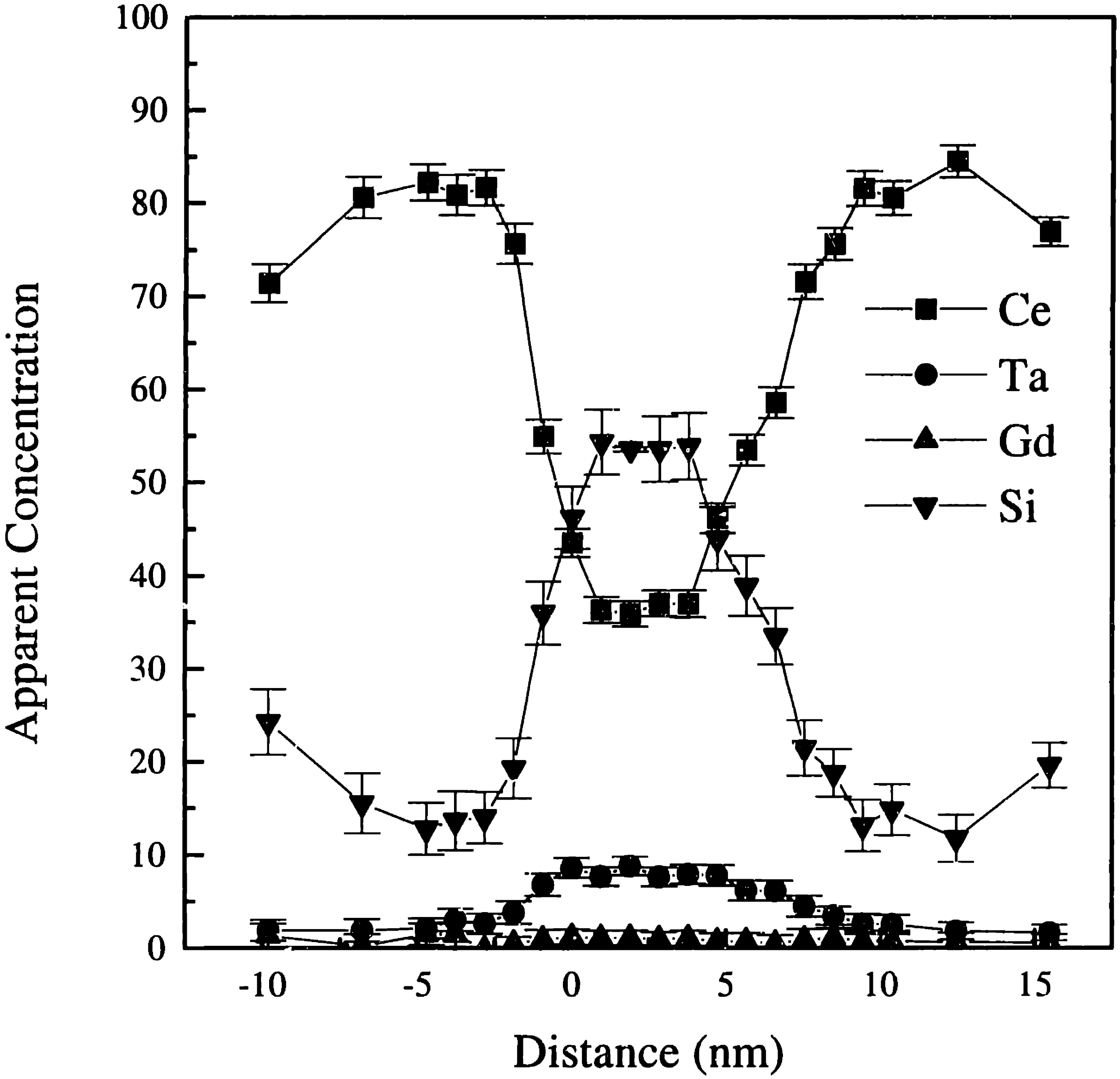

Figure 4-22: X-ray linescan across the boundary seen in Figure 4-25.

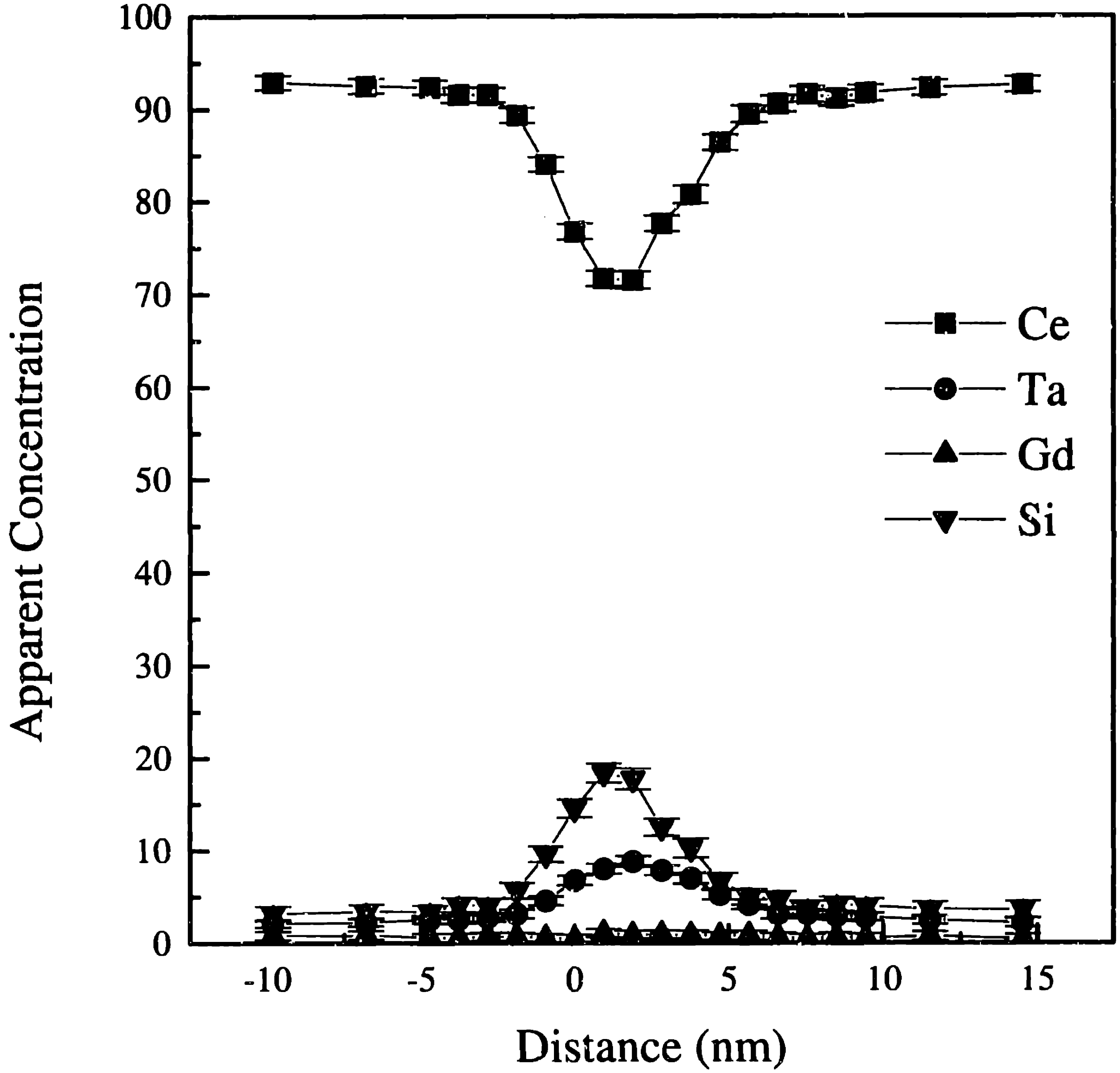

Figure 4-23: X-ray linescan across the boundary seen in Figure 4-26.

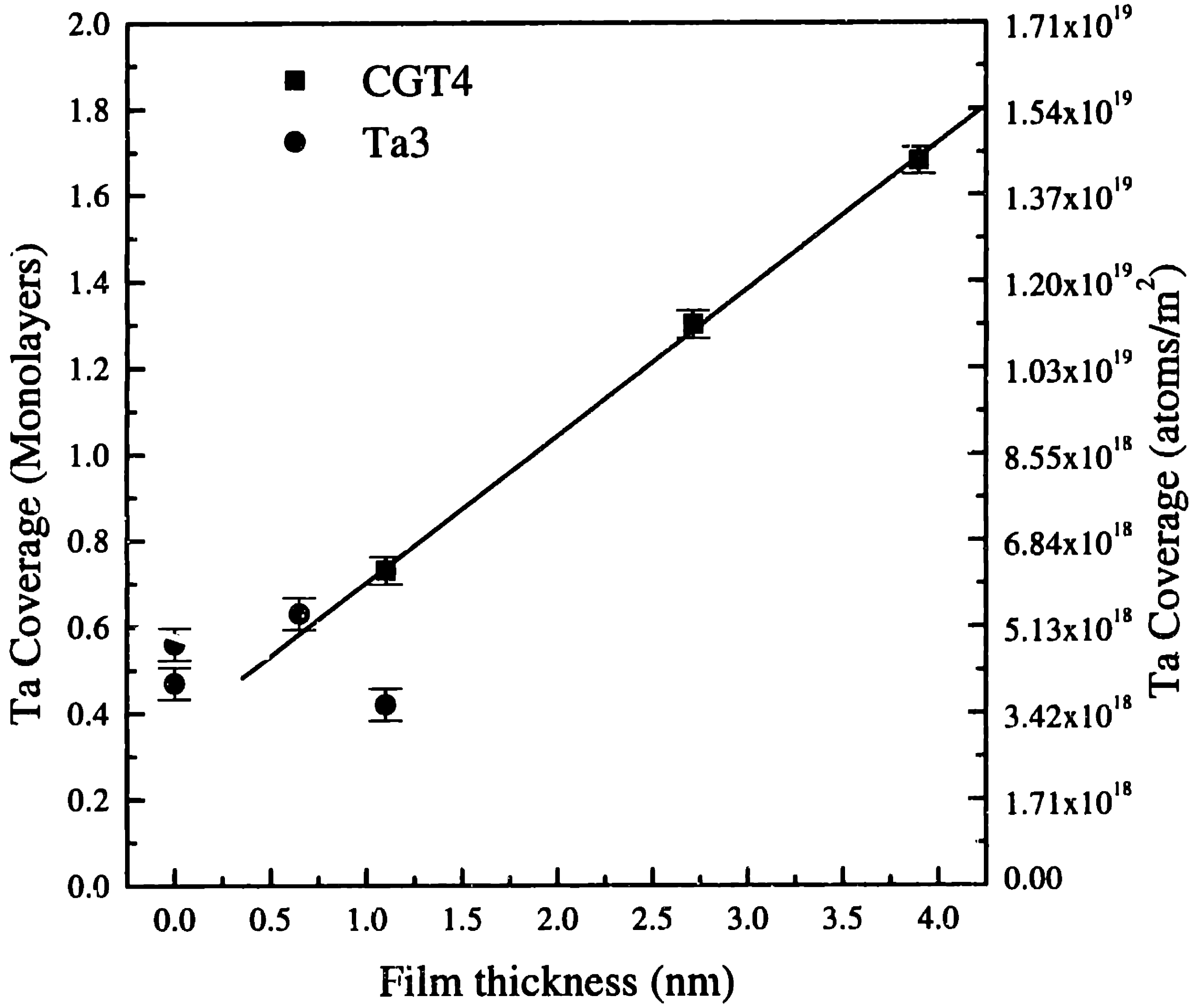

Figure 4-24: Ta^{5+} coverage versus grain boundary film thickness in CGT4 and Ta3.

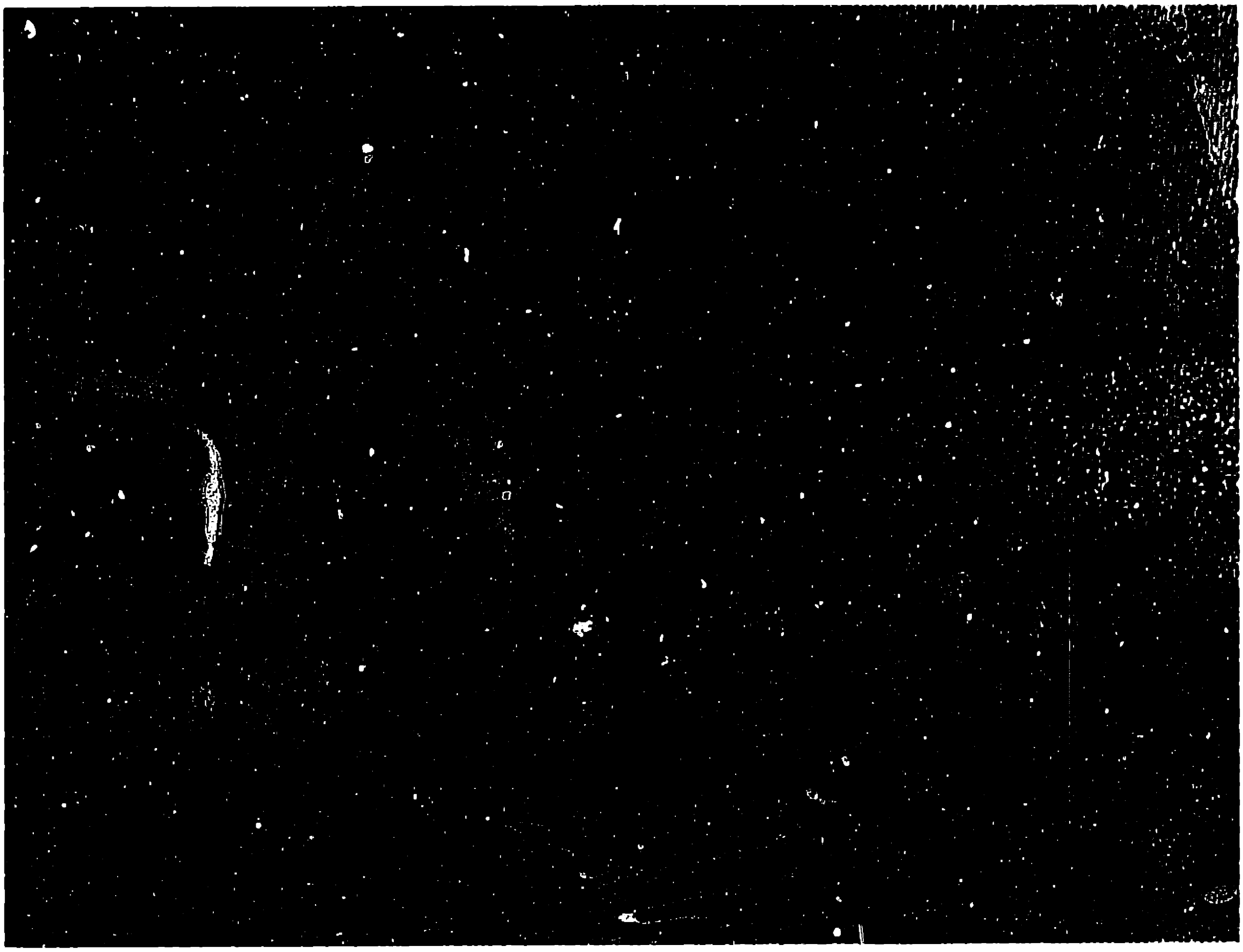

Figure 4-25: High resolution electron micrograph of a grain boundary in CGT4 at which a 5.4 nm wide amorphous film exists

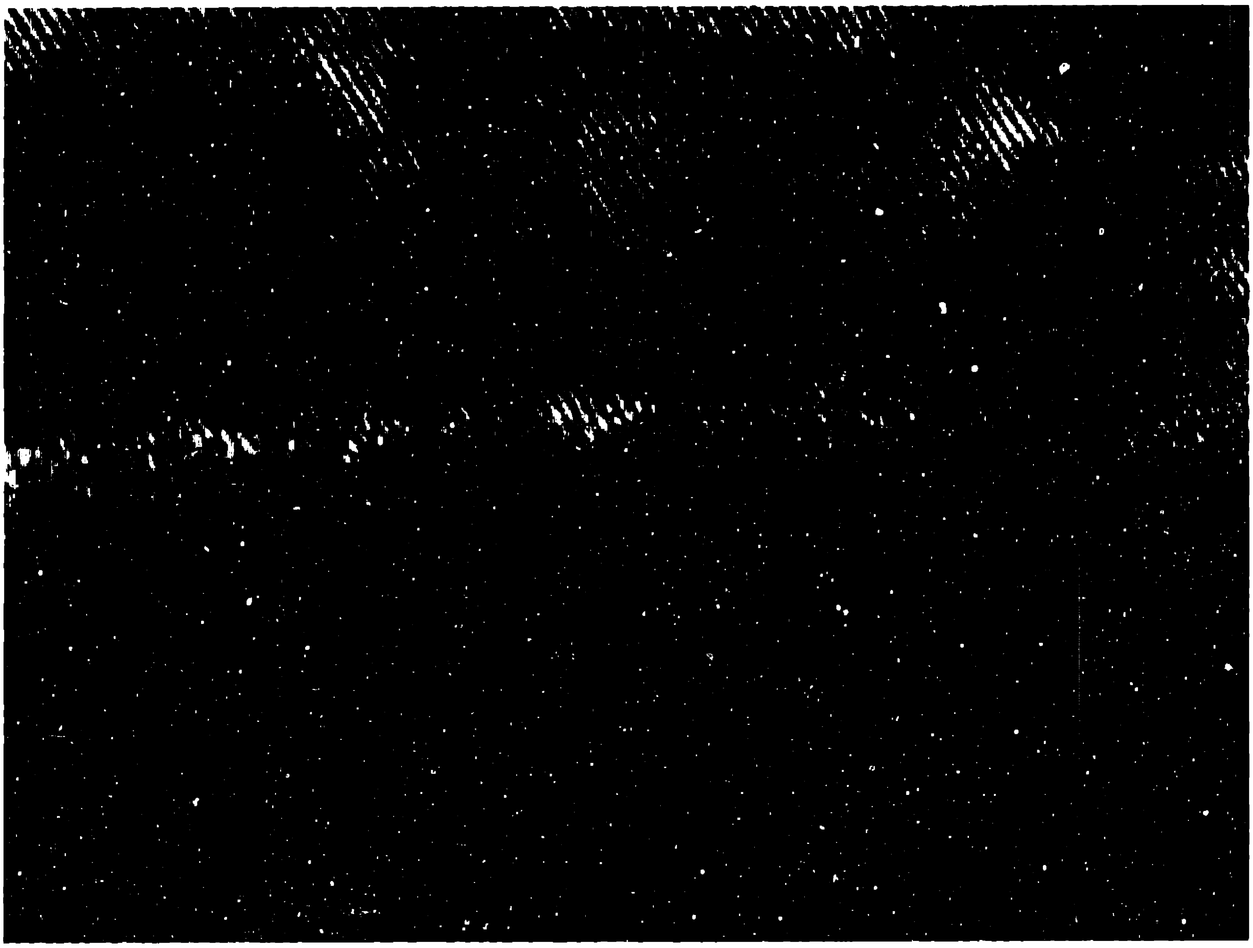

Figure 4-26: High resolution electron micrograph of a grain boundary in CGT4 at which a 2.2 nm wide amorphous film exists

Additional data suggesting that Ta^{5+} adsorbs at the glass/crystal interface in addition to being distributed in the glass is the ordinate intercept of the regression line for the CGT4 data. The intercept is equal to a positive value of 0.36 monolayers, suggesting that at a dry grain boundary in CGT4, Ta^{5+} adsorption of this magnitude would be expected. This observation coupled with the previous measurement of Ta^{5+} segregation at interfaces lacking amorphous phase suggests that the total excess of Ta^{5+} is due to the combined adsorption of Ta^{5+} at the glass/crystal interface and dissolution of an equilibrium amount of Ta^{5+} into the siliceous glass. Even for the uncommonly thick film seen in Figure 4-21, only approximately half of the observed Ta^{5+} excess is associated with the glassy film.

Cosegregation of Ca and Si has been previously observed by STEM and HREM in high purity zirconia samples without amorphous intergranular films [9]. In that system it was found that for a high bulk Ca concentration (15%), the Ca segregation remained less than a monolayer and scaled with the Si segregation, implying that Ca segregated only to the extent necessary to create a preferred grain boundary chemistry. A similar effect is not seen in Ta^{5+} doped ceria. The observations from sample Ta3 showed little effect of amorphous film formation on the level of Ta^{5+} segregation. Two crystal/crystal interfaces were measured and had Ta^{5+} segregation similar to measured segregation at interfaces with amorphous films as seen in Figure 4-24. The boundary to boundary variance was similar to other samples in which no siliceous films were observed. Upon film formation, Ta^{5+} is incorporated into the film to form an amorphous film composition in equilibrium with the Ta^{5+} in the ceramic grains. For sample Ta1 and Ta3 with relatively thin films, the majority of Ta^{5+} segregating to the interface is associated with adsorption and not the Ta^{5+} content of the siliceous glass. Glass formation at a boundary is concluded to not significantly affect the Ta^{5+} adsorption process.

Despite a consistent processing procedure for all samples, Si levels of the present

Ta samples observed with HREM ranged from 0.02 to 0.38 mole % Si, and were not proportional to Ta content (Table 3.2). No apparent correlation between the average Ta^{5+} segregation and bulk Si content was found. If there was a strong cosegregation effect, either positive or negative, we would expect to see an isotherm which would not follow a typical Langmuir shape. A positive cosegregation effect would cause more Ta^{5+} to segregate in samples rich in Si (such as Ta2), while a negative effect would depress Ta^{5+} segregation in Si rich specimens. The experimental isotherm is well fit by a Langmuir model and therefore, we conclude that *strong* cosegregation interactions do not exist between Ta^{5+} and Si in ceria.

The quantity of Si in the two Ta^{5+} containing samples observed by HREM is more than a factor of 2 less than that in the Gd^{3+} containing samples, (see Table 3.2). Yet the Gd^{3+} specimens exhibited clean boundaries while the Ta^{5+} specimens contained intergranular films. Samples co-doped with an excess of Ta^{5+} also exhibited siliceous films. The solubility of impurity Si in ceria clearly varies with the bulk concentration of $V_O^{\cdot\cdot}$, although the exact mechanism of compensation is unclear at this time. One possible mechanism is the increase of Si solubility in subvalent doped ceria due to the presence of $V_O^{\cdot\cdot}$. Tetrahedral coordination of O^{2-} around Si is greatly preferred due to the covalent nature of the Si—O bond. In undoped ceria, the cations are surrounded by a cube of O^{2-} ions. Si ions in undoped ceria exist in a high energy state and therefore, the solubility of silicon in ceria is expected to be minimal. Doping ceria with subvalent cations is well known to be charge compensated by the creation of $V_O^{\cdot\cdot}$. The large concentration of $V_O^{\cdot\cdot}$ in the lattice may increase the solubility of Si by allowing for lower coordination of O^{2-} around the Si ions. The defect complex shown in Figure 4-27 is the extreme example of the lower coordination of Si due to $V_O^{\cdot\cdot}$. If this suggested mechanism is correct, the implication is that doping fluorite structure oxides with supervalent ions, which decrease

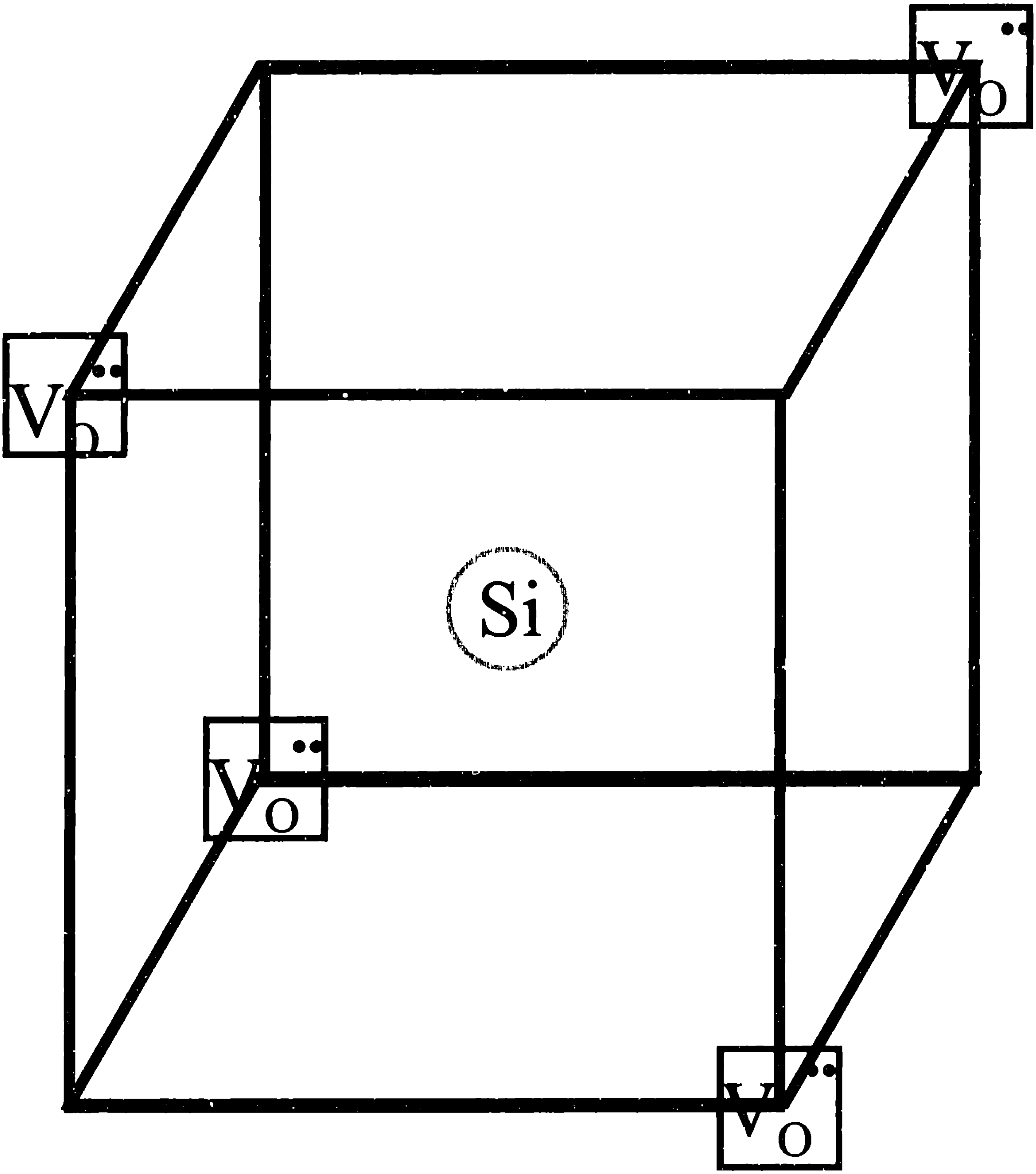
$V_O^{\bullet\bullet}$
$V_O^{\bullet\bullet}$
Si
$V_O^{\bullet\bullet}$
$V_O^{\bullet\bullet}$

Figure 4-27: Proposed low energy defect complex for Si in ceria suggested to increase the solubility of Si.

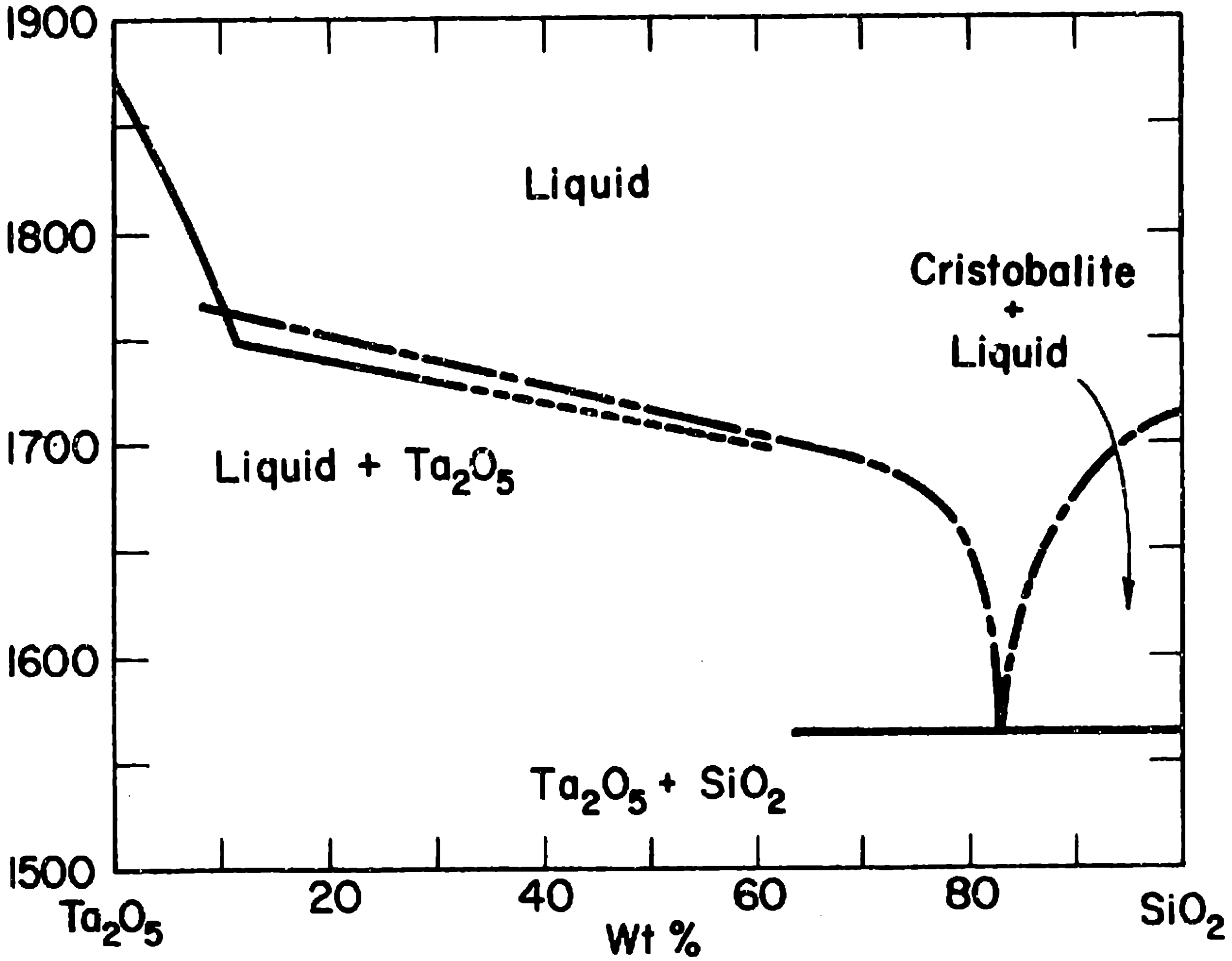

Figure 4-28: The Ta_2O_5-SiO_2 binary phase diagram

the $V_O^{\cdot\cdot}$ concentration in the material, will lead to rejection of Si from the crystal and the formation of siliceous grain boundary films. Additionally, lightly doped ceria would be more susceptible to the formation of siliceous films due to the lower concentration of $V_O^{\cdot\cdot}$ in the bulk. This proposed mechanism is consistent with the observed grain boundary morphology in both Ta^{5+} and Gd^{3+} doped ceria.

The binary Ta_2O_5-SiO_2 [88] and Gd_2O_3 [89] phase diagrams are seen in Figures 4-28 and 4-29. No ternary phase diagrams for Ce, Si and Ta or Gd have been reported. The eutectic temperature in the Ta-Si diagram is $\approx$ 1550°C, while in the Gd-Si system,

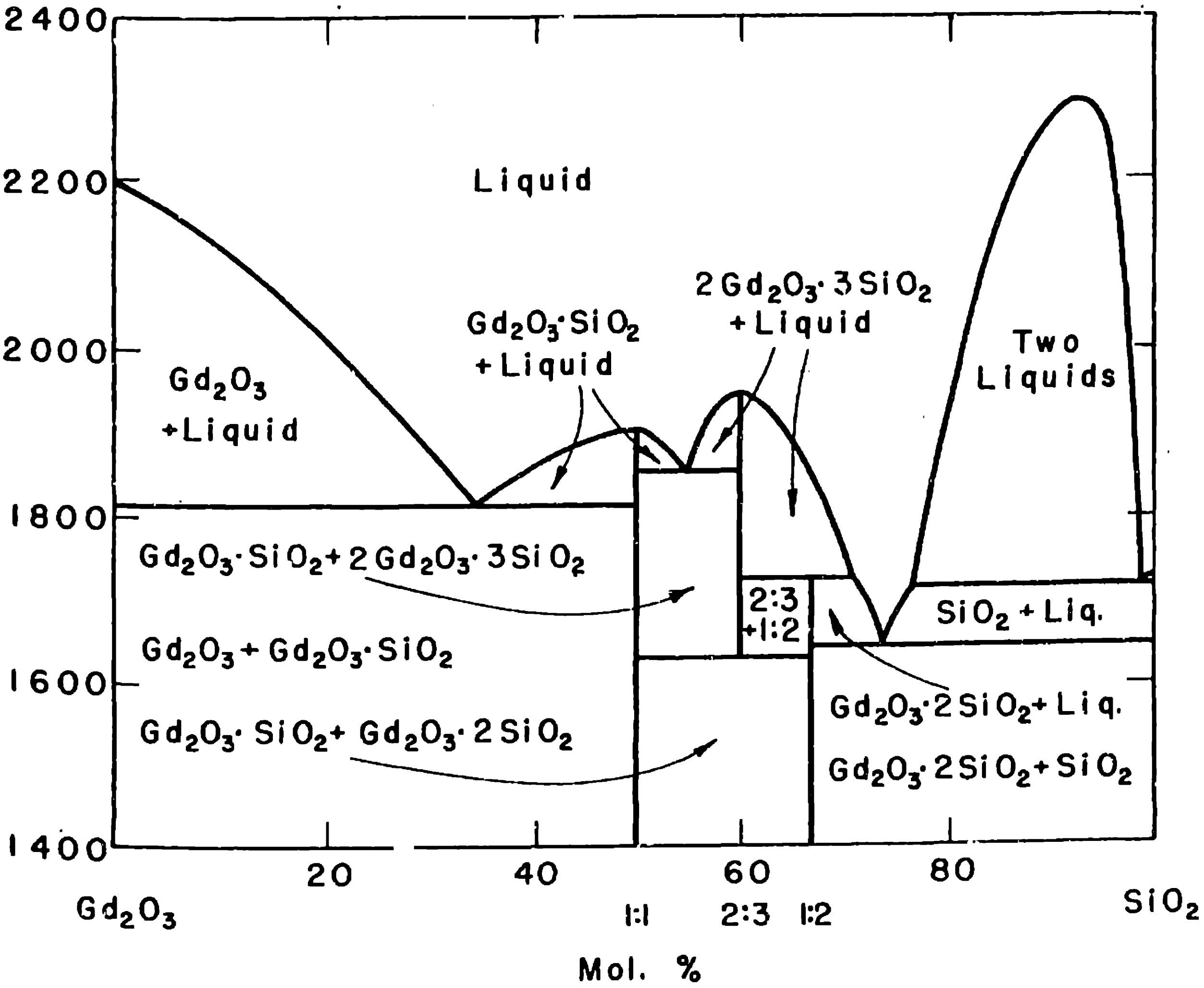

Figure 4-29: The Gd_2O_3-SiO_2 binary phase diagram

$T_{eutectic} \approx 1650°C$. All processing was done below the binary eutectics, though the existence of a possible ternary eutectic cannot be ruled out. However, recent results in the ZnO-Bi_2O_3 system have shown that even below the solidus it is possible for an intergranular amorphous film to be thermodynamically stable [90,91]. Wang and Chiang reported that amorphous Bi films are the equilibrium grain boundary morphology in ZnO-Bi_2O_3. Pressure desegregation experiments conclusively showed that the measured Bi excess in their samples was associated with the amorphous films and not a space charge layer.

For Ta^{5+} doped ceria, the results therefore show that the measured Ta^{5+} segregation is not a space charge phenomenon. The Ta^{5+} both adsorbs at the glass/crystal interface and segregates into the amorphous siliceous films. Gd^{3+} segregation in ceria is a space charge phenomenon and no amorphous films are observed even in samples containing a larger amount of Si than the Ta^{5+} doped specimens. The adsorption of Ta^{5+} to the grain boundaries in ceria promotes the formation of amorphous films that are enriched in Ta^{5+} and Si relative to the bulk of the grains. If the crystal/crystal interface energy becomes larger than two times the glass/crystal interface, a thin amorphous glassy layer will be thermodynamically stable as recently observed in the ZnO-Bi_2O_3 system [90,91] and the TiO_2-SiO_2 system [92]. Because Gd^{3+} segregation does not occur in the first atomic plane of the interface, the interfacial energy is not significantly changed and amorphous Si films are unstable with respect to the crystal/crystal interface.

4.5 Implications for Transport Properties

Gerhardt and Nowick [15,16] reported that the grain boundary impedance in ceria doped with between 0.3% and 6% subvalent dopant was due to the existence of thick ($\approx$ 50 nm) Si-containing films. They found that by eliminating the films, they were able to remove the majority of the "grain boundary effect". Unfortunately, they did not calculate the specific grain boundary resistance, σ_{gb}^{sp}, which is necessary to understand the conduction across a single boundary.

More recent results indicate that even in the absence of silicate films the grain boundaries are blocking in fluorite structure oxides [9, 14]. Aoki *et al.* reported on impedance measurements of high purity calcia-stabilized zirconia. Grain boundary segregation of Si was controlled through grain size control. In the very pure samples ($\leq$ 80ppm Si) studied, grain sizes below 4 μm exhibited size-dependent segregation due to the limited quantity of Si. Correspondingly, σ_{gb}^{sp} increased with decreasing Si segregation. The limiting value of the grain boundary conductivity was still more than 10^2 less than the bulk conductivity. Additionally, the activation energy of the bulk conductivity was reported to be lower than the activation energy of the grain boundary conduction mechanism suggesting that constriction effects cannot account for the large resistivity of the grain boundaries. Christie and van Berkel [14] correlated the microstructure and grain boundary conductivity in ceria doped with 20 mole % Gd. HREM was used to show the absence of any amorphous grain boundary films. Christie and van Berkel report that σ_{gb}^{sp} is 10^3 less than the bulk conductivity of their samples. The grain boundary conductivity mechanism had a clearly larger activation energy than the bulk mechanism, again suggesting that constriction effects are not a plausible explanation of the impedance data. Clearly, significant blocking effects occur in fluorite structure oxides even without glassy intergranular phases.

Maier has recently reviewed the problem of conduction through a space charge region [93]. Both the concentration of mobile defects and the mobility of the defects can potentially lead to blocking effects at interfaces. Current data in the silver halides can be effectively described assuming that the defect mobility is unchanged in the space charge region. For the case of a large electric field, as predicted in heavily doped ceria, the assumption of constant mobility may no longer be valid. No theoretical model exists to describe the effect of a space charge on ionic mobility. A depletion of mobile defects is predicted to lead to a lower conductivity perpendicular to the interface. The measured grain boundary conductivity is the integration across the space charge region of the local conductivity and as Hagenbeck and Waser [94,95] have shown for $SrTiO_3$, is dominated by the defect concentration minimum. The mobility effect would be manifested in the measured activation energy for conduction. Experimentally, both Aoki *et al.* [9] and Christie and van Berkel [14] have reported that the activation energy for grain boundary conductivity is ≈ 0.1eV greater than the activation energy of the bulk conductivity mechanism. For heavily doped ceria, the space charge potential is ≈ -0.65eV and is predicted to exist over a distance of 1 Å. The space charge model is based on continuum electrostatic theory and therefore does not take into consideration finite ion size effects. The space charge model therefore predicts that the electrostatic barrier to oxygen vacancy motion from one atomic plane to the next is 0.65 eV, and therefore the activation energy for conduction perpendicular to the interface should be larger than the bulk by 0.65eV. This is not consistent with the experimental data measured by Christie and van Berkel and Aoki *et al.*. Limitations of the space charge models include: the assumption of continuum dielectric behavior at the Å level, dilute solution approximation for defects in the space charge, and neglect of the discreteness of ions. The spatial extent of the space charge layer in the case of heavily doped ceria will be increased upon consideration of these effects. Therefore, it is expected that the potential drop from one atomic plane to the next will be in reality less than the predicted 0.65 V and may approach the experimentally measured 0.1 V.

The predicted depletion of $V_O^{\cdot\cdot}$ in the near grain boundary space charge is suggestive of why the grain boundaries are blocking in subvalent doped fluorite oxides in the absence of second phase siliceous films. The addition of subvalent dopants is required to generate the large concentration of $V_O^{\cdot\cdot}$ necessary for high oxygen ion conduction in the bulk. As a consequence, in this extrinsic limit, the grain boundary charge will always be positive, which implies depletion of positive defects such as $V_O^{\cdot\cdot}$ in the space charge. Figure 4-30 shows the calculated defect concentration profiles in Gd^{3+} doped ceria assuming a space charge segregation effect. These calculated profiles assume equilibration at 1500°C in air for ceria doped with 20 mole % Gd. Note the depletion of $V_O^{\cdot\cdot}$ in the near boundary space charge. $V_O^{\cdot\cdot}$ transport across the grain boundaries in fluorite structure oxides will be impeded due to the lower $V_O^{\cdot\cdot}$ concentration even in the absence of second phase intergranular glassy films.

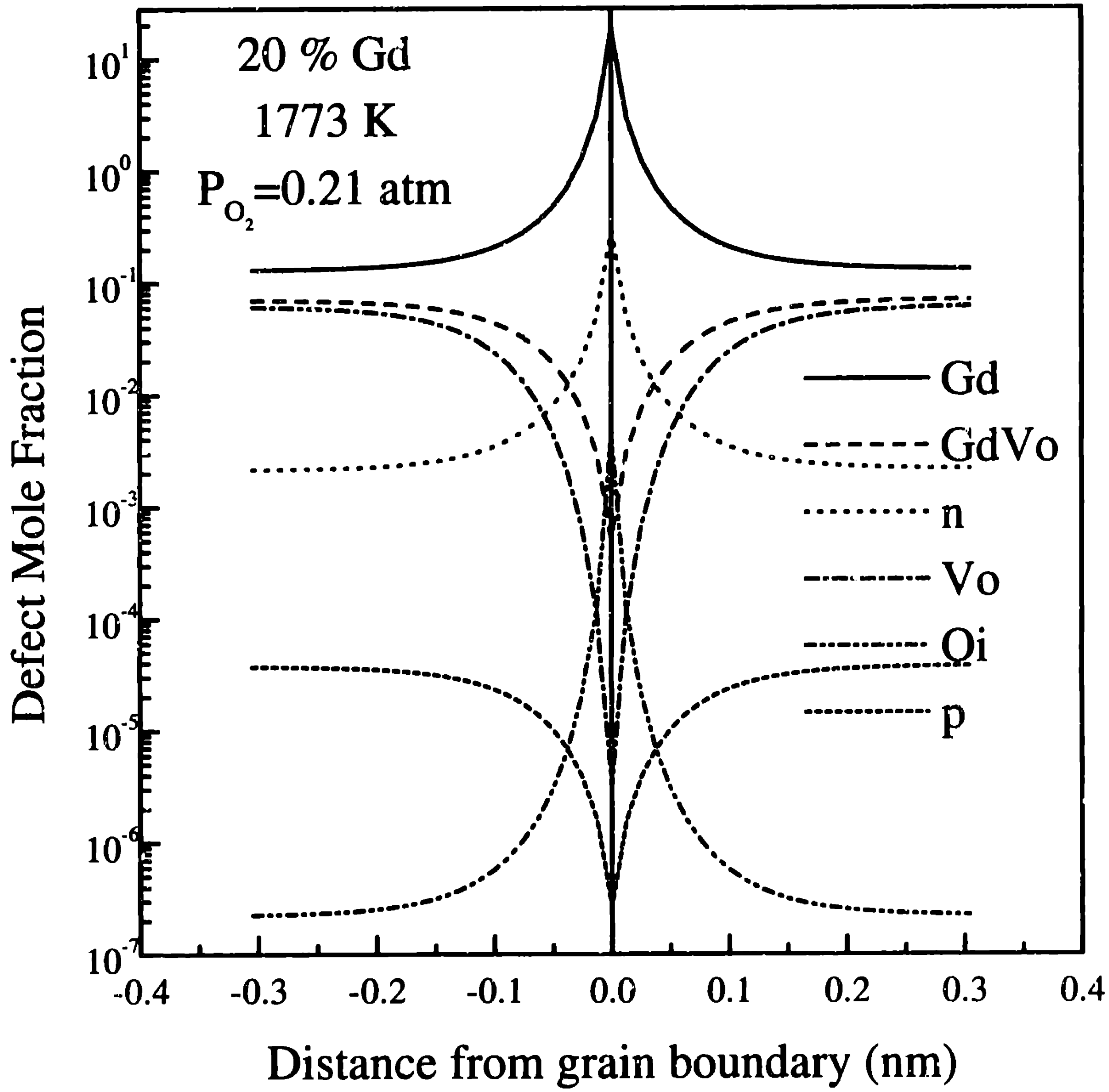

Figure 4-30: Defect profiles in 20 mole % Gd^{3+} doped ceria at 1773K and air atmosphere with a positive charge on the grain boundary and a negative space charge region.

Chapter 5

Conclusions

Extensive measurements of grain boundary segregation of Gd^{3+} in doped ceria have been performed and confirm that segregation of Gd occurs at sub-monolayer levels in samples containing between 1 and 26 mole % Gd. The experimentally measured isotherm can be fit over most of its composition extent with any of three models: a dilute space charge model originally developed by Kliewer and Koehler [53, 58–60], a limited interfacial site space charge model originally developed by Blakely and coworkers [62–64], and a simple Langmuir-type isotherm.

Although adsorption models and space charge models are based on different ideas about the driving forces for segregation and the location of the segregant, their isotherms are remarkably similar. In only a few cases is it justified to *a priori* argue that segregation in a particular ceramic must be due to electrostatic effects or adsorption. Before discarding any models, a detailed understanding of the defect chemistry of the system and values of the free energy of formation of key defects is required to argue that the magnitude of the electrostatic driving force is small and can be safely ignored.

In the case of aliovalent doped ceria, the defect chemistry has been solved and from the observation of acceptor segregation, an estimate of the key defect formation energy, $g_{V_O^{\cdot\cdot}}$, has been made. $g_{V_O^{\cdot\cdot}}$ in ceria is $\approx$ 2eV which is reasonable given the previously reported values of the Frenkel and Redox energies. We conclude that Gd'_{Ce} segregates in ceria predominantly due to electrostatic effects as embodied in the limited-site space charge model described in Section 2.1.2. The measured Gd^{3+} segregation can be most closely modeled with an isotherm derived from a limited-site space charge model. The derived free energy of adsorption in a Langmuir-type isotherm for Gd^{3+} is unreasonable for the elastic misfit of the Gd^{3+} ion on a Ce^{4+} site. Gd'_{Ce} in ceria represents an ideal space charge dopant due to its small size misfit with the host Ce^{4+} ion which minimizes elastic strain. Other acceptors such as Sc^{3+} and Sm^{3+}, with larger misfits will most likely segregate more strongly due to a combination of electrostatic and adsorption forces.

The space charge models predict that for donor doped ceria the interfaces should be positively charged with a depletion of donor solute in the space charge region. STEM measurements of a number of compositions containing Ta instead showed Ta^{5+} segregation in all cases. Ta^{5+} segregation in ceria is therefore not electrostatically driven. In fact, the electrostatics of the situation seek to deplete the boundaries of Ta. It is concluded that segregation of Ta^{5+} in ceria is driven by adsorption effects. Due to the similar size misfit of other potential donor ions such as Mn^{5+} and Nb^{5+}, we predict that they also will adsorbed at the grain boundaries in ceria.

Simultaneous segregation of Gd^{3+} and Ta^{5+} in ceria has been measured in a number of co-doped ceria samples. Both Gd^{3+} and Ta^{5+} segregate in sub-monolayer amounts for Gd $<$ 4.5% and Ta $<$ 2%. The Gd^{3+} segregation isotherm can only be explained with the space charge models. We conclude that the segregation of Gd^{3+} is exclusively due to space charge effects. This result is reasonable given the small misfit of the Gd'_{Ce} defect with respect to the host Ce^{4+} site. Ta^{5+} addition does not affect the amount of

Gd^{3+} segregation in the space charge since it does not have much impact on the defect chemistry within the Ta solubility limit.

Ternary adsorption models predict that Ta^{5+} should segregate more strongly in co-doped samples than in binary solid solutions. The opposite is in fact observed: Ta^{5+} segregation is depressed in co-doped samples. The magnitude of the depression of Ta^{5+} segregation cannot be satisfactorily explained by space charge depletion. From the Ta^{5+} segregation data, it is clear that there is a negative co-segregation effect of Gd^{3+} on Ta^{5+}.

From HREM observations of the grain boundary morphology in these aliovalent doped materials coupled with chemical information from STEM and SAES measurements, a clear difference is seen in the morphology of grain boundaries in Ta and Gd doped ceria. Gd doped ceria has dry boundaries without any intervening amorphous film. Grain boundaries in Ta doped ceria are separated by a thin film of Si containing amorphous material. The solubility of Si in ceria varies depending on the concentration of $V_O^{\cdot\cdot}$ in the bulk. The proposed explanation is that subvalent doping increases the Si solubility by raising the concentration of $V_O^{\cdot\cdot}$ and creating cation sites surrounded by 4 O^{2-} ions rather than the 8 typical for the cubic fluorite structure. The covalent nature of the silicon-oxygen bond is such that tetrahedral coordination is much preferred over any other coordination. $V_O^{\cdot\cdot}$ help stabilize the solution of Si into the ceria lattice. Doping ceria with Ta^{5+} or other supervalent ions is suggested to decrease the bulk solubility of Si due to the lower concentration of $V_O^{\cdot\cdot}$ in the lattice. and lead to the formation of thin intergranular siliceous films between the grains.

Table 5.1 outlines the projected driving forces for grain boundary segregation of other aliovalent dopants in ceria. The ionic radii are from Shannon [76] and are for eight-fold coordination of the cations. Supervalent dopants such as Ta^{5+} and Nb^{5+} are significantly undersized for the Ce^{4+} site in ceria and are therefore predicted to segregate due to

Table 5.1: Projected segregation driving forces for aliovalent dopants in ceria

Ion	Radius (pm) [76]	Driving force
Ce^{4+}	111	
Y^{3+}	116	Electrostatic
Gd^{3+}	119	
Mg^{2+}	103	
Sc^{3+}	101	Mixed electrostatic and adsorption
Sm^{3+}	122	
Nd^{3+}	125	
Ta^{5+}	88	Dominated by adsorption
Nb^{5+}	88	

adsorption effects. Subvalent dopants with misfit equal to or less than Gd^{3+} will segregate in a space charge to shield the positive charge on the grain boundaries. Subvalent dopants with a large size misfit are predicted to segregate due to the combined influence of space charge and elastic strain effects.

Figure 5-1 shows schematically the space charge segregation of Gd'_{Ce} in ceria and the combined Ta^{5+} adsorption at the glass/crystal interface and dissolution into a siliceous grain boundary amorphous film. Gd^{3+} segregates in the near boundary region in order to balance the charge on the grain boundary. This occurs regardless of Ta^{5+} segregation and/or amorphous film formation. The Gd^{3+} segregation falls exponentially from the interface to the bulk value over a length scale of approximately two Debye lengths ($2\kappa^{-1}$). Ta^{5+} segregation on the other hand, is an adsorption effect with the Ta^{5+} existing both at the glass/crystal interface and in an amorphous siliceous film between the grains. The Ta^{5+} is heavily segregated right at the first atomic layer of the grain and exists at a concentration in the glass greater than in the bulk of the crystal.

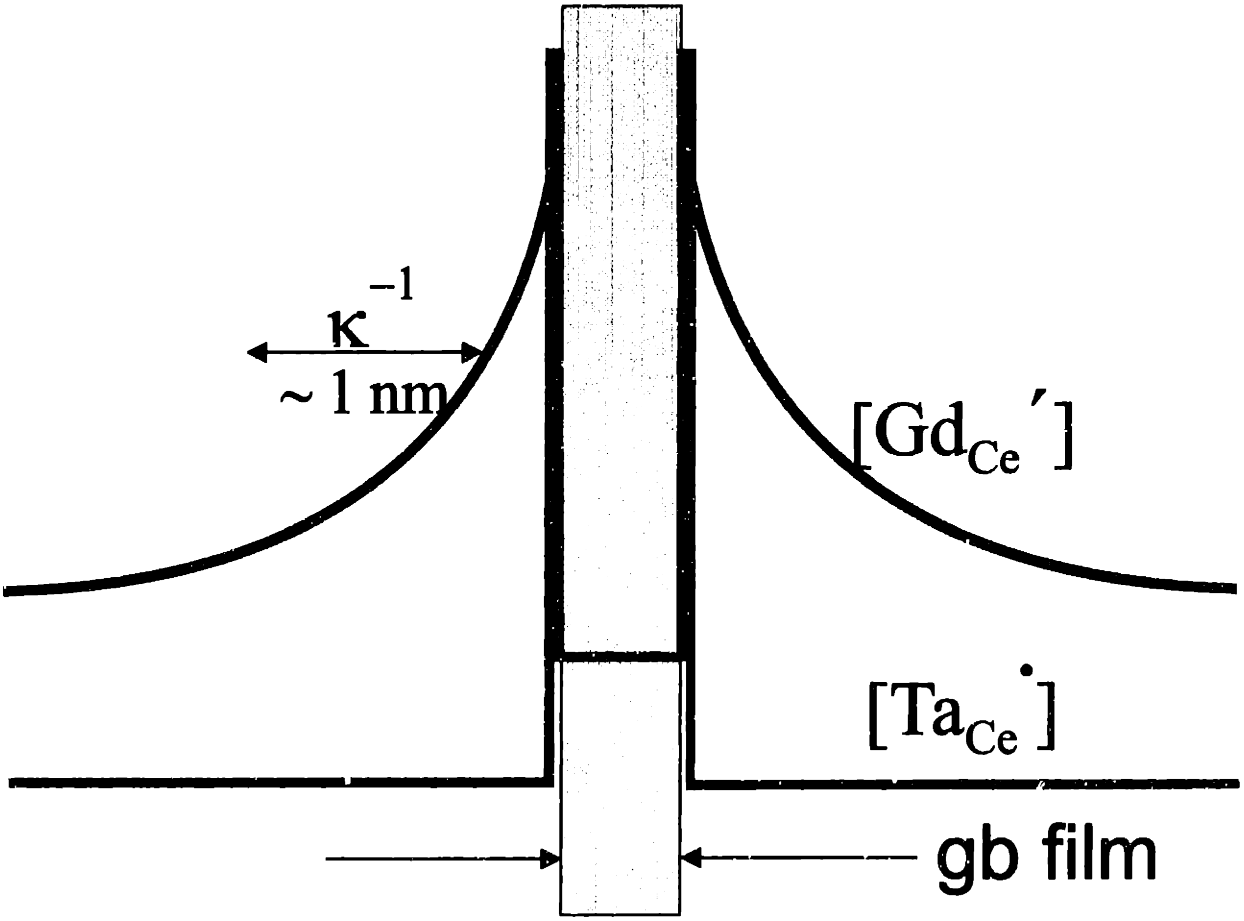
κ^{-1}
~ 1 nm
$[Gd_{Ce}']$
$[Ta_{Ce}^{\bullet}]$
gb film

Figure 5-1: Schematic diagram of Gd^{3+} in the space charge layer of ceria, Ta^{5+} adsorption at the glass/crystal interface and dissolution into the amorphous siliceous film.

Appendix A

Coverage Histograms

The following pages contain the histograms of the segregation measurements discussed in this thesis. The error bars on the individual grain boundaries are 95% confidence limits as described in Section 3.3. The sample identification as given in Table 3.2, along with the average segregation and confidence limits plotted in the figures in Section 4 are given above the histograms. Tabulated below each figure are the following experimental details: dopant mole%, number of counts at 4.840 keV (the Ce L_{α_1} X-ray line), and the size of the virtual objective aperture (VOA) used. The size of the VOA affects the electron probe size and total intensity of the probe. For highest spatial resolution, a 20μm VOA is necessary to limit the spherical aberration of the focussed electron probe. A larger VOA decreases the maximum spatial resolution, but increases the total beam intensity and hence the X-ray counting statistics for a given counting time. The area-scan technique uses a large (relative to the ultimate probe size) raster area and therefore the increased spherical aberration is acceptable given the large gains in the X-ray signal.

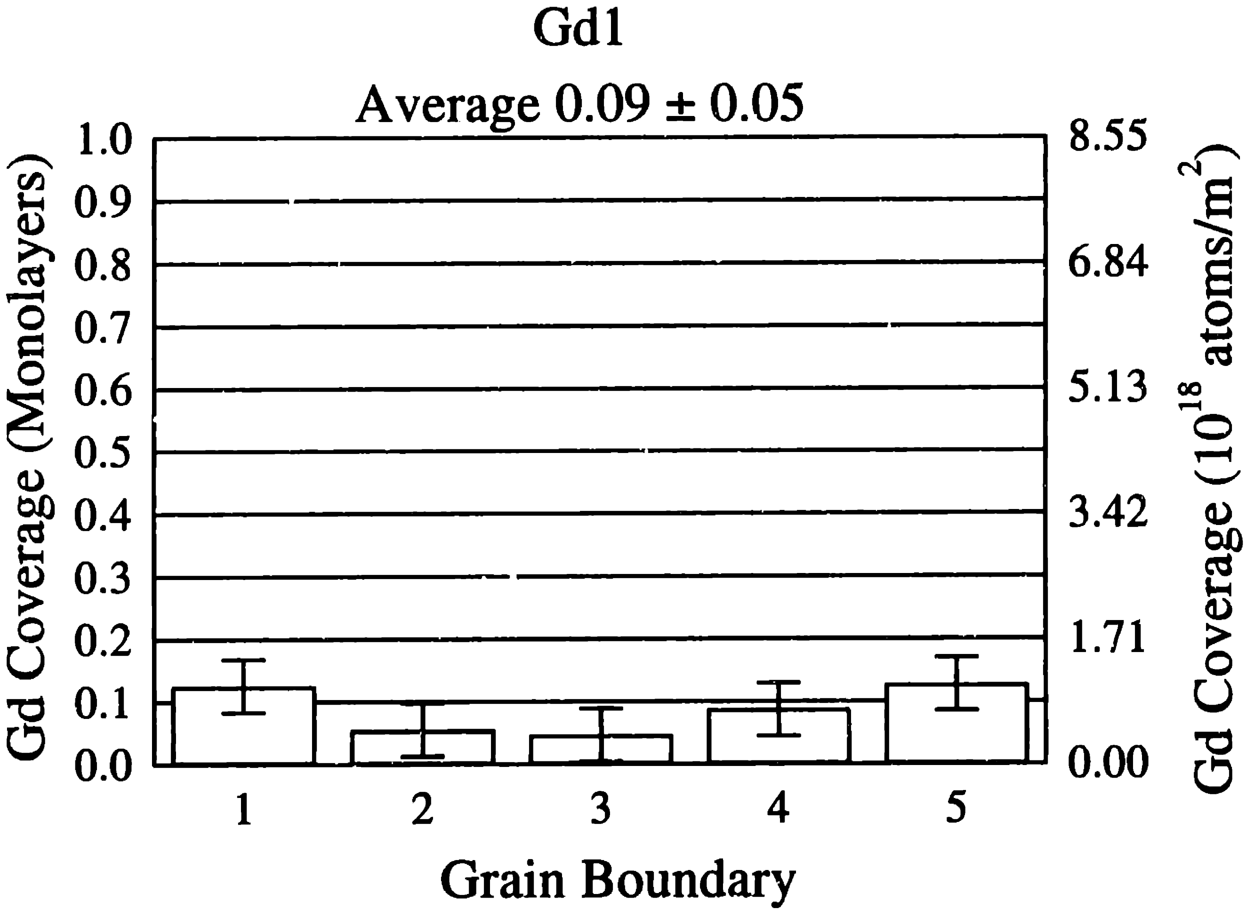

Gd	Ce L_{α_1} counts	VOA
1.28%	45,000	50 μm

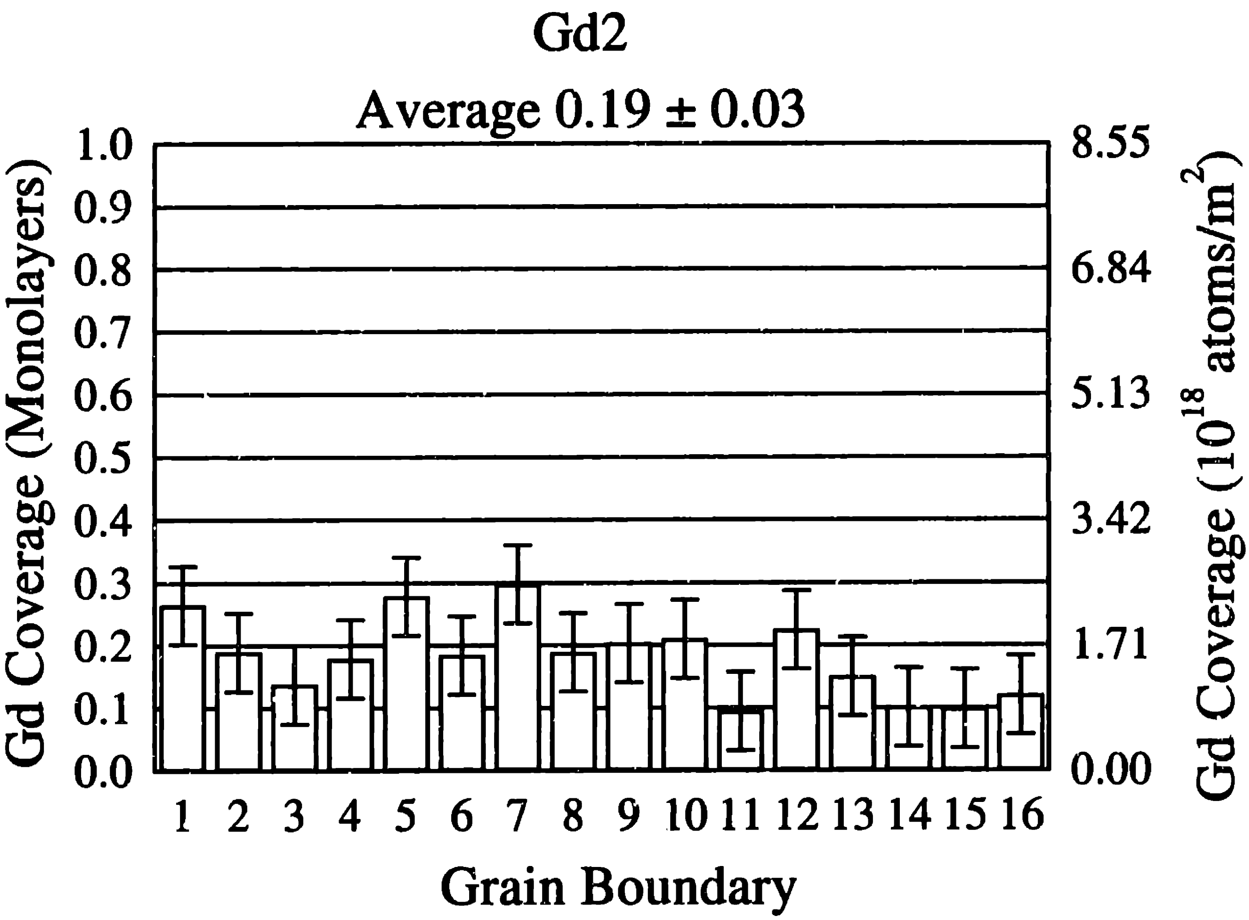

Gd	Ce L_{α_1} counts	VOA
1.76%	45,000	50 μm

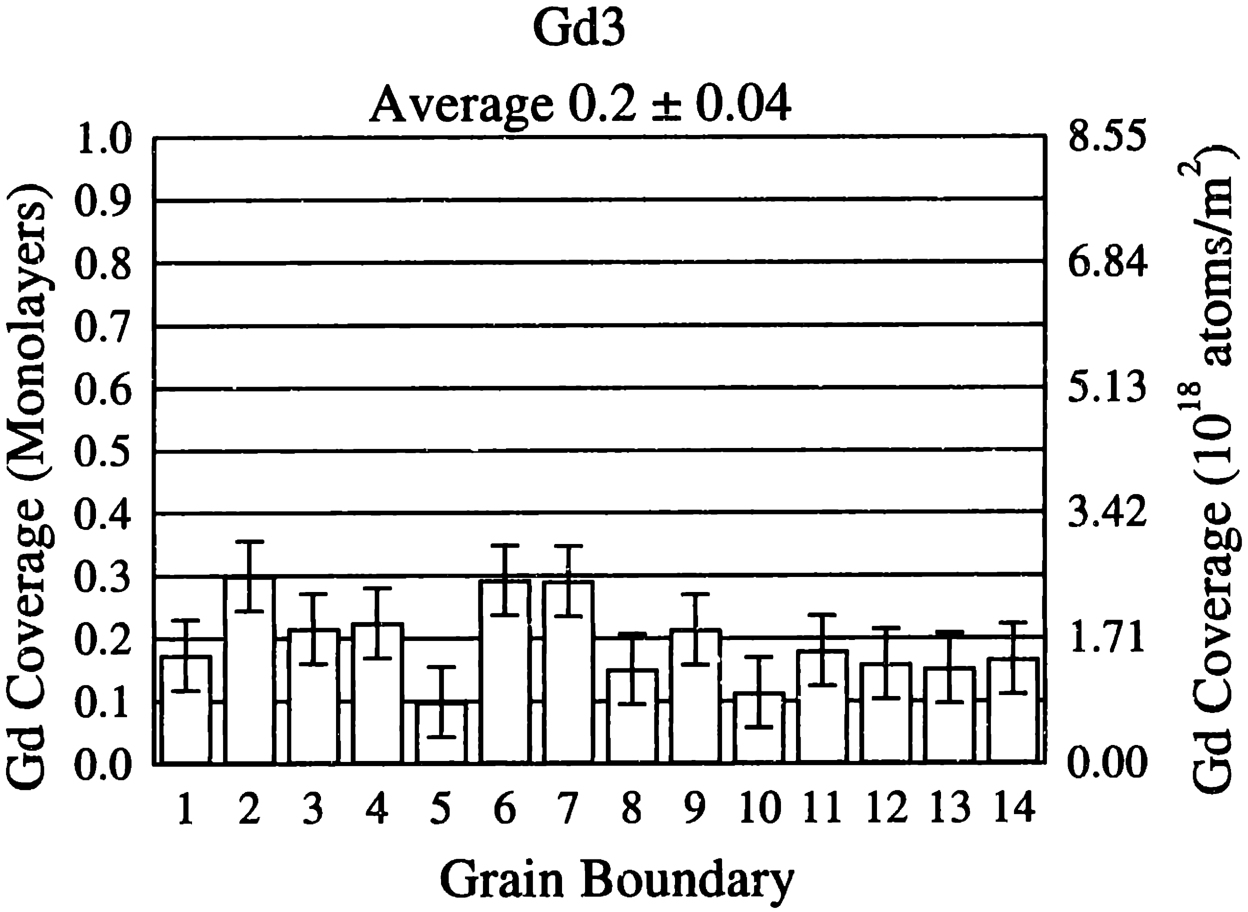

Gd	Ce L_{α_1} counts	VOA
1.87%	50,000	50 μm

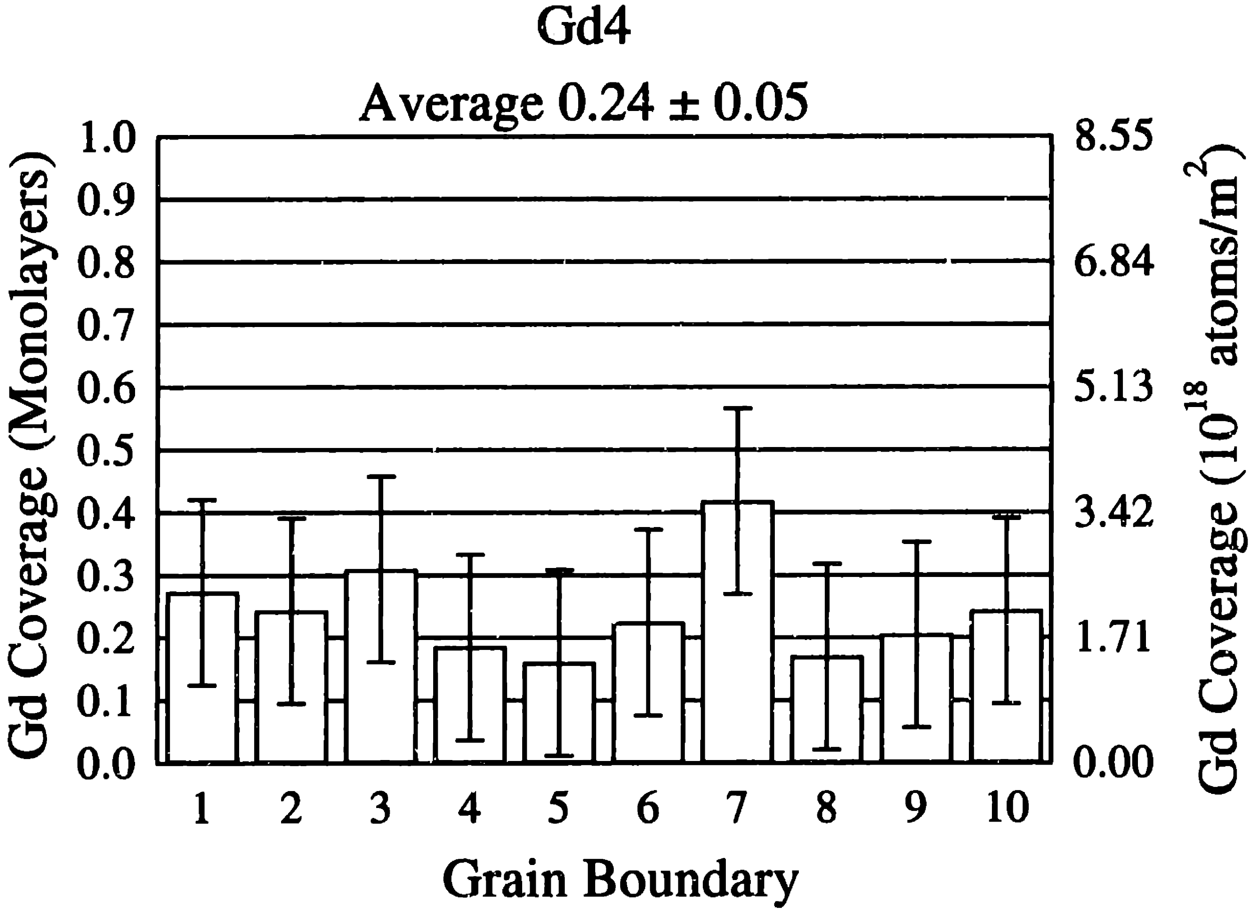

Gd	Ce L_{α_1} counts	VOA
4.85%	30,000	50 μm

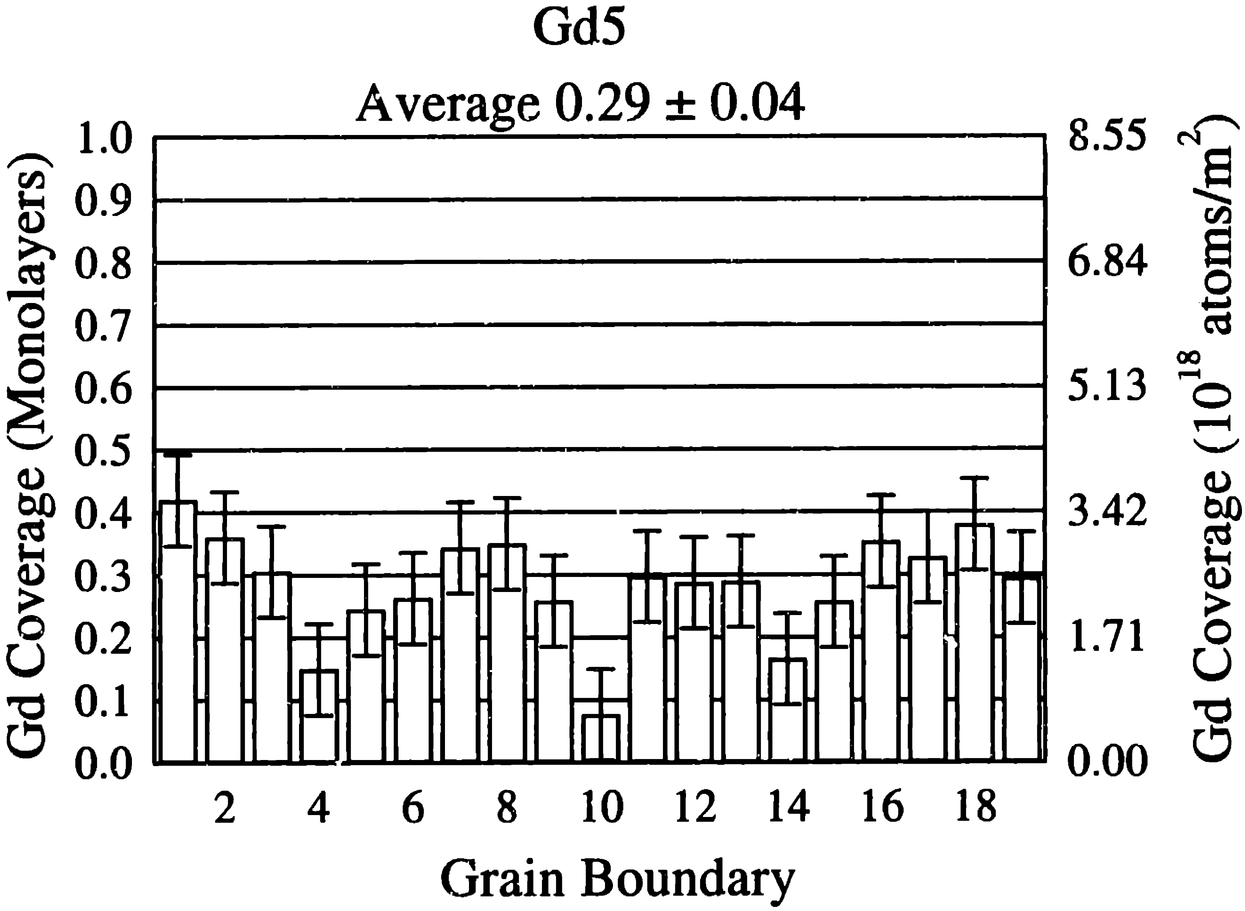

Gd	Ce L_{α_1} counts	VOA
7.57%	30,000	30,50 μm

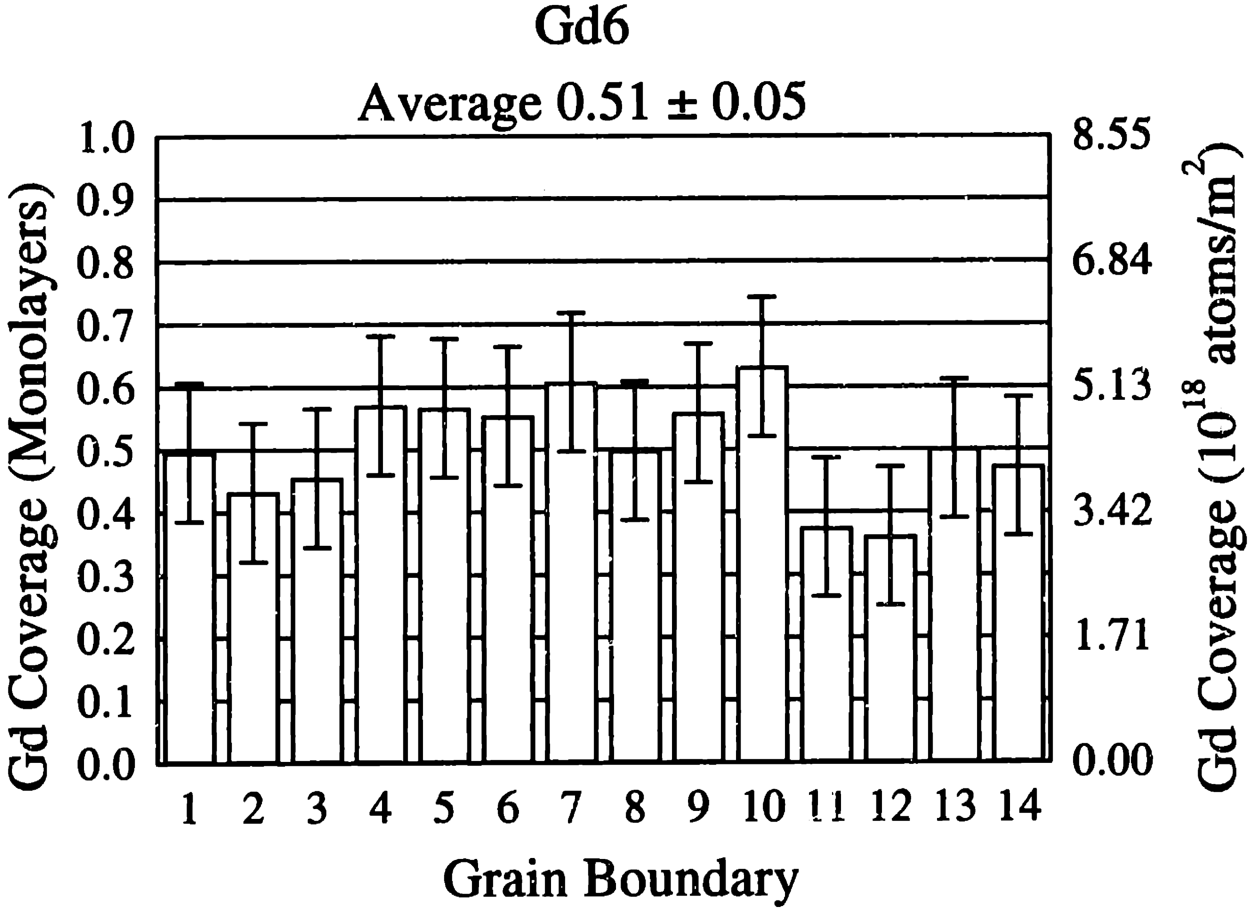

Gd	Ce L_{α_1} counts	VOA
23.7%	60,000	50 μm

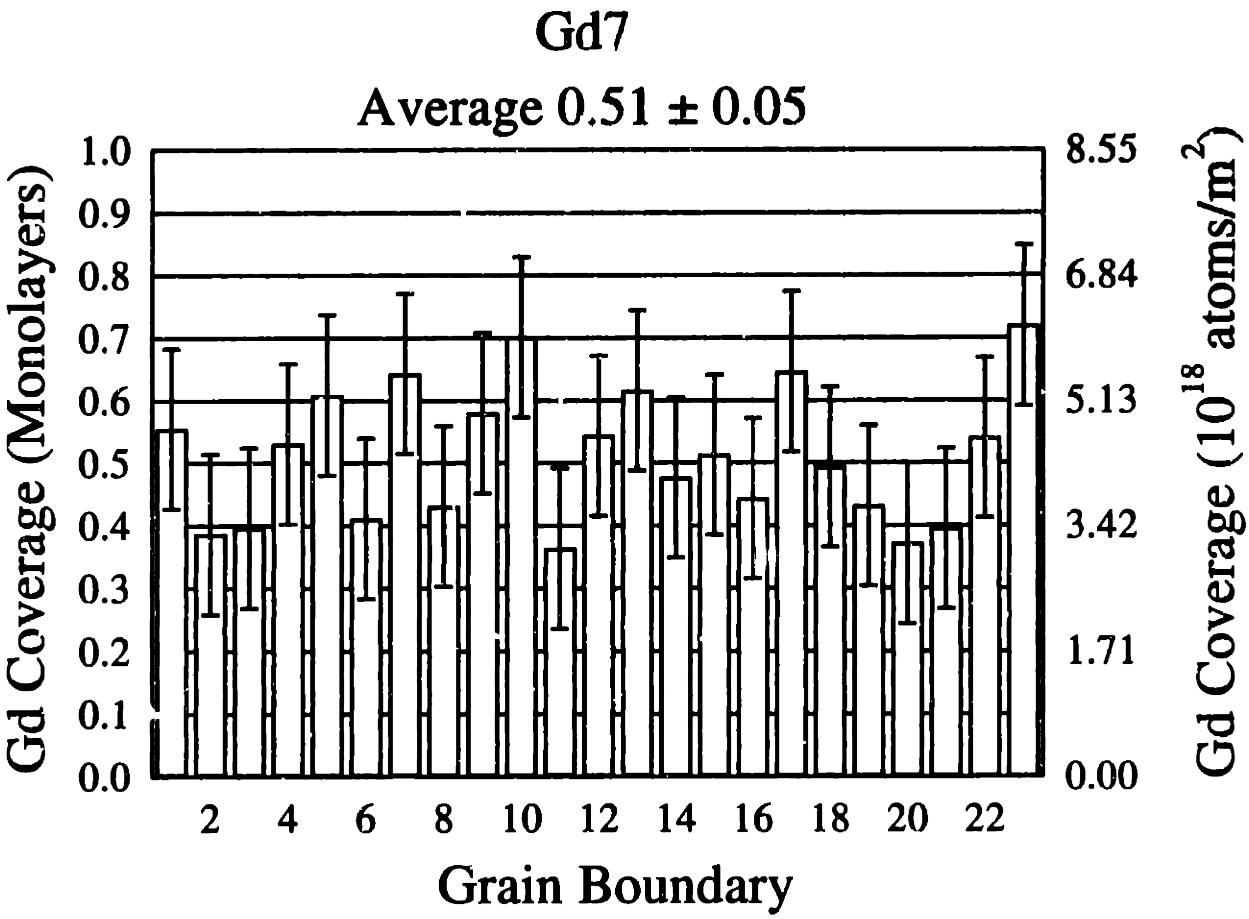

Gd	Ce L_{α_1} counts	VOA
25.7%	40,000	50 μm

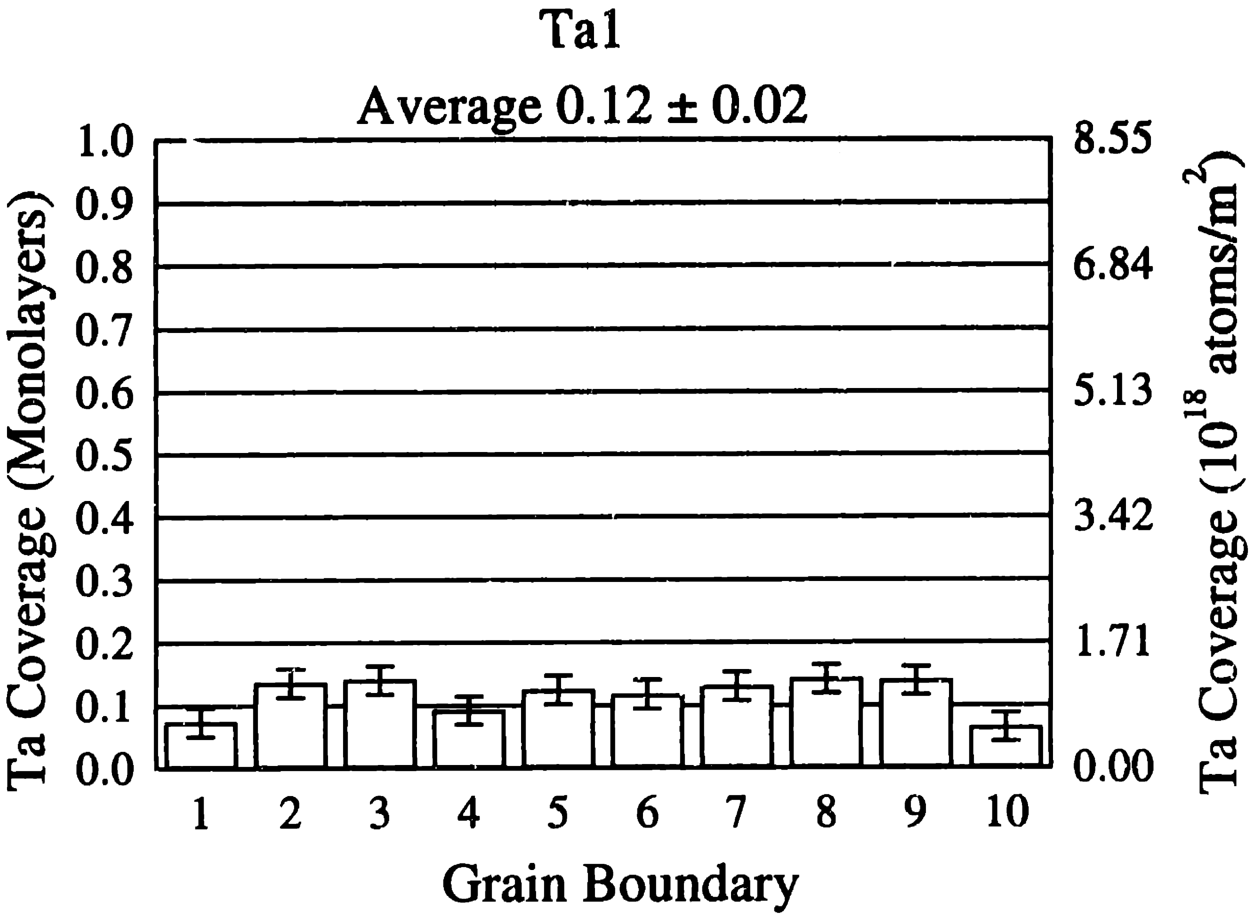

Ta	Ce L_{α_1} counts	VOA
0.28%	60,000	30 μm

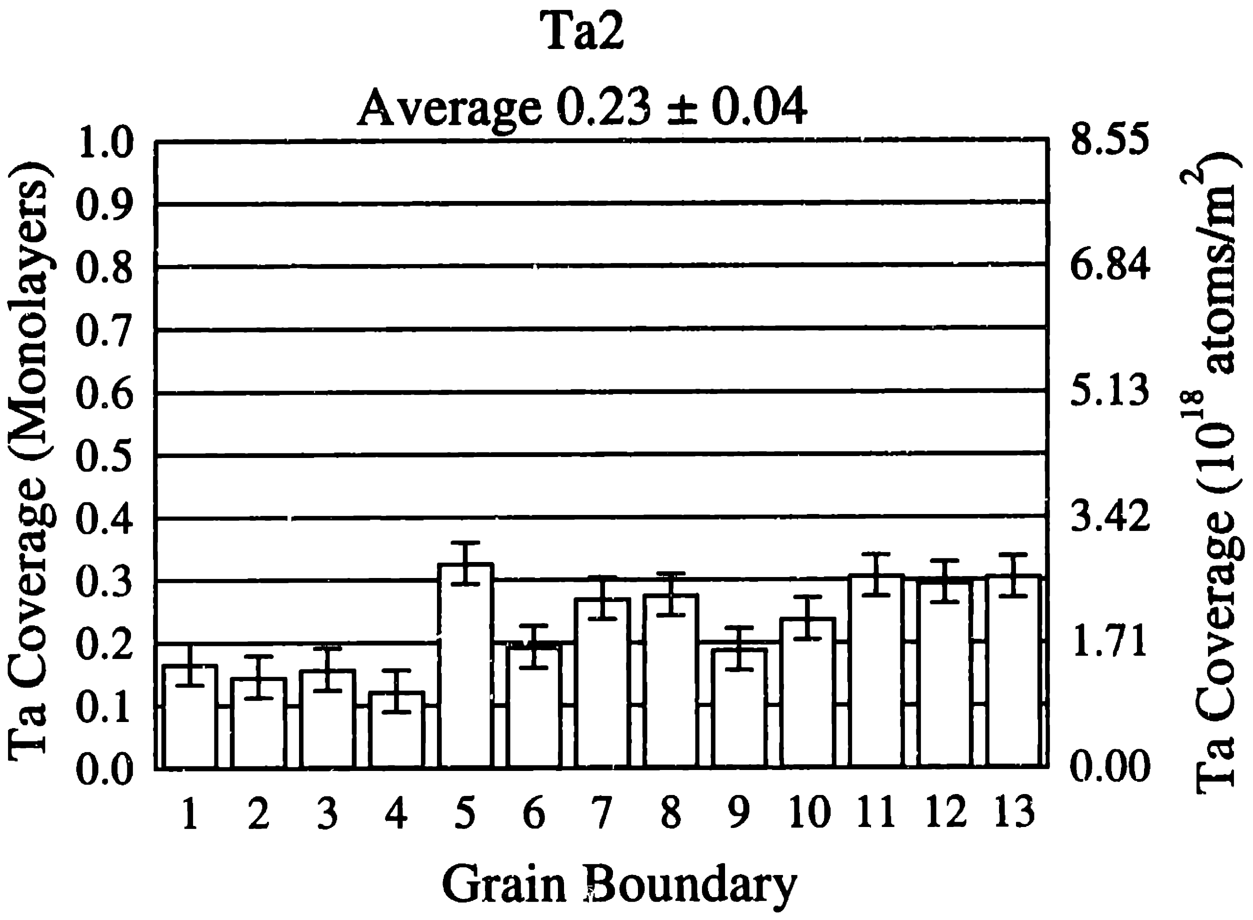

Ta2

Average 0.23 ± 0.04

Ta	Ce L_{α_1} counts	VOA
0.53%	60,000	50 μm

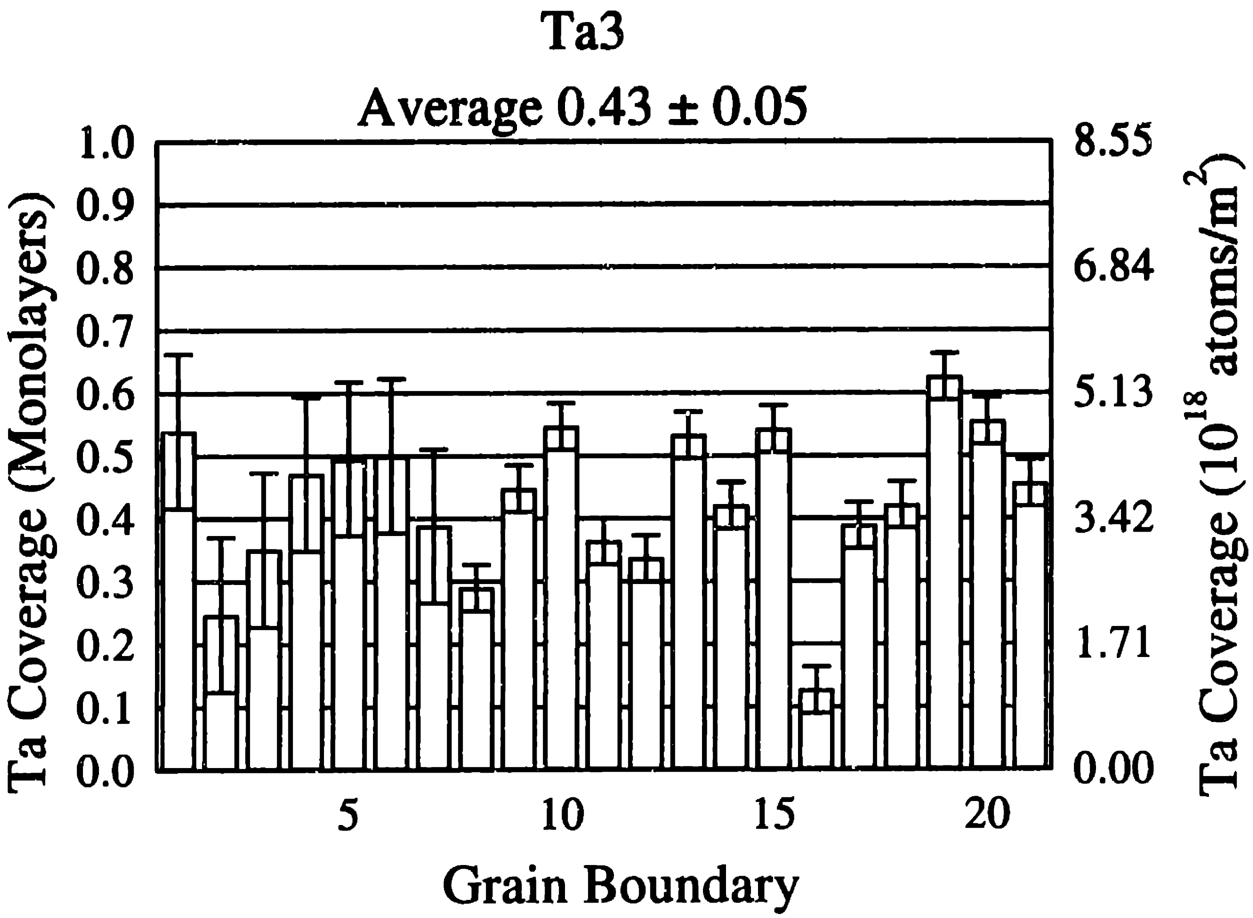

Ta	Ce L_{α_1} counts	VOA
1.79%	22,000 20,000[a]	50 μm

---

[a] Mo TEM support ring. Grain boundaries 8-21. Note the increase in precision.

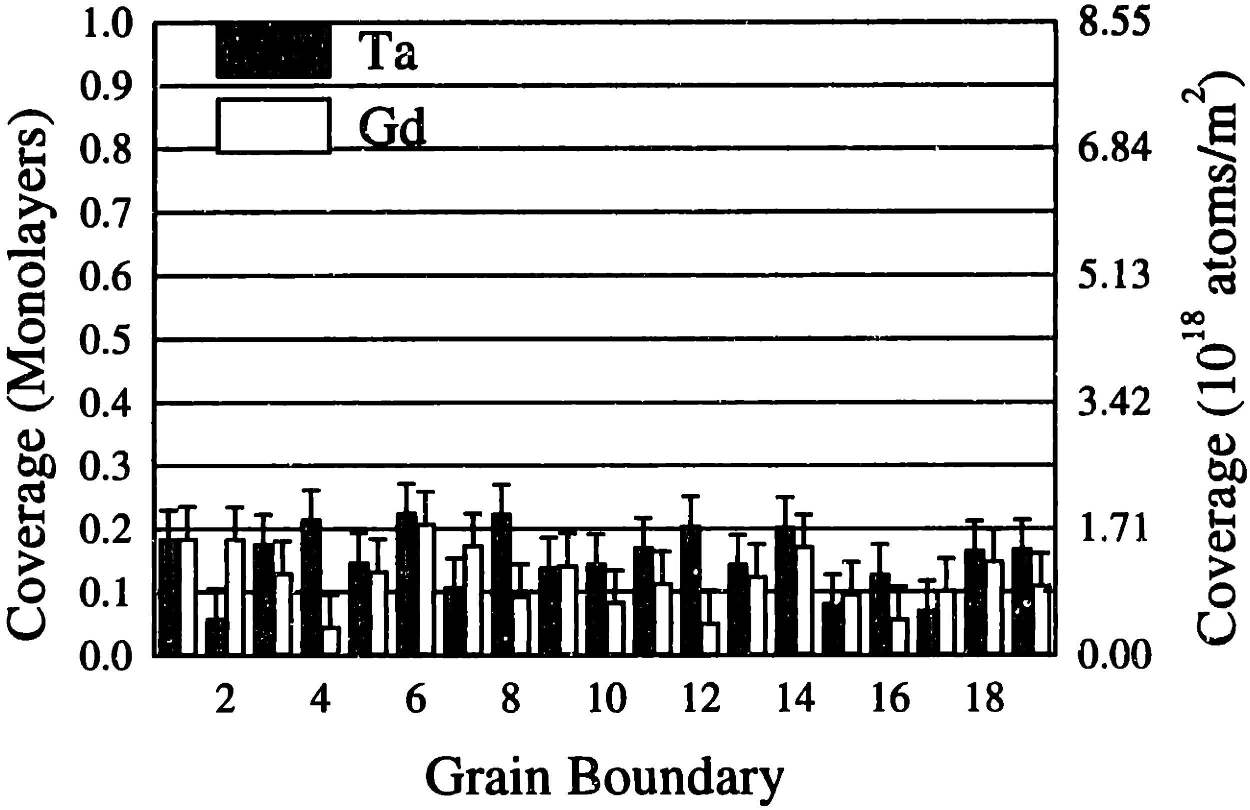

CGT1

Average 0.15 ± 0.03 Ta

0.12 ± 0.03 Gd

Gd	Ta	Ce L_{α_1} counts	VOA
1.54%	0.9%	45,000	30 μm

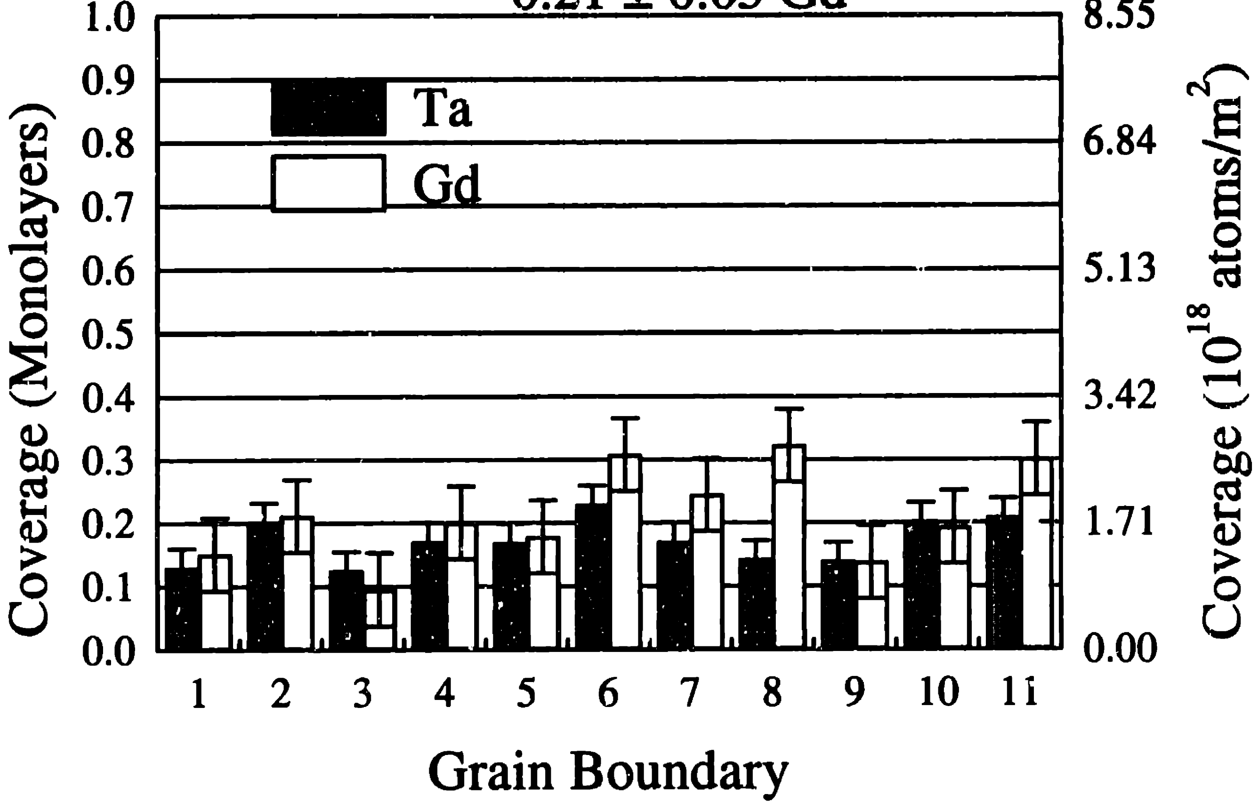

CGT2

Average 0.17 ± 0.02 Ta

0.21 ± 0.05 Gd

Gd	Ta	Ce L_{α_1} counts	VOA
4.21%	1.52%	30,000	50 μm

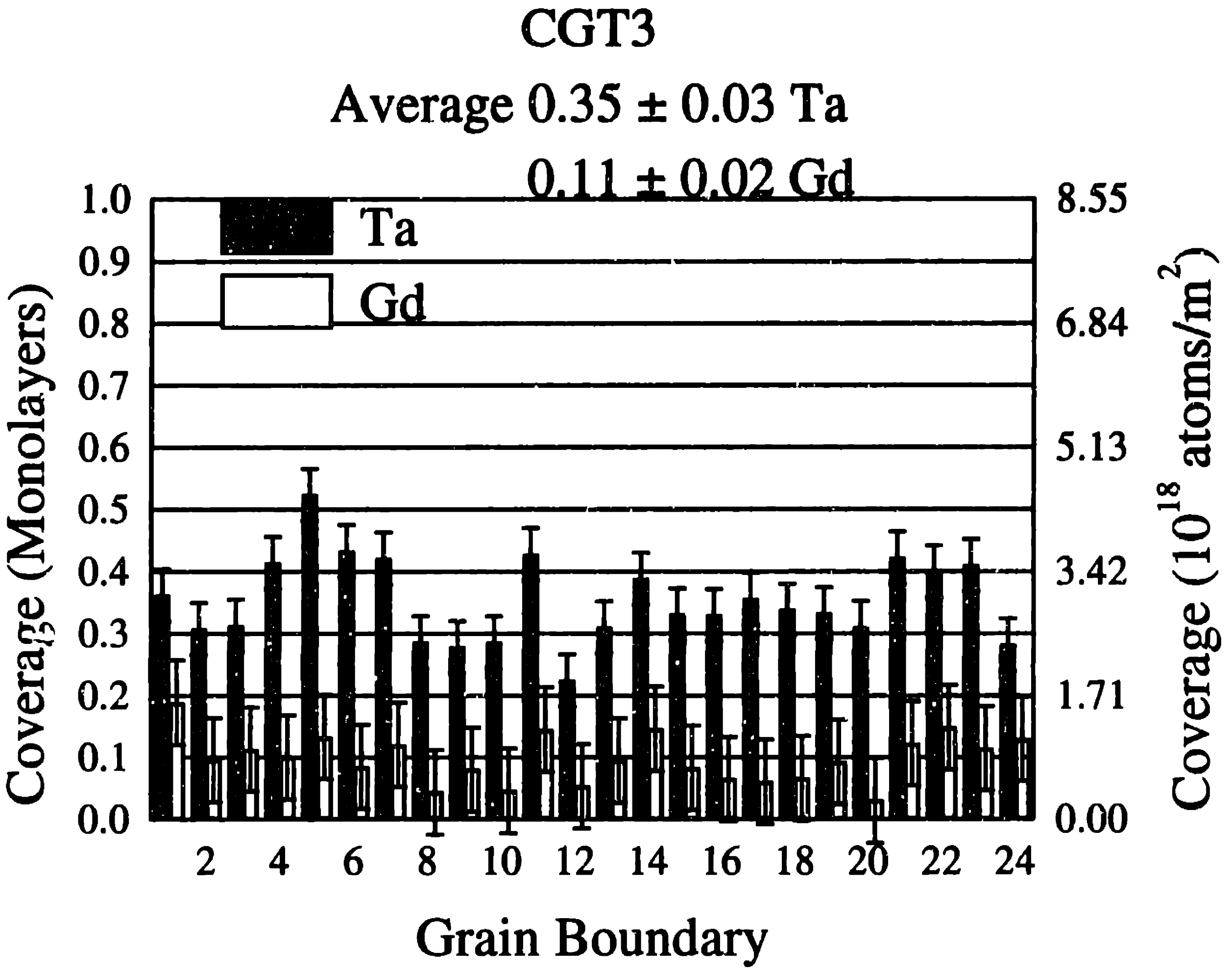

Gd	Ta	Ce L_{α_1} counts	VOA
1.48%	1.89%	45,000	50 μm

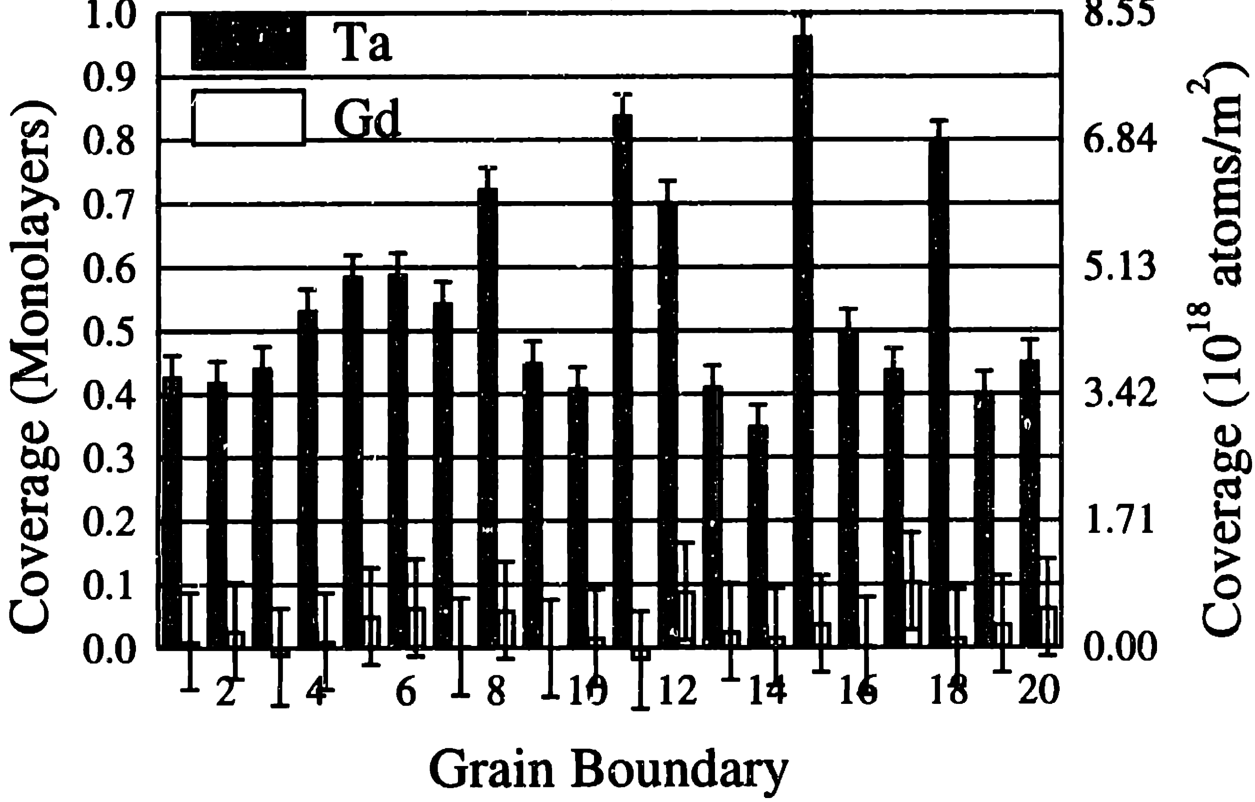

CGT4

Average 0.59 ± 0.09 Ta

0.06 ± 0.02 Gd

Gd	Ta	Ce L_{α_1} counts	VOA
0.81%	1.82%	60,000	50 μm

Bibliography

[1] N. Q. Minh. Ceramic Fuel Cells. *J. Am. Ceram. Soc.*, 76(3):563–588, 1993.

[2] B. C. H. Steele. State-of-the-Art SOFC Ceramic Materials. In U. Bossel, editor, *First European Solid Oxide Fuel Cell Forum Proceedings Volume 1*, pages 375–397, 1994.

[3] B. C. H. Steele. Applications of Ceramic Electrolytes in Electrochemical Engineering Systems. *Chem. Ind.*, 19:651–656, 1986.

[4] P.-L. Chen and I.-W. Chen. Grain Growth in CeO_2: Dopant Effects, Defect Mechanism and Solute Drag. *J. Am. Ceram. Soc.*, 79(7):1793–1800, 1996.

[5] S.-L. Hwang and I.-W. Chen. Grain Size Control of Tetragonal Zirconia Polycrystals Using the Space Charge Concept. *J. Am. Ceram. Soc.*, 73(11):3269–3277, 1990.

[6] D. D. Upadhyaya, R. Bhat, S. Ramanathan, S. K. Roy, H. Schubert, and G. Petzow. Solute Effect on Grain Growth in Ceria Ceramics. *J. Eur. Ceram. Soc.*, 14(4):337–341, 1994.

[7] J. Bauerle. Study of Solid Electrolyte Polarization by a Complex Admittance Method. *J. Phys. Chem. Solids*, 30:2657–2670, 1969.

[8] N. M. Beekmans and L. Heyne. Correlation Between Impedance, Microstructure and Composition of Calcia-Stabilized Zirconia. *Electrochim. Acta*, 21:303–310, 1976.

[9] M. Aoki, Y.-M Chiang, I. Kosacki, J.-R Lee, H. L. Tuller, and Y. Liu. Solute Segregation and Grain-Boundary Impedance in High-Purity Stabilized Zirconia. *J. Am. Ceram. Soc.*, 79(5):1169–1180, 1996.

[10] M. A. Panhans and R. N. Blumenthal. A Thermodynamic and Electrical Conductivity Study of Nonstoichiometric Cerium Dioxide. *Solid State Ionics*, 60:279–298, 1993.

[11] D. Y. Wang and A. S. Nowick. The "Grain Boundary Effect" in Doped Ceria Solid Electrolytes. *J. Solid State Chem.*, 35:325–333, 1980.

[12] D. Y. Wang and A. S. Nowick. A Grain-Boundary-Type Maxwell-Wagner Peak in the Thermally-Stimulated Depolarization of Doped Ceria Ceramics. *Physica Status Solidi (a)*, 73:165–172, 1982.

[13] D. Y. Wang, D. S. Park, J. Griffith, and A.S. Nowick. Oxygen-Ion Conductivity and Defect Interactions in Yttria-Doped Ceria. *Solid State Ionics*, 2:95–105, 1981.

[14] G. M. Christie and F. P. F. van Berkel. Microstructure-ionic conductivity relationships in ceria-gadolinia electrolytes. *Solid State Ionics*, 83:17–27, 1996.

[15] R. Gerhardt and A. S. Nowick. Grain-Boundary Effect in Ceria Doped with Trivalent Cations: I, Electrical Measurements. *J. Am. Ceram. Soc.*, 69(9):641–646, 1986.

[16] R. Gerhardt, A. S. Nowick, M. E. Mochel, and I. Dumbler. Grain-Boundary Effect in Ceria Doped with Trivalent Cations: II, Microstructure and Microanalysis. *J. Am. Ceram. Soc.*, 69(9):647–651, 1986.

[17] M. Gödickemeier, B. Michel, A. Orliukas, P. Bohac, K. Sasaki, L. Gauckler, H. Heinrich, P. Schwander, G. Kostorz, H. Hofmann, and O. Frei. Effect of Intergranular Glass Films on the Electrical Conductivity of 3Y-TZP. *Journal of Materials Reseach*, 9(5):1228–1240, 1994.

[18] L. Navarro, F. Marques, and J. Frade. n-Type Conductivity in Gadolinia-Doped Ceria. *J. Electrochem. Soc.*, 144(1):267–273, 1997.

[19] P. J. Scanlon, R. A. M. Bink, F. P. F. van Berkel, G. M. Christie, L. J. van IJzendoorn, H. H. Brongersma, and R. G. van Welzenis. Surface Composition of Ceramics CeGd-Oxide. *Solid State Ionics*, submitted.

[20] A. J. A. Winnubst, P. J. M. Kroot, and A. J. Burggraaf. AES/STEM Grain Boundary Analysis of Stabilized Zirconia Ceramics. *J. Phys. Chem. Solids*, 44(11):955–960, 1983.

[21] M. M. R. Boutz, A. J. A. Winnubst, and A. J. Burggraaf. Yttria-Ceria Stabilized Tetragonal Zirconia Polycrystals: Sintering, Grain Growth and Grain Boundary Segregation. *J. Eur. Ceram. Soc.*, 13:89–102, 1994.

[22] G. S. A. M. Theunissen, A. J. A Winnubst, and A. J. Burggraaf. Surface and Grain Boundary Analysis of Doped Zirconia Ceramics Studied by AES and XPS. *J. Mater. Sci.*, 27:5057–5066, 1992.

[23] A. E. Hughes. Segregation in Single-Crystal Fully Stabilized Yttria-Zirconia. *J. Am. Ceram. Soc.*, 78(2):369–378, 1995.

[24] P. J. Whalen, F. Reidinger, S. T. Correale, and J. Marti. Yttria migration in Y–TZP during high-temperature annealing. *J. Mater. Sci.*, 22:4465–4469, 1987.

[25] A. E. Hughes and S. P. S. Badwal. Impurity and Yttrium Segregation in Yttria-tetragonal Zirconia. *Solid State Ionics*, 46:265–274, 1991.

[26] A. E. Hughes and B. A. Sexton. XPS study of an intergranular phase in yttria-zirconia. *J. Mater. Sci.*, 24:1057-1061, 1989.

[27] T. Kudo and H. Obayashi. Oxygen Ion Conduction of the Fluorite-Type $Ce_{1-x}Ln_xO_{2-\frac{x}{2}}$ (Ln=Lanthanoid Element). *J. Electrochem. Soc.*, 122:142–147, 1975.

[28] T. H. Etsell and S. N. Flengas. Electrical Properties of Solid Oxide Electrolytes. *Chem. Rev.*, 70(3):339, 1970.

[29] G. B. Balazs and R. S. Glass. ac Impedance Studies of Rare Earth Oxide Doped Ceria. *Solid State Ionics*, 76:155–162, 1995.

[30] H. L. Tuller and A. S. Nowick. Defect Structure and Electrical Properties of Non-stoichiometric CeO_2 Single Crystals. *J. Electrochem. Soc.*, 126(2):209–217, 1979.

[31] T. G. Stratton and H. L. Tuller. Thermodynamic and Transport Studies of Mixed Oxides: The CeO_2–UO_2 System. *J. Chem. Soc., Faraday Trans.*, 83(2):1143-1156, 1987.

[32] J. H. Park, R. N. Blumenthal, and M. A. Panhans. Direct Measurement of Thermodynamic Properties in Nonstoichiometric CaO-Doped Cerium Dioxide by Coulometric Titration. *J. Electrochem. Soc.*, 135(4):855–859, 1988.

[33] H.-W Chiang, R. N. Blumenthal, and R. A. Fournelle. A High Temperature Lattice Parameter and Dilatometer Study of the Defect Structure of Nonstoichiometric Cerium Dioxide. *Solid State Ionics*, 66:85–95, 1993.

[34] R. J. Panlener, R. N. Blumenthal, and J. E. Garnier. A Thermodynamic Study of Nonstoichiometric Cerium Dioxide. *J. Phys. Chem. Solids*, 36:1213–1222, 1975.

[35] H. L. Tuller and A. S. Nowick. Doped Ceria as a Solid Oxide Electrolyte. *J. Electrochem. Soc.*, 122(2):255–259, 1975.

[36] A. Tschöpe, J. Y. Ying, K. Amonlirdviman, and M. L. Trudeau. Surface Chemistry of Nanocrystalline Cerium Oxide. In K. E. Gonsalves, G.-M. Chow, T. D. Xiao, and Robert C. Cammarata, editors, *Molecularly Designed Ultrafine/Nanostructured Materials*, volume 351 of *Materials Research Society Symposium Proceedings*, pages 251–256, Pittsburgh, PA, 1994.

[37] A. Trovarelli. Catalytic Properties of Ceria and CeO_2-Containing Materials. *Catal. Rev.*, 38(4):439–520, 1996.

[38] H. Inaba and H. Tagawa. Ceria-based Solid Electrolytes. *Solid State Ionics*, 83:1–16, 1996.

[39] M. Gödickemeier, K. Sasaki, and L. J. Glauckler. Operation Principles for Fuel Cells with Mixed Ionic Electronic Conductors. In B. Thorenstein, editor, *Proceedings of the Second European Solid Oxide Fuel Cell Forum*, 1997.

[40] M. Gödickemeier, K. Sasaki, and L. J. Gauckler. Current-Voltage Characteristics of Fuel Cells with Ceria-based Electrolytes. In M. Dokiya, O. Yamamoto, H. Tagawa, and S. C. Singhal, editors, *Proceedings of the Fourth International Symposium on Solid Oxide Fuel Cells*, 1996.

[41] M. Gödickemeier, K. Sasaki, L. J. Gauckler, and I. Riess. Electrochemical Characteristics of Cathodes in Solid Oxide Fuel Cells Based on Ceria Electrolytes. *J. Electrochem. Soc.*, 144(5):1635–1646, 1997.

[42] R. Gerhardt-Anderson and A. S. Nowick. Ionic Conductivity of CeO_2 with Trivalent Dopants of Different Ionic Radii. *Solid State Ionics*, 5:547–550, 1981.

[43] V. Butler, C. R. A. Catlow, B. E. F. Fender, and J. H. Harding. Dopant Ion Radius and Ionic Conductivity in Cerium Dioxide. *Solid State Ionics*, 8:109–113, 1983.

[44] I. K. Naik and T. Y. Tien. Small-Polaron Mobility in Nonstoichiometric Cerium Dioxide. *J. Phys. Chem. Solids*, 39:311–315, 1978.

[45] H. L. Tuller and A. S. Nowick. Small Polaron Electron Transport in Reduced CeO_2 Single Crystals. *J. Phys. Chem. Solids*, 38:859–867, 1977.

[46] P. V. Ananthapadmanabhan, S. B. Menon, D. S. Patil, N. Venkatramani, and V. K. Rohatgi. Electrical Conductivity of Cerium Dioxides Doped with Tantalum Pentoxide. *J. Mater. Sci.*, 11:501–503, 1992.

[47] M. R. De Guire, M. J. Shingler, and E. Dincer. Point Defect Analysis and Microstructural Effects in Pure and Donor-doped Ceria. *Solid State Ionics*, 52:155–163, 1992.

[48] J. A. S. Ikeda, Y.-M. Chiang, A. J. Garratt-Reed, and J. B. Vander Sande. Space Charge Segregation at Grain Boundaries in Titanium Dioxide: II, Model Experiments. *J. Am. Ceram. Soc.*, 76(10):2447–2459, 1993.

[49] J. A. S. Ikeda and Y.-M. Chiang. Space Charge Segregation at Grain Boundaries in Titanium Dioxide: I, Relationship between Lattice Defect Chemistry and Space Charge Potential. *J. Am. Ceram. Soc.*, 76(10):2437–2446, 1993.

[50] Y.-M. Chiang and J. A. S. Ikeda. Grain Boundary Segregation in Semiconducting Oxides. In *Grain Boundaries and Interfacial Phenomena in Electronic Ceramics*, volume 41 of *Ceramic Transactions*, pages 3–18, 1994.

[51] J. Frenkel. *Kinetic Theory of Liquids.* Oxford University Press, New York, 1946.

[52] F. A. Kröger and H. J. Vink. Relations between the Concentrations of Imperfections in Crystalline Solids. In F. Seitz and D. Turnbull, editors, *Solid State Phys.*, volume 3, pages 307–435. Academic Press, Inc., New York, 1956.

[53] K. L. Kliewer and J. S. Koehler. Space Charge in Ionic Crystals. I. General Approach with Applications to NaCl. *Phys. Rev. A*, 140(4A):A1226–A1240, 1965.

[54] Y.-M Chiang, E. B. Lavik, and D. A. Blom. Defect Thermodynamics and Electrical Properties of Nanocrystalline Oxides: Pure and Doped CeO_2. *NanoStructured Materials*, 9:633–642, 1997.

[55] C. Binet, A. Badri, and J.-C. Lavalley. A Spectroscopic Characterization of the Reductions of Ceria from Electronic Transitions of Intrinsic Point Defects. *J. Phys. Chem.*, 98(25):6392–6398, 1994.

[56] T. X. T. Sayle, S. C. Parker, and C. R. A. Catlow. The role of oxygen vacancies on ceria surfaces in the oxidation of carbon monoxide. *Surf. Sci.*, 316:329–336, 1994.

[57] D. C. Sayle, T. X. T. Sayle, S. C. Parker, J. H. Harding, and C. R. A. Catlow. The stability of defects in the ceramic interfaces, MgO/MgO and CeO_2/Al_2O_3. *Surf. Sci.*, 334:170–178, 1995.

[58] K. L. Kliewer. Space Charge in Ionic Crystals. II. The Electron Affinity and Impurity Accumulation. *Phys. Rev. A*, 140(4A):A1241–A1246, 1965.

[59] K. L. Kliewer. Space Charge in Ionic Crystals — III. Silver Halides Containing Divalent Cations. *J. Phys. Chem. Solids*, 27:705–717, 1966.

[60] K. L. Kliewer. Space Charge in Ionic Crystals — IV. Interstitial-Producing Impurities in the Silver Halides. *J. Phys. Chem. Solids*, 27:719–725, 1966.

[61] J. A. S. Ikeda. *Grain Boundary Defect Chemistry and Electrostatic Potential in Acceptor- and Donor-doped Titanium Dioxide.* PhD thesis, Massachusetts Institute of Technology, Cambridge, MA, May 1992.

[62] R. B. Poeppel and J. M. Blakely. Origin of Equilibrium Space Charge Potentials in Ionic Crystals. *Surf. Sci.*, 15:507–523, 1969.

[63] J. M. Blakely and S. Danyluk. Space Charge Regions at Silver Halide Surfaces: Effects of Divalent Impurities and Halogen Pressure. *Surf. Sci.*, 40:37–60, 1973.

[64] S. Danyluk and J. M. Blakely. Space Charge Regions at Silver Halide Surfaces: Experimental Results for Undoped AgCl. *Surf. Sci.*, 41:359–370, 1974.

[65] D. Schneider, M. Gödickemeier, and L. J. Gauckler. Nonstoichiometry and Defect Chemistry of Ceria Solid Solutions. *Journal of Electroceramics*, 1(2):165–172, 1997.

[66] B. C. H. Steele and J. M. Floyd. Oxygen Self-Diffusion and Electrical Transport Properties of Non-stoichiometric Ceria and Ceria Solid Solutions. In *Proc. Br. Ceram. Soc.*, volume 19, pages 55–76, 1971.

[67] A. S. Nowick, D. Y. Wang, D. S. Park, and J. Griffith. Oxygen-Ion Conductivity and Defect Structure of CeO_2 Doped with CaO and Y_2O_3. In P. Vashishta, J. N. Mundy, and G. K. Shenoy, editors, *Fast Ion Trans. Solids: Electrodes Electrolytes, Proc. Int Conf.*, pages 673–677. Elsevier North Holland Inc., 1979.

[68] T. G. Stratton. *Electrical Properties and Defect Structure of UO_2-CeO_2 Solid Solutions.* PhD thesis, Massachusetts Institute of Technology, Cambridge, MA, February 1984.

[69] S. Ling. High-concentration point-defect chemistry: Statistical-thermodynamic approach applied to nonstoichiometric cerium dioxides. *Phys. Rev. B*, 49(2):864–880, 1994.

[70] M. H. R. Lankhorst, H. J. M. Bouwmeester, and H. Verweij. Thermodynamics and Transport of Ionic and Electronic Defects in Crystalline Oxides. *J. Am. Ceram. Soc.*, 80(9):2175–2198, 1997.

[71] A. K. A. Pryde, S. Vyas, R. W. Grimes, J. A. Gardner, and R. Wang. Cadmium and Indium Defects in Ceria and their Interactions with Oxygen Vacancies and Small Polarons. *Phys. Rev. B*, 52:13214–13222, 1995.

[72] M. P. Sheah. Grain boundary segregation. *J. Phys. F*, 10:1043–1064, 1980.

[73] P. Lejcek and S. Hofmann. Thermodynamics and Structural Aspects of Grain Boundary Segregation. *CRC Crit. Rev. Solid State Mater. Sci.*, 20(1):1–85, 1995.

[74] D. McLean. *Grain Boundaries in Metals.* Clarendon Press, 1957.

[75] R. C. McCune and P. Wynblatt. Calcium Segregation to a Magnesium Oxide (100) Surface. *J. Am. Ceram. Soc.*, 66(2):111–117, 1983.

[76] R. D. Shannon. Revised Effective Ionic Radii and Systematic Studies of Interatomic Distances in Halides and Chalcogenides. *Acta Crystallogr. Sect A: Cryst. Phys., Diffr., Theor. Gen. Crystallogr.*, A32:751–767, 1976.

[77] A. Atkinson. Chemically-induced stresses in Gadolinium-doped Ceria Solid Oxide Fuel Cell Electrolytes. *Solid State Ionics*, 95:249–258, 1997.

[78] S. E. Hill and C. R. A. Catlow. A Hartree-Fock Periodic Study of Bulk Ceria. *J. Phys. Chem. Solids*, 54:411–419, 1993.

[79] J. Andrés and A. Beltrán. An ab initio Perturbed Ion Study of Bulk Ceria. *Chem. Phys. Lett.*, 221:249–254, 1994.

[80] T. H. Courtney. *Mechanical Behavior of Materials.* McGraw-Hill, Inc., New York, 1990.

[81] M. Guttmann and D. McLean. Grain Boundary Segregation in Multicomponent Systems. In W. C. Johnson and J. M. Blakely, editors, *Interfacial Segregation*, pages 261–348, Metals Park, OH, 1979. American Society for Metals.

[82] J. A. S. Ikeda, Y.-M Chiang, and A. J. Garratt-Reed. Quantification of Grain Boundary Segregation in TiO_2 by STEM. In *Proceedings of the XIIIth International Congress on X-ray Optics and Microanalysis.* IOP Publications, 1992.

[83] K. F. J. Heinrich. X-ray Absorption Uncertainty. In T. D. McKinley, K. F. J. Heinrich, and D. B. Wittry, editors, *Electron Microprobe, Proc. Symp.*, pages 296–377, New York, 1966. J. Wiley & Sons.

[84] G. Cliff and G. W. Lorimer. The Quantitative Analysis of Thin Specimens. *Journal of Microscopy*, 103:203, 1975.

[85] W. Furdanowicz. *Effects of Diffraction on Microanalysis of Embedded Precipitates.* PhD thesis, Massachusetts Institute of Technology, Cambridge, MA, February 1991.

[86] E. B. Lavik. The Electrical Properties of Pure and Doped Nanocrystalline Cerium Oxide. Master's thesis, Massachusetts Institute of Technology, 1997.

[87] Y.-M. Chiang, J.-R. Lee, and H. Wang. Microstructure and Intergranular Phase Distribution in Bi_2O_3-doped ZnO. In A. P. Tomsia and A. Glaeser, editors, *Ceramic Microstructures '96: Control at the Atomic Level*, NY, 1998. Plenum.

[88] D. A Reeve and N. F. H. Bright. *J. Am. Ceram. Soc.*, 52(8):407, 1969.

[89] N. A. Toropov. *Trans. Intern. Ceram. Congr. 7th.* 1960.

[90] H. Wang and Y.-M. Chiang. Thermodynamic Stability of Intergrnaular Amorphous Films in Bismuth-Doped Zinc Oxide. *J. Am. Ceram. Soc.*, 81(1):89–96, 1998.

[91] Y.-M. Chiang, H. Wang, and J.-R. Lee. HREM and STEM of Intergranular Films at Zinc Oxide Varistor Grain Boundaries. *J. Microscopy*, submitted.

[92] H. D. Ackler and Y.-M. Chiang. Model Experiment on Thermodynamic Stability of Retained Intergranular Amorphous Films. *J. Am. Ceram. Soc.*, 80(7):1893–1896, 1997.

[93] J. Maier. Ionic Conduction in Space Charge Regions. *Progress in solid state chemistry*, 23(3):171–263, 1995.

[94] R. Hagenbeck and R. Waser. Simulation of Electrical Properties of Grain Boundaries in Titanate Ceramics. *Ber. Besunges. Phys. Chem.* , 101(9):1238–1241, 1997.

[95] R. Hagenbeck and R. Waser. Influence of temperature and interface charge on the grain-boundary conductivity in acceptor-doped $SrTiO_3$ ceramics. *J. Appl. Phys.* , 83(4):2083–2092, 1998.